Construction of a new ultra-cold Ytterbium experiment for nonlinear quantum optics based on Rydberg atoms

Jiachen Zhao

I hereby declare that this thesis was formulated by myself and that no sources or tools other than those cited were used.

Bonn, ...

03.02.2022   Jiachen Zhao

Date   Signature

1. Gutachter: Prof. Sebastian Hofferberth
2. Gutachter: Prof. Simon Stellmer

Acknowledgements

I would like to thank all the people who were part of this experience and helped me learn so much over the course of the past year.

My sincere and hearty thanks and appreciations go firstly to my supervisor, Prof. Dr. Sebastian Hofferberth, for his kindness, illuminating guidance and profound knowledge. It has been a great privilege and joy to study under his guidance and supervision. Furthermore, it is my honor to be his first master student in Bonn.

Secondly, I would like to express my heartfelt thanks to Prof. Dr. Dieter Meschede, whose suggestions and encouragement have given me much insight into quantum optics.

I also want to thank Dr. Rafael Rothganger de Paiva and Dr. Mohammad Noaman, who were always there whenever I needed them.

In addition, I would like to thank all group members, especially Thilina Muthu-Arachchige, Nina Stiesdal, Hannes Busche, Lukas Ahlheit, Cedric Wind, for their kind help.

Finally, I want to thank my parents, who made all of this possible.

Contents

Introduction

The study of Rydberg atoms has a long history in physics, extending back more than a century when the high-lying energy levels of hydrogen in the Balmer series were originally investigated in atomic spectroscopy to provide as the experimental foundation for Bohr's atom modeling [1]. In today's atomic physics, Rydberg-atoms play a unique role due to their strong long-range interactions based on their high polarizability [2]. Various experiments involved with Rydberg atoms yielded new important results. For example, in 2009, the first experimental implementation of a quantum gate based on Rydberg-atoms was demonstrated [3]. Furthermore, the long-lifetime and large electric dipole moment of Rydberg atoms in a high-Q resonant cavity led to the counting of emitted microwave photons, allowing quantum non-demolition photon state measurements, which was recognized by the Nobel physics prize in 2012 [4, 5]. All these results emphasize that Rydberg-atoms can serve as fundamental component for applications in quantum computation, offering the possibility to build required single photon-sources [6] single-photon absorbers [2] and a quantum repeater [7] for quantum-communication over long distances.

In conventional optical materials, photon interactions are negligible and nonlinear effects, such as frequency doubling or sum-frequency generation, do only occur at extremely high intensities [8]. The simplest system to consider is a single atom coupled to a faint light field. To produce significant effective interactions between individual photons in the probe field, the atomic absorption must be saturated with a single photon. The minuscule atom-photon scattering cross section necessitates matching the geometry of the light field to the single atom's dipolar emission pattern. Even with the enormous advances in precision optics engineering, only modest coupling efficiencies have been achieved so far. Alternatively, optical nonlinearities have been explored in ensembles of atoms using slow light provided by electromagnetically induced transparency (EIT).

The essential concept is to combine EIT with the strong interaction of Rydberg atoms. Both of these phenomena have been extensively researched in the past: EIT has been used to demonstrate that photons can be slowed down and stored in cold atomic ensembles. [9], while recent studies on Rydberg atoms have demonstrated the strong interaction and related blockade of Rydberg excitations [10](when two quantum systems interact strongly with each other, their simultaneous excitation by the same driving pulse may be forbidden). In the Rydberg-EIT system, the first photon entering the atomic gas is transformed into a slow-light polariton with a significant admixture of the Rydberg state. The latter admixture effectively maps the Rydberg-Rydberg interaction onto an effective interaction between slow Rydberg polaritons. Within this approach, the formation of bound states of Rydberg polaritons [11] have been demonstrated, and even up to three-photon correlations were observed [12].

In recent years, there has been an increase in the use of alkaline-earth-like atoms (AEL) in ultracold atom experiments. AEL atoms have a more complex internal structure and possess several highly intriguing features, e.g., metastable excited electronic states or a nuclear spin that is decoupled from the electron shell. The presence of two valence electrons of AEL atoms allows the production of both

singlet and triplet states which exhibit a diversity of attractive and repulsive interactions. Furthermore, the excitation of one electron to a Rydberg state results in an optically active core ion that allows for multiple manipulations of the second valence electron [13]. Therefore, AEL atoms can provide a new significant platform for researching nonlinear quantum effects in Rydberg physics. Ytterbium is a particularly versatile one among the AEL elements, e.g., it has the largest number of stable isotopes among these elements. Five bosonic and two fermionic isotopes not only enable the study of multiple isotope mixtures but also provide a variety of different interaction strengths, nuclear spins, and other isotope-dependent properties for specific experiments [14].

About this thesis

This thesis describes a newly constructed experiment for ultracold ytterbium Rydberg atom studies. The experiment seeks to research nonlinear quantum optics by utilizing the unique properties of ytterbium combined with ultra cold atom techniques to produce a cold and highly dense nonlinear medium in which many-body phenomena involving highly interacting Rydberg-polariton can be studied. Additionally, it aims to investigate the emerging field of alkaline-earth-like Rydberg physics.

The proposed ytterbium experiment employs a dual-chamber design. This comprises a two-dimensional magneto optical trap (2D-MOT) as a source of cold atoms, with the 2D-MOT loaded directly from an atom stream emitted by dispensers. The ultra-high vacuum science chamber in which the atoms are trapped in a 3D-MOT is used for studying the nonlinear quantum effects in a single photon level.

Rydberg EIT system demands high frequency stability of the laser system. More specifically, the radiative lifetime of the Rydberg atoms scales with the principal quantum number n^3 which needs control of the excitation laser linewidth generally down to kHz to address the proper Rydberg state. An ultrastable, high-finesse cavity is utilized as a frequency reference supplying the necessary stability and precision of the lasers.

This thesis is structured as follows. The first chapter presents alkaline-earthlike atoms, focusing on ytterbium and its pertinent features, as well as the opportunities for Rydberg quantum optics experiments that ytterbium may offer. In Chapter 2, the setup of laser system and vacuum system are described. Chapter 3 discusses the theoretical background of the laser locking techniques and presents the characterization of the laser setup. Chapter 4 presents the pulse shaping of the probe and control fields. Chapter 5 discusses the design and construction of new in-house built ultra-high-vacuum (UHV) compatible 2D-MOT chamber. In Chapter 6, the experiment results of 2D/3D Magneto-optical trap (MOT) are briefly shown. Chapter 7 summarizes the current status of the experiment and outlines the next stages of realizing ultra-cold Ytterbium Rydberg atoms.

Alkaline-earth-like (AEL) Rydberg Atoms: Ytterbium

AEL elements have mostly been used as strong frequency standards in the recent past: their atomic structure contains low-lying metastable electronic states, and the corresponding ultra-narrow optical transitions exhibit an extraordinary intrinsic precision [15]. Since the first alkaline-earth-based optical lattice atomic clock was constructed, several lattice clock systems have been established around the globe and now represent the most exact frequency standards, surpassing even the performance of single-ion atomic clocks [16]. Along with their application in quantum metrology, AEL atoms were introduced to the cold atom community more than a decade ago, when the first bosonic isotope of ytterbium was cooled to degeneracy by the Takahashi group in Kyoto [17]. Their enormous quantum simulation potential was then realized shortly after they were described as a viable system for quantum computing in optical lattices [18]. Among them, due to the intensity of their interactions and their nuclear spin characteristics, the fermionic ^{87}Sr and ^{173}Yb are particularly intriguing candidates for quantum simulations of strongly correlated phases [19].

In this chapter, we review the general properties of AEL atoms. Besides, it is intended to provide an overview of the properties of ytterbium, followed by a discussion of the advantages for nonlinear quantum optics experiments using ytterbium.

1.1 Characteristics of Alkaline-earth-like (AEL) Atoms

The majority of AEL atoms' features are due to their unique two-valence electron level configuration. The two outer electrons may form a spin singlet (S = 0), as in the ground state $\left(^{1}S_{0}\right)$, or a spin triplet (S = 1). Thus, all lower-lying electronic levels may be classified into two manifolds, each of which has either S = 0 or S = 1 total electronic spin. All transitions from electronic states in the singlet manifold to states in the triplet manifold are typically very narrow due to the fact that spin-flipping transitions (ΔS $\neq$ 0) are banned in the dipole approximation [20]. A limited dipole coupling exists between the ground state and the triplet states only as a result of a slight mixing of triplet and singlet electronic states caused by spin-orbit and hyperfine interactions. One such narrow transition is the $^{1}S_{0} \rightarrow {}^{3}P_{1}$, which may be used to Doppler cool atomic samples to very low temperatures of the order of 10 μK or below, enabling efficient direct loading of an optical dipole trap. Additionally, more complex all-optical systems leveraging this narrow transition have been developed, resulting in the

Mass number	Natural abundance	Nuclear Spin	Type
168	0.13%	0	Boson
170	3.05%	0	Boson
171	14.3%	1/2	Fermion
172	21.9%	0	Boson
173	16.12%	5/2	Fermion
174	31.8%	0	Boson
176	12.7%	0	Boson

Table 1.1: Stable isotopes of Ytterbium, taken from Ref.[26]

enhanced fast synthesis of degenerate AEL atomic gases [21]. Another peculiarity of AEL atoms is the wavelength range of the optical transitions used for laser cooling and state manipulation: they all fall within the visible region of the electromagnetic spectrum, in contrast to the transitions used in alkali atom experiments, which typically fall within the near-infrared range.

The existence of metastable, long-lived excited electronic states in the triplet manifold, notably the $^3P_0$ and the $^3P_2$ states, which are very weakly coupled to the ground state, is a notable feature of AEL atoms. Transitions from such states to the ground state have extremely low linewidths of 10mHz at most, corresponding to state durations of tens to hundreds of seconds for the lightest AEL elements. These transitions are commonly referred to be ultranarrow since they are more than a factor of 10^8 narrower than ordinary optical transitions with linewidths ranging from 1 to 10 MHz. The $^1S_0 \rightarrow {}^3P_0$ transition is commonly referred to as the clock transition since it is commonly employed in single-ion and optical lattice atomic clocks [22]. The clock transition in fermionic AEL has a phenomenally high Q-factor exceeding 10^{17}, which has enabled the creation of the world's most stable and precise atomic clocks [16]. Because it can be utilized as a precise spectroscopic probe in the study of ultracold gases, such a narrow transition is a very powerful experimental resource. Spectroscopy of many-body states based on narrow transitions has already been used to bosonic Mott insulators [23], and confined gases [24].

1.2 General Properties of Ytterbium

Ytterbium is a rare-earth element belonging to the lanthanide class. It has a proton number of $Z = 70$. Its complete electronic structure is $[Xe]4f^{14}6s^2$, which is determined mostly by the two valence electrons in the 6s-shell. Ytterbium exists naturally in seven stable isotopes, five of which are fermions and two of which are bosons. As a result, ytterbium enables the realization of ultracold Bose–Bose, and very intriguing Bose–Fermi systems isotope mixtures of Fermi and Fermi [25]. Table 1.1 summarizes the natural abundance and nuclear spin of each isotope.

Typically, the atomic source requires temperatures between $400°C$ and $500°C$ to provide a sufficient flux. Another significant attribute of ytterbium is its low vapour pressure at room temperature, $p_{Yb,RT} \sim 10^{-21}$ mbar, which is orders of magnitude lower than the vapour pressure of rubidium, $p_{Rb,RT} \sim 10^{-7}$ mbar, a typical element used in cold atom investigations. Due to that, ytterbium collides with a surface in a high vacuum chamber does not evaporate but rather adheres to it.

1.3 Electronic Structure of Ytterbium

The atomic characteristics of ytterbium are mostly determined by the two s-shell valence electrons, which are split into two manifolds with total electronic spin (S = 0) and (S = 1), respectively. The weak intercombination transitions between these spin configurations give rise to crucial ytterbium properties, including narrow-line laser cooling and metastable excited electronic states. As is the case with other alkaline-earth-metal-like substances, the excited states are either singlet (S = 0) or triplet (S = 1) states. Fig. 1.1 shows the energy levels up to $40000 \, \text{cm}^{-1}$. All energy levels were denoted by the symbol $^{2S+1}L_J$, where S denotes the total electronic spin, L denotes the total orbital angular momentum of all electrons in the system (denoted by the letters S, P, D for L = 0, ..., 2), and J denotes the system's total angular momentum. The critical transitions are summarized here.
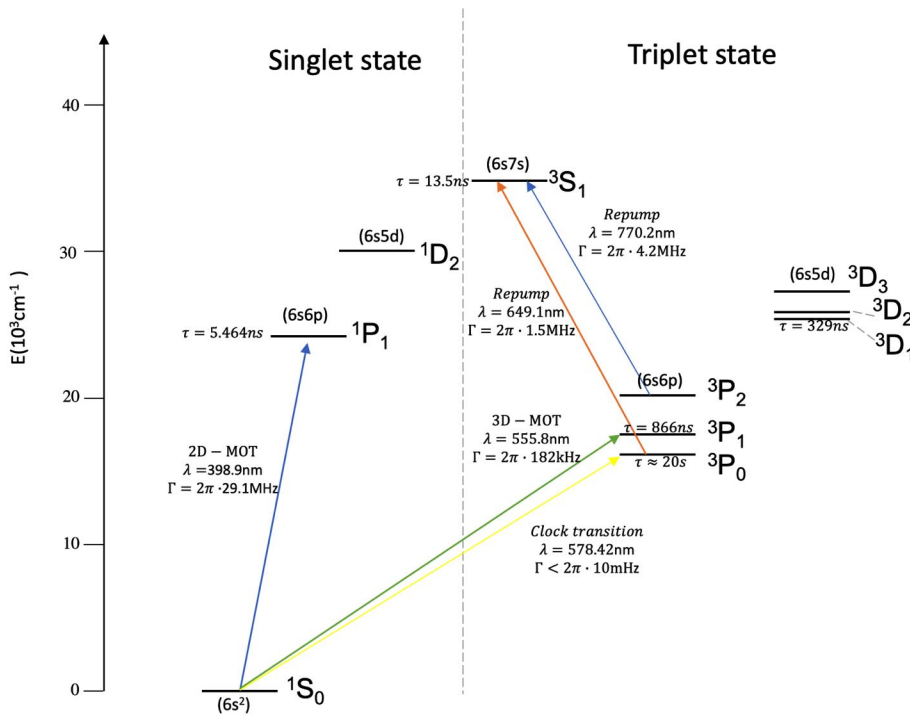

Figure 1.1: Level diagram of Ytterbium, the relevant energy levels and transitions for mainly cooling Yb atoms, precision spectroscopy and optical pumping are illustrated, taken from Refs.[27–30]

$^1S_0 \longleftrightarrow {}^1P_1 (399 \, \text{nm})$
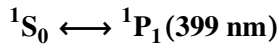
The wavelength of the E1 dipole-allowed transition is 398.9 nm, which is in the visible blue-violet region of the optical spectrum. Due to its broad linewidth, it is mostly used for initial atom slowing and magneto-optical trapping, as well as absorption imaging. Its natural linewidth was determined to $\Gamma_{\text{blue}}/2\pi = 29.13(3)$ MHz [28]. Although this strong transition is nearly closed, a very weak radiative decay channel exists between the $^1P_1$ and the $^3P_{0,1,2}$ states.

$^1S_0 \longleftrightarrow {}^3P_1 (556 \, \text{nm})$
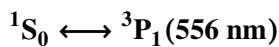
This singlet to triplet intercombination transition is strictly forbidden in the $L - S$ coupling

scheme. For heavy elements such as Ytterbium, $J - J$ coupling between the orbital and spin motions of the two valence electrons results in a relaxation of the selection rules. Spin–orbit coupling modifies atomic eigenstates and admixes small fractions of states from the opposite spin manifold, which acquires small transition amplitudes. On the other hand, due to the suppression of spin-changing transitions, ytterbium's intercombination transition $^1S_0 \leftrightarrow {}^3P_1$ has a line width of just $\Gamma/2\pi = 181$ kHz. As a result, its saturation intensity is significantly lower $I_{\text{sat}} = 0.14$ mWcm^{-2}, and the Doppler cooling limit drops to 4 μK. The Doppler cooling limit and saturation intensity of each transition can be calculated by [31]

$$k_B T_D = \frac{\hbar\Gamma}{2}$$

$$I_{L,\text{sat}} = \frac{\pi hc}{3\lambda^3}\Gamma$$

where λ and Γ are wavelength of the transition and decay rate of the excited state, respectively.

$^1S_0 \longleftrightarrow {}^3P_0$ (578 nm)

The $^3P_0$ state is very weakly coupled to the $^1S_0$ ground state in this double forbidden transition, with decay rates in the tens of millihertz range. The ultra-narrow transition is referred to as clock-transition. For fermionic isotopes, the hyperfine interaction couples states with the same F and causes a mixing between the $^3P_0$ state and the $^3P_1$ (F = I) state, which yields values for the natural linewidths of the clock transition $\Gamma_{\text{clock}}/2\pi = 7$ mHz in ^{173}Yb and $\Gamma_{\text{clock}}/2\pi = 6$ mHz in ^{171}Yb. Radiative decay of this state in bosonic ytterbium isotopes is only feasible via multi-photon processes, such as the EM two-photon transition. Thus, its lifetime is much longer than in the fermionic isotopes.

$^1S_0 \longleftrightarrow {}^3P_2$ (507 nm)

In contrast to $^3P_0$, the transition from the ground state to the second metastable state, $^1S_0 \leftrightarrow {}^3P_2$ ($\Delta J = 2$), is permitted, however only as a only as a magnetic quadrupole (M2) or higher transition. This quadruple magnetic (M2) transition is also an ultra-narrow transition with a linewidth of a few tens of millihertz. Furthermore, the excited state has a large magnetic dipole moment of $3\mu_B$, which could be used as a readout state in quantum information processing protocols by tuning dipole-dipole interactions between atoms in an optical lattice [32].

$^3P_0 \rightarrow {}^3S_1$ and $^3P_2 \rightarrow {}^3S_1$

The $^3P_1$ state of an atom decays rapidly to the ground state, whereas the $^3P_{0,2}$ state is metastable. As a result, atoms trapped in a MOT operating at the blue transition can be lost when shelved in those states. To restore the blue cooling cycle to atoms, optical repumping of the $^3P_{0,2}$ states to the $^3S_1$ state can be employed [33]. The strongly allowed $^3P_0 \rightarrow {}^3S_1$ and $^3P_2 \rightarrow {}^3S_1$ transitions have respective wavelengths of 649.1 nm and 770.2 nm with linewidths of roughly 12 MHz. Both transitions must be driven simultaneously to ensure efficient repumping to the ground state via an intermediate decay to the $^3P_1$ state, due to the $^3S_1$ state's branching ratio of about 1:3:4 in comparison to the $^3P_{0,1,2}$ states [34].

$^1S_0 \longleftrightarrow {}^3D_2$ (404 nm)

This E2 transition with a linewidth of $\Gamma/2\pi = 350$ kHz is effective for optical pumping atoms into the $^3P_2$ and $^3P_0$ states. Atoms excited to the $^3D_2$ state decay in a 20:3 ratio to the $^3P_{1,2}$

states. Due to the fact that the atoms in the $^3P_1$ state decay to the ground state after a few cycles, it is possible to pump all the atoms into the $^3P_2$ state.

1.4 Advantages of Ytterbium

The Ground State of Ytterbium

Ytterbium's ground state is the spin-singlet state $^1S_0$. Because the electron shell has no net angular momentum (L=S=J=0), its total angular momentum F is entirely determined by the nuclear spin I. As a result, the ground state exhibits a number of highly fascinating properties, such as nuclear spin decoupling. Its insensitivity to magnetic fields makes it particularly valuable for a variety of applications, including precision spectroscopy on ultranarrow transitions and matter-wave interferometry.

Long Coherence Times

An important concept in quantum mechanics is coherence time. Decoherence mechanisms in collective Rydberg excitation-based photon storage systems are mostly due to thermal atomic motion. The collective excitation of a Rydberg atomic ensemble can be written as [35]

$$|R\rangle = \frac{1}{\sqrt{N}} \sum_{j=1}^{N} e^{i(k_c - k_p)r_j} \left|g_1, \ldots, r_j, \ldots, g_N\right\rangle$$

with counter-propagating probe beam k_p and control beam k_c in one dimension, r_j denotes the position of atom j and the $\left|g_1, \ldots, r_j, \ldots, g_N\right\rangle$ donates the atom j in the Rydberg state $|r\rangle$ other atoms in the ground state. The phase factor reads

$$\left(k_c - k_p\right) r_j = 2\pi \left(\frac{1}{\lambda_c} - \frac{1}{\lambda_p}\right) vt =: \frac{t}{\tau_{coh}}$$

with the mean velocity of the atoms v. The mean velocity establishes the upper bound for the coherence time scale $\tau_{coh.}$. While thermal atomic motion can be mitigated by cooling the atoms, decoherence comes from a wavelength mismatch in the two-photon transition from the ground to the Rydberg state [36]. The two-photon transition of ytterbium from the ground to Rydberg state is shown in Fig. 1.2. Since the wavelength of the probe beam and control beam are close, it will lead to a small phase factor which corresponds to a long coherence time at a given temperature. For temperatures 10 μK near to the Doppler temperature of the triplet transition, the highest limit of the coherence time scale in ytterbium is $\tau_{coh,Yb} = 80 \ \mu s \gg 2 \ \mu s = \tau_{coh,Rb}$, which is significantly longer than rubidium and results in longer coherence times.

Rayleigh Length

The wavelength of the probe light is the major limitation for the length of a Rydberg EIT medium in free space. Typically, the atomic cloud is located at the focus of the probe beam, which diverges along the length scale of the Rayleigh length $z_R = \pi w_0^2 / \lambda$ with the waist w_0 and the wavelength λ. To have a decent probability of excitation Rydberg states, the diameter of the probe beam must be less than the blockade radius $2w_0 < r_b$, which is $w_0 < 10 \ \mu$m for all prior experiments with alkali atoms. In comparison to alkali atoms, which have probe beam
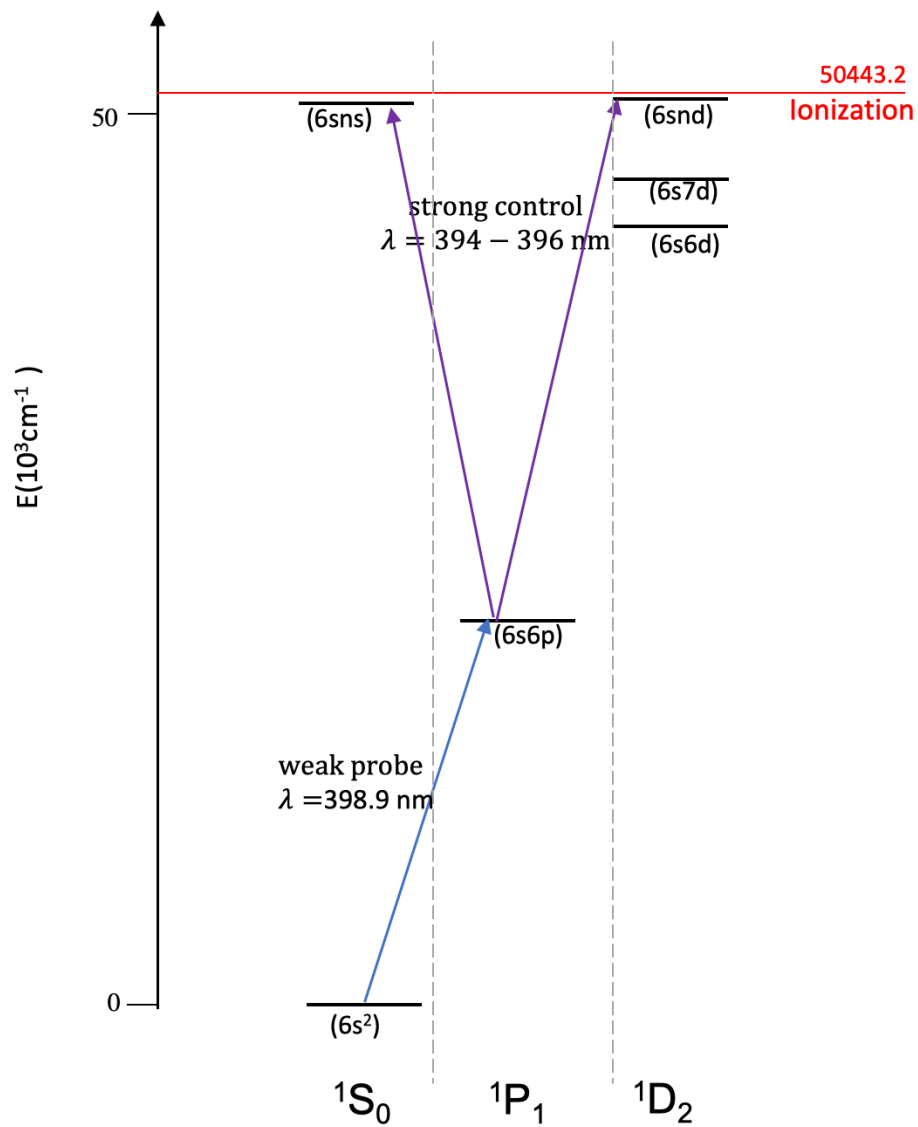
Figure 1.2: Two-photon transition of ytterbium from the ground to Rydberg state. The ground state is coupled with a weak, single photon probe laser to the intermediate state. The Rydberg state is excited by strong control laser.

wavelengths in the infrared, ytterbium has a near-ultraviolet wavelength, allowing for a huge EIT-medium capable of investigating the interactions of a large number of Rydberg-polaritons.

High Blocked Depth

The critical figure of merit which characterizes the strength of the non-linearity is the blockaded optical depth $OD_b = (2r_b/L) \, OD$, where $2r_b$ denotes the diameter of the blockaded sphere, L denotes the length of the optical medium, and OD is the optical depth. $OD_b \geq 1$ is necessary to enter the quantum nonlinear regime. Since the OD is proportional to the number of atoms and the Doppler cooling limit of ytterbium's intercombination transition $^1S_0 \leftrightarrow \, ^3P_1$, gives a relatively low starting point (4 μK) for the further cooling scheme without losing atoms, the potential of ytterbium allows it to have a larger high blocked depth than alkali atoms.

Non-radiative Decay

While the preceding section has concentrated on radiative decay, an atom's environment naturally results in the emergence of a number of additional decay mechanisms. For example, it has been found that quenching the $^3P_2$ state with black-body radiation (BBR) – via excitation of neighboring ^3D states significantly diminishes its lifetime in strontium at ambient temperature. However, the effect of BBR quenching on ytterbium is expected to be minor [37].

1.5 Lifetime of Rydberg Atoms

The lifetime of the Rydberg state, which defines the linewidth of the excitation, imposes one of the demands on the laser system. The frequency inaccuracy of the laser frequency must be less than the linewidth in order to resolve the linewidth of an atomic transition. The spontaneous decay (to the ground state) is the first mechanism limiting the lifetime of Rydberg atoms. The lifetime of the excited state in a two-level system can be described by the Einstein A-coefficient for spontaneous emission of a photon as

$$\frac{1}{\tau_{if}} = A_{if} = \frac{\omega_{if}^3}{3\pi\epsilon_0\hbar c_0^3}|\langle f|e\mathbf{r}|i\rangle|^2, \tag{1.1}$$

where ω_{if} is the transition frequency and $\langle i|e\mathbf{r}|f\rangle$ the transition dipole moment for the transition from state $|i\rangle$ to state $|f\rangle$. In the case of Rydberg atoms, taking only one final state into account is insufficient because the Rydberg state can generally decay to various states. As a result, the contributions of all relevant transitions must be added up.

$$\frac{1}{\tau_{n,1}^{n',1'}} = \sum_{n',1'} A_{n,1}^{n',1} \tag{1.2}$$

Typical values for transitions between nearby Rydberg levels are around 100 GHz and 1000 ea_0 for the dipole matrix element. For decay to the ground state, the level spacing is around 600 THz, and the dipole matrix element is 0.01 ea $_0$. This implies that the decay of Rydberg atoms to the ground state contributes the most to lifetime [38].

Apart from spontaneous decay to the ground state, Rydberg atoms have a limited lifetime due to blackbody radiations. This occurs when the main modes of the environment blackbody spectrum equal the splitting of the energy difference between adjacent Rydberg levels. Stimulated emission to other Rydberg levels occurs in this situation, lowering the lifetime.

The probability $W_{n,1}^{n',1'}$ for a blackbody induced transition from a state $n, 1$ to a state n',l', can be calculated by the Einstein coefficient and the number of photons per mode, given by the Planck-distribution

$$W_{n,1}^{n',1'} = A_{n,1}^{n',1'} \cdot \frac{1}{\exp\left(\omega_{n,l}^{n',l'}/kT\right) - 1}.$$

(1.3)

the decay rate Γ_{BBR} by summing over all contributing Rydberg states

$$\Gamma_{BBR} = \frac{1}{\tau_{BBR}} = \sum_{n',l'} A_{n,1}^{n',1'} \cdot \frac{1}{\exp\left(\omega_{n,l}^{n',l'}/kT\right) - 1}.$$

(1.4)

the total lifetime of Rydberg atoms reads [39]

$$\tau(n,1) = \left[\frac{1}{\tau_{rad}(n,1)} + \frac{1}{\tau_{BBR}(n,1)}\right]^{-1}$$

(1.5)

Experiment Setup

A novel experimental apparatus for studies of ytterbium quantum gases and ultrahigh-precision spectroscopy has been designed and constructed during a major part of this thesis.

2.1 Laser System for the Novel Ytterbium Experiment

As it is already discussed in section 1.2. The low Doppler temperature of the triplet transition $^1S_0 \to {}^3P_1$ is great to produce relatively cold and dense MOTs just by Doppler cooling. In turn, the problem with a pure "green" MOT is a very low capture velocity [40]. A solution for this problem employed in the ytterbium experiment is to combine the low temperature of the triplet MOT with the high capture velocity of a singlet MOT: A green MOT traps and cools atoms in a central region while a blue "shell" MOT provides an initial slowing of atoms coming from the 2D-MOT. This section will summarize the technical details of the various laser setups assembled for this thesis and utilized to conduct the experiments described in it. To begin, the two laser systems that generate light for laser cooling and resonant manipulation or detection of atoms, namely the blue and green laser systems will be described. Secondly, the infrared laser sources that provide high-power outputs for the optical dipole trap are briefly illustrated.

2.1.1 Blue MOT Laser

The blue laser in the setup is needed to produce the necessary light at 399 nm which corresponds to the singlet transmission $^1S_0 \to {}^1P_1$ of Yb. It is used for initial cooling in the 2D-MOT chamber and in a core-shell-MOT configuration as the shell beam to increase the capture velocity. Additionally, it is also employed as a push beam to boost the flux into the science chamber.

  The blue laser used in the setup is a commercial Toptica DLpro-TA-SHG laser. It consists of a 798 nm grating stabilized diode laser which is used as a seed for a tapered amplifier. The amplified light is then fed to a second-harmonic generation (SHG) cavity and frequency up-converted to 399 nm. With this scheme, the laser reaches output powers of up to 1300 mW of blue light. The integration of the blue laser into the complete laser system is visualized in Fig. 2.1. A pick-up of the 798 nm seed light for the blue laser is separated into two branches by a polarizing beamsplitter (PBS) on the top side. One of the branches is coupled to a wavemeter[1], which allows the determination of the frequency with
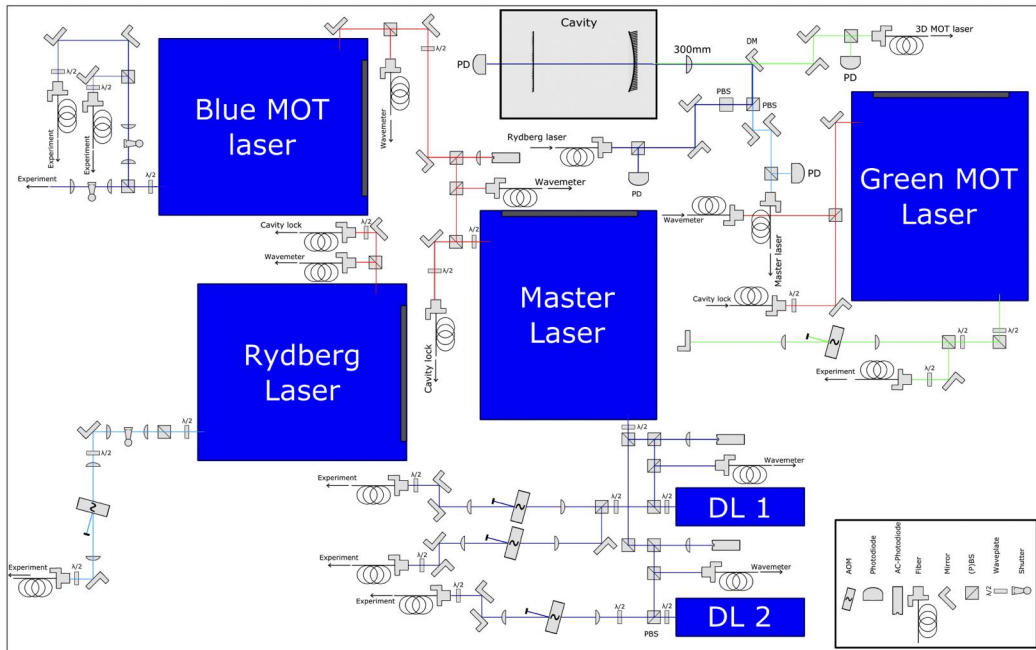
---

[1] Wavemeter WS6/200

Figure 2.1: Setup of the laser table. The Master laser, the Green MOT laser, and Rydberg laser are stabilized to the same reference cavity. The Master laser is used as a frequency reference for the DL 1,2, and the Blue MOT by means of offset lock. The Green MOT laser is utilized for cooling the atoms in the science chamber. The Blue MOT is used for initial cooling in the 2D-MOT chamber and in a core-shell-MOT in the science chamber. The Rydberg laser and the DL 1,2 are used in combination to couple the atoms from ground state to the Rydberg state by a two-photon transition. DL1,2 are further used for imaging the atomic cloud to obtain information about the atomic cloud density and temperature.

an accuracy of 200 MHz. The other branch is overlapped with the master laser for offset locking. The overlapped beams are focused on a fast photodiode[2]. The photodiode signal is further processed on an electronic board[3] which realizes a digital-phase-locked loop. The frequency of the master laser itself is stabilized to a high-finesse reference cavity. The frequency doubled 399 nm light of the blue MOT laser is divided into three branches. The light from the main branch (transmitted on the first PBS) is used for the 2D-MOT. The second branch is used for the science chamber's two-color MOT. The last branch is ultimately used as a push beam. All three branches are fiber coupled and fed to the experiment table.

2.1.2 Green MOT Laser

The green laser system produces light at 556 nm which corresponds to the triplet transition $^1S_0 \rightarrow {}^3P_1$ of Yb. It is utilized for cooling the atoms in the science chamber.

Like for the blue laser described in section 2.1.1, a commercial Toptica DLpro-TA-SHG is also used in this instance. Here, the frequency of the seed diode laser is, however, changed to 1112 nm, and the TA and SHG-cavity are accordingly adjusted. The laser is capable of producing 1560 mW of

---

[2] Hamamatsu Photonics G4176-03

[3] Analog Devices AD4007

green light at the desired wavelength. The integration of the green laser into the complete laser system is visualized in Fig. 2.1. As can be seen, a pick-up of the 1112 nm seed is separated into two branches by a polarizing beamsplitter (PBS) on the left side. One of the branches is coupled to the same wavemeter as the blue MOT laser. The other branch is directly coupled into the high-finesse reference cavity[4] for frequency stabilization. For locking the laser to the reference cavity 1 mW of output power is coupled to a fiber-coupled electro-optic modulator (EOM)[5]. To use the EOM efficiently, a $\lambda/2$-waveplate is used in front of the fibercoupler to rotate the polarization of the laser parallel to the electric field of the EOM. A detailed description of the cavity setup is given in section 5.1. The green MOT laser's frequency doubled 556 nm light is fed through an Acousto-Optic Modulator (AOM)[6] in double-pass configuration, in which the laser light passes through the AOM twice. Several rf-frequency components can be added to the AOM to efficiently boost the capture velocity via the spectrally widened laser light. Eventually, the green beam light is coupled to a single mode fiber and transferred to the experiment table.

2.1.3 Control/Probe Laser

For implementing the Rydberg EIT in our experiment, control and probe lights are needed. The Rydberg laser and the DL 1,2 are combined to couple atoms from their ground state to the Rydberg state via a two-photon transition. The Rydberg laser serves as the strong control laser, excitating the atoms from their intermediate states into a single state in the Rydberg manifold, while the DL 1,2 serve as weak probe beams, coupling the ground state and the intermediate state. Additionally, DL 1,2 are used to image the atomic cloud in order to obtain information about its density and temperature.

The laser setup shown in Fig. 2.1 also features these lasers. As can be seen, one branch of the Rydberg laser is locked to the high-finesse reference cavity using a pick-up of its IR beam, which is coupled through a fiber EOM to the cavity[7]. A second pick-up is coupled into the wavemeter. The main laser beam, which is used to excite the Rydberg states, requires fast switching times in the order of 30 ns. To realize these switching times, interaction coorp AOMs[8] are used. Then, the high power beams are coupled into a phototonic crystal fiber from NKT and transferred to the experiment table. The DL 1 laser is split into four branches. The first one is overlapped with the master laser for digital-offset-locking. The offset lock of the DL 1 laser is performed in the near ultra-violet. The second one is coupled to the wavemeter. The other two branches work as probes and imaging beams, respectively. The DL 2 laser is the same as DL 1 laser except that the latter does not have an imaging branch.

2.1.4 Optical Dipole Trap (ODT) Laser System

To enter the quantum nonlinear regime the blockaded optical depth $OD_{\mathrm{b}} \geq 1$ is required. However, the limitation of the atomic density is a restriction of the OD_{b}. Therefore, an optical dipole trap (ODT) is used in the setup to confine the atoms in the science chamber. Diode-pumped single-mode, linearly polarized CW ytterbium fiber laser systems operating at 1070 nm (IPG, YLR-100-AC-MM) is

---

[4] VH-6010-4 from Stable Laser Systems

[5] EOSpace phase modulator

[6] Gooch and Housego 3080-125

[7] VH-6010-4 from Stable Laser Systems

[8] Intraaction ASM-1501LA8

used here. The maximum power output from the fibre laser head is 100 W. It is located under the experimental table itself and generates the laser light for the Optical Dipole Trap (ODT).
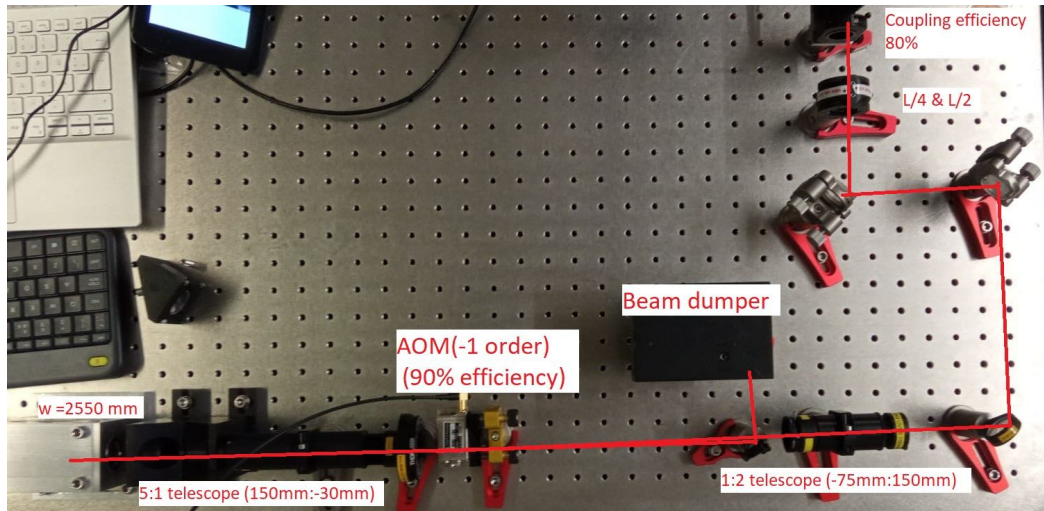

Figure 2.2: Optical setup of Optical Dipole Trap. The laser output first passes through a $\lambda/2$ waveplate before entering a PBS cube. The reflected output of the PBS is dumped into a fire brick. The transmission beam is fed into the AOM in the light path, which is for controlling the pulse shape and duration of ODT. The telescope is used for beam waist magnification, and the $\lambda/2$ and $\lambda/4$ waveplate are used as a polarization modulator.

An overview of the ODT is given in Fig. 2.2. The laser output first passes through a $\lambda/2$ waveplate before entering a PBS cube. The reflected output of the PBS is dumped into a fire brick. This combination of waveplate and PBS is primarily used for alignment purposes. The waveplate is used to dump most of the laser power into the brick and allows for safe working conditions when aligning the main beam. The AOM used in the light path is for controlling the pulse shape and duration of ODT. The aim is to reach a beam waist of 50 m. This can be achieved by utilizing a telescope with twice the magnification. The aim is to reach a beam waist of 50 um. This can be achieved by utilizing a telescope with twice the magnification. A polarization modulator composed of an $\lambda/2$ and an $\lambda/4$ waveplate is applied before the fiber coupler.

2.2 Vacuum system

The heart of the setup is the vacuum chamber shown in Fig. 2.3. Here, ytterbium is pre-cooled in a 2D-MOT in a Titanium chamber and then transferred to the science chamber for laser cooling in a 3D-MOT. Further evaporative cooling can be implemented. A well-designed and meticulously installed vacuum system is critical for producing the extremely high vacuum necessary in the science chamber to avoid excessive atom loss due to collisions with the background gas.

A Yb-MOT can not be efficiently loaded directly from background gas. The vapor pressure of Yb is too low for this approach, and ytterbium sticks to any surface it gets in contact with. Thus, ytterbium experiments use an initial cooling stage to feed the 3D-MOT, either a Zeeman slower or a 2D-MOT (or combination of both). The advantage of the 2D-MOT technique is that it is a simple and compact setup with comparable loading rates to Zeeman slower [14]. In the setup, dispensers
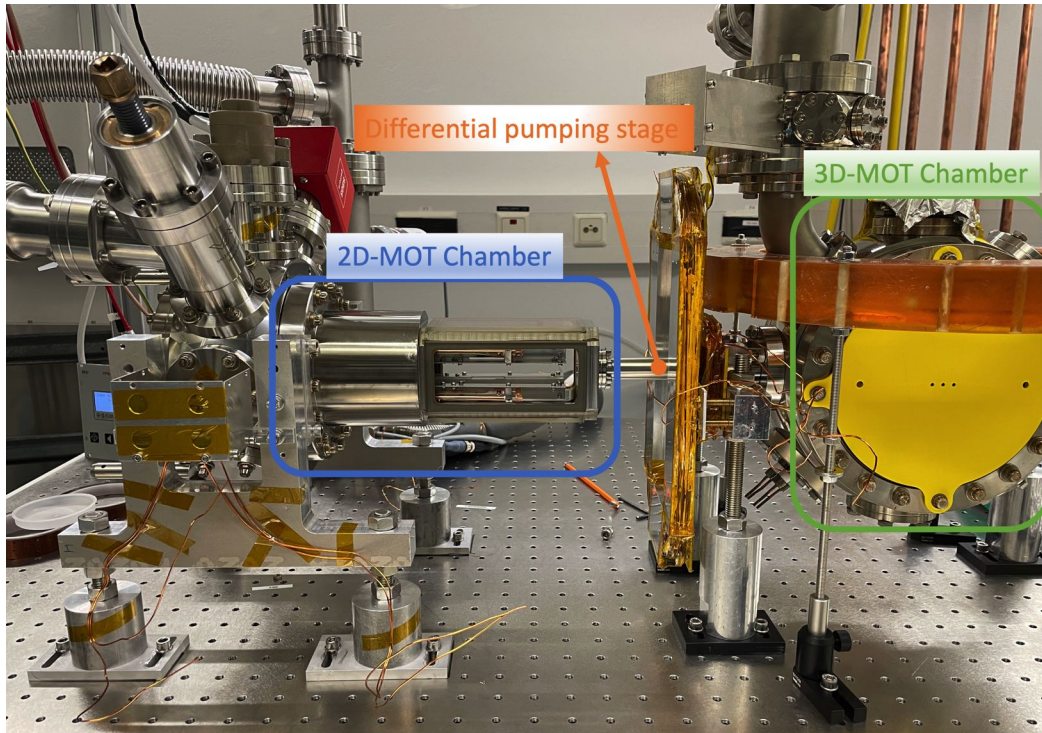
Figure 2.3: The complete experiment setup consists of a dual-chamber approach including a 2D-MOT as a source of cold atoms created in the 2D-MOT titanium chamber. Subsequently, the transversely cold atomic beam is transferred to the science chamber (spherical octagon). Each chamber has a vacuum pump, a valve, and an ion gauge connected. The magnet coils for creating the magnetic field gradient required for the MOT and the compensation coils are not shown here.

are used to load the 2D-MOT. These small reservoirs are heated using a current of 4 A to sublimate the ytterbium atoms from their compound state. Due to the dispensers' tiny size, the 2D-MOT can be constructed in a compact Titanium chamber. Additionally, the flux of atoms entering the science chamber is dependent on the intensity of the laser light in the 2D-MOT, which can be adjusted using acoustic-optical modulators (AOMs) or mechanical shutters. Both chambers are connected via a differential pumping stage to ensure that the science chamber maintains an ultra-high vacuum. It should be noted that the 2D-MOT technique requires relatively high laser power since the broad singlet transition $\Gamma/2\pi = 29.1$ MHz should be saturated for sufficient transverse cooling.

The advantage of using the narrow intercombination transition for the MOT in the science chamber is that the Doppler temperature $T_D = 4.4$ μK is significantly lower. However, this green MOT has a slow capture velocity of around 2 m/s. Atoms flying at this velocity require a 30 ms travel time via the differential pumping stage in our case. As a result, the atoms' trajectory before entering the science chamber is significantly altered by gravity and transverse heating. To prevent these losses, a two-color MOT can be used that boosts the 3D-MOT's capture velocity to around 40 m/s [40]. Gravity and transverse heating have a negligible effect on atoms in these velocity classes. Thus, the horizontal orientation simplifies optics alignment while maintaining the science chamber's atom flux.

2.2.1 2D-MOT Chamber

The main part of the 2D-MOT vacuum system is a titanium chamber mounted on a stainless steel spherical octagon[9] for which the two DN100 ports define the symmetry axis. The part of the 2D-MOT chamber is shown in Fig. 2.4. The titanium chamber consists of a rectangular cuboid with inner dimensions 120mmx50mmx50mm. There are four N-BK7 glass plates[10] glued on the titanium frame. For maximum optical access, dichroic coatings on both sides have been applied to these glass plates. The titanium chamber contains four Alfavacuo 3mm S-type dispensers containing 500 mg each of 99% pure, natural abundance ytterbium. Each dispenser may be addressed individually, and the current returns along independent paths. Consequently, all four dispensers may be run simultaneously if so desired. Each electrical connection is rated for up to 17 A.
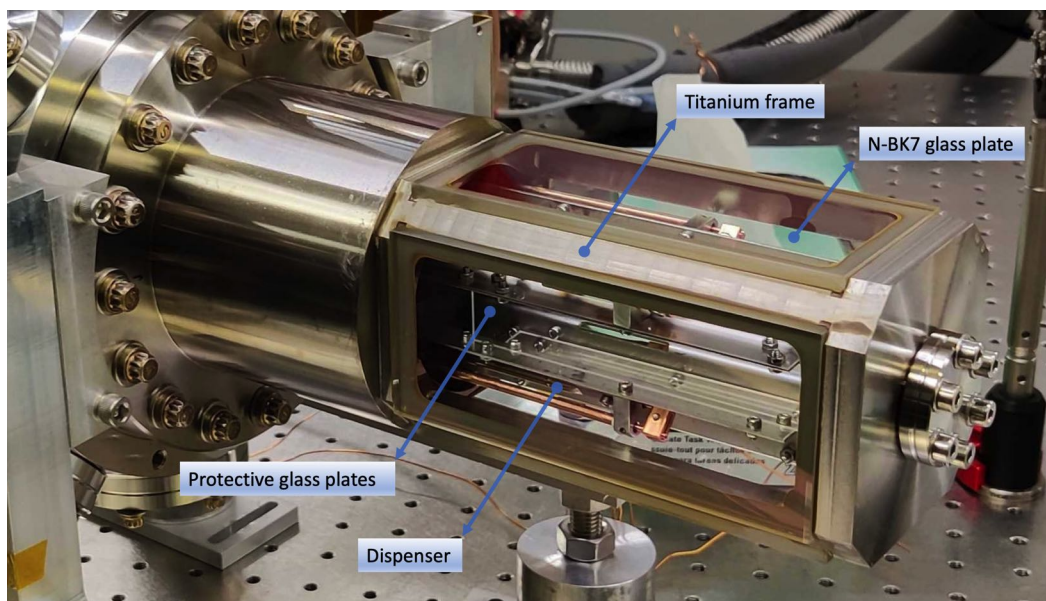

Figure 2.4: The main part of 2D-MOT titanium chamber. There are four N-BK7 glass plates glued on the Titanium frame. It contains four Alfavacuo 3mm S-type dispensers of ytterbium. The protective glass plates are used to protect N-BK7 glass plates from ytterbium atom deposition.

The vapor pressure of ytterbium is extremely small, and it is efficiently adsorbed to any surface at room temperature. Therefore, it is critical to protect these glass plates from deterioration of the optical access caused by ytterbium atom deposition. Stainless steel apertures are installed in front of each dispenser's emission slit to confine the emission angle to the opposite dispenser, as depicted in Fig. 2.5, the emission angle is outlined in. Additional protection is provided by anti-reflection coated glass plates clamped in between the apertures. These plates can be easily re-manufactured and replaced in the case of degradation.

Permanent magnets[11] shown in Fig. 2.5 facilitate the application of strong field gradients that are necessary due to the broad linewidth of trapping transition. The magnets are made out of Neodymium.

---

[9] Kimball physics MCF600
[10] Customized Lens-Optics viewports
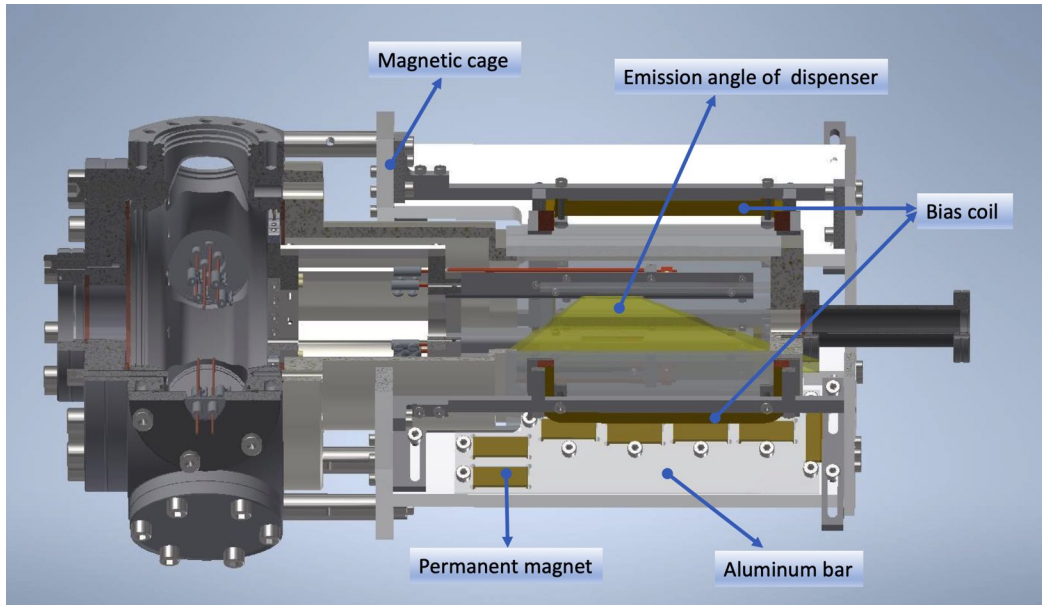[11] Eclipse magnets N750-RB

Figure 2.5: CAD model of the magnet cage enclosing the titanium chamber. The yellow rectangulars represent the permanent magnets. The yellow rectangular frame illustrates the bias coils for compensating constant magnetic fields.

They are stacked in groups of 4 in 7 pockets in an aluminum bar, and clamped in place under an aluminum lid. There are four bars along the diagonals of the chamber. Each bar can be moved independently. The four bars are in mirror-imaged pairs. Magnets should be inserted into each bar such that the bottoms of each bar repel, and the bars are attracted from bottom to top (lid side). With all four panels at the closest position to the cell, the field gradient is calculated to be 57 G/cm.

In Fig. 2.5, the magnetic cage can be assembled individually from the 2D-MOT chamber and then positioned over the titanium chamber. It is mounted on the 2D-MOT chamber's circular octagon. The magnets are arranged in a cross configuration to provide a magnetic field gradient along the atomic beam's zero magnetic field axis. Around the 2D-MOT chamber, there are two pairs of rectangular coils in the Helmholz configuration to generate homogeneous fields in the two directions transverse to the atomic beam. Each coil is rectangular with nominal full inner dimensions of 40x100 mm and 60 turns. These bias coils, used for compensating constant magnetic fields, are also mounted on the magnetic cage. Taking into consideration the distance and diameters of the coils, this results in a magnetic field of 2.8 G/A at the atomic beam's symmetry axis.

2.2.2 Transfer stage

The emission of ytterbium in the 2D-MOT chamber results in a decrease in vacuum pressure, which should be avoided in the science chamber. As a result, a differential pumping stage separates the 2D-MOT chamber from the science chamber in order to maintain a high pressure ratio. Due to the inefficiency of pumping one chamber through the differential pumping stage, each chamber is equipped with a vacuum pump. The 2D-MOT chamber's vacuum pump is connected to the spherical octagon on which the glass cell is mounted, whereas the science chamber's pump is located above the

chamber in a T-cross configuration, which is shown in Fig. 2.5. In the science chamber, a vacuum pressure of 10^{-11} mba is targeted to produce sufficient lifetimes for the atoms in the MOT. As a result, the differential pumping stage diameter d must be modest, as the pressure ratio between the chambers scales with d^3 [41]. The differential pumping stage shown in Fig. 2.6 is designed to have a diameter of d = 7 mm and a length of 150 mm, resulting in a pressure ratio of 300 between the chambers. The length of the differential pumping stage results in a 219 mm distance between the end of the 2D-MOT and the center of the science chamber. Additionally, the diameter of the differential pumping stage enables a push and imaging beam to go through along the atomic axis.
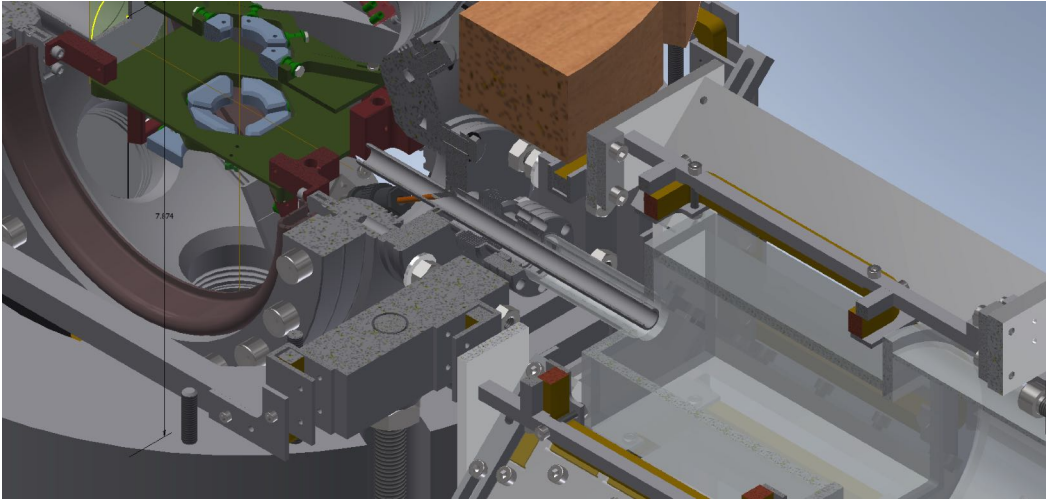

Figure 2.6: CAD model of the transfer stage. The differential pumping tube connects the 2D-MOT chamber and science chamber.

2.2.3 Science Chamber

The science chamber is the core component of the experimental setup for Yb Rydberg physics. The science chamber is a spherical octagon[12] made of stainless steel 316L with six DN40 and two DN160 flange connections and a width of 70.6 mm, as illustrated in Fig. 2.7. The center part of the science chamber is the electric field control, which allows the ionization of the Rydberg atom. The DN160 viewports[13] are made of UV-grade fused silica with antireflection coatings at 394 nm, 399 nm, 532 nm, 556 nm, 578 nm, and 1064 nm, respectively, for the Rydberg laser, the probe and imaging beam, an optional magic wavelength trap, the 3D-MOT laser, an optional clock laser, and the optical dipole trap laser. On the horizontal atomic beam axis utilized for high-resolution imaging, the same coating is applied on a UV grade fused silica DN40 viewport lens. The viewport has a length of 50 mm in vacuum and an inner diameter of 35.6 mm. This design is conducive to achieving the best possible resolution of a lens on the trapped atoms. The distance is limited to 48 mm by the electric field control. The numerical aperture NA = $n\sin(\arctan(d/2f))$ = 0.233, with the refractive index n, the focal length f = 48 mm, and the lens diameter d, is restricted by the first lens and results in a maximum resolution $R = \lambda/2\text{NA}$ = 0.86 μm with an imaging beam on the blue singlet transition 399 nm.

---

[12] Kimball physics MCF800
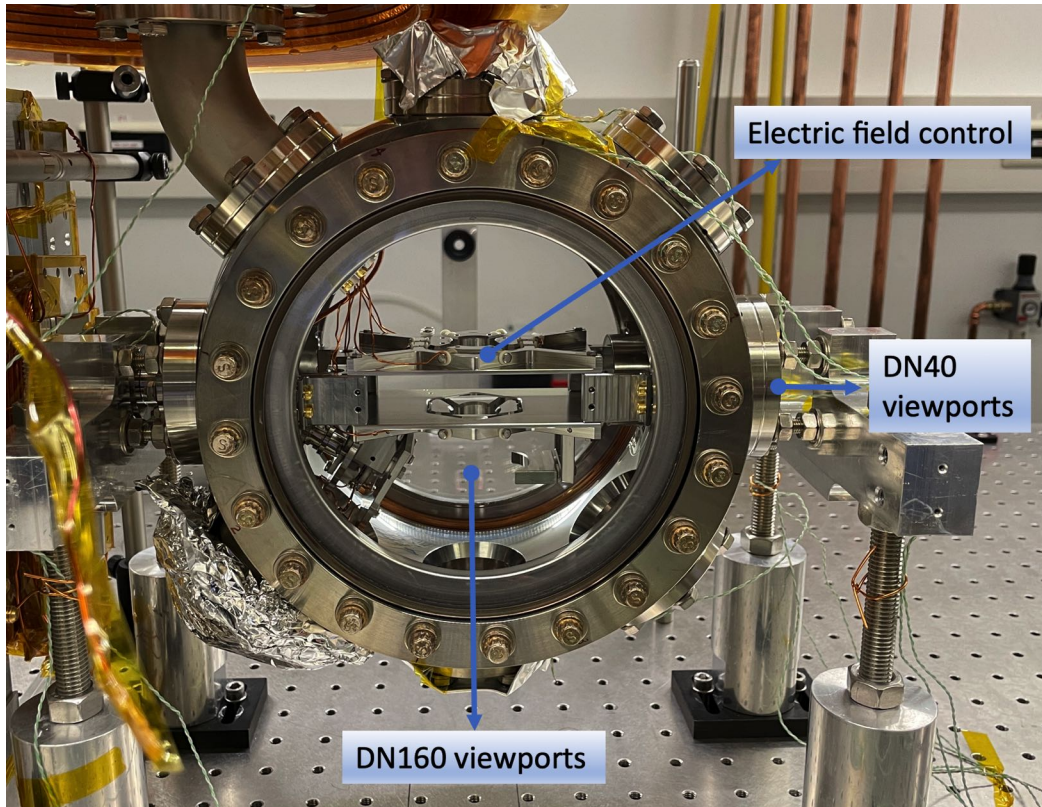
[13] MPF technologies Q21173-6

Figure 2.7: The science chamber is shown with the internal structure and with the key components. For the sake of visibility, the magnet coils for creating the magnetic field gradient required for the MOT and the compensation coils are not shown here. The electric field control allows the ionization of the Rydberg atom. The DN160 viewports are made of UV-grade fused silica with antireflection coatings at 394 nm, 399 nm, 532 nm, 556 nm, 578 nm, and 1064 nm. The same coating is applied on DN40 viewports.

In Fig. 2.8, the setup of the magnetic coils around the science chamber is displayed. When compared to the large singlet transition utilized for the initial transverse cooling in the 2D-MOT, the narrow intercombination transition used for cooling the atoms in the 3D-MOT requires significantly smaller magnetic field gradients. For making the combined blue/green MOT, a quadrupole field with gradients of ca. 10 G/cm on the coil axis and ca. 5 G/cm perpendicular to the coils is required. The MOT coils are composed of Kapton isolated copper wire with a rectangular (4 mm x 4 mm) hollow core (2.5 mm cooling channel). At nominal currents of 26 A, 8 layers of 8 winding turns with an inner diameter of 230 mm and an outside diameter of 344 mm produce magnetic field gradients of 10 G/cm axially and 5 G/cm radially. Holes are made in the socketing to mount them at a fixed spacing of 96 mm apart. Compensation coils are used to adjust the magnetic field by a fixed offset.

2.3 Overview of the Experiment

Up to now, all the core setup including laser systems and vacuum systems, have been illustrated in the former section. However, in order to give an intuitive understanding of this experiment, an overview
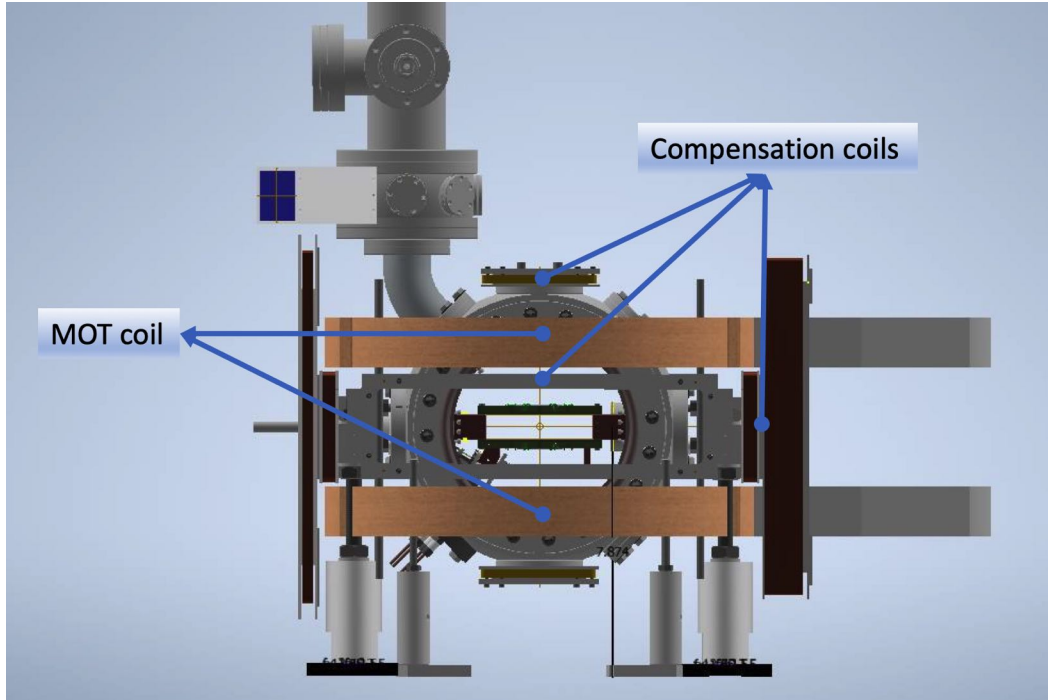
Figure 2.8: 3D modeling setup of Magnetic coils for science chamber. The MOT coils are composed of Kapton isolated copper wire with a rectangular (4 mm x 4 mm) hollow core (2.5 mm cooling channel). Compensation coils are used to adjust the magnetic field by a fixed offset.

of the experiment will be discussed in this section.

The experiment begins by loading atoms into the 2D-MOT using the wide $\Gamma/2\pi = 29.1$ MHz singlet transition $^1S_0 \rightarrow {}^1P_1$. Four orthogonal pairs of retroreflected, counter-propagating laser beams are sent into the 2D-MOT chamber titanium chamber. When a 2D quadruple magnetic field and laser light are combined, a restoring force is created along the zero magnetic field line. In order to reduce the velocity of atoms along the atomic beam axis, two counterpropagating atomic beams are applied to travel along the z-direction.

The atoms are confined and cooled in the science chamber through the narrow intercombination line $^1S_0 \rightarrow {}^3P_1$. This has the benefit of a lower Doppler temperature and a closed cooling cycle over the singlet transition [42]. To be precise, the triplet transition has a Doppler temperature of $T_D = 4.4\mu K$, which is well suited as a starting point for evaporative cooling. However, when a MOT is operated only at the intercombination line, the capture velocity is only $v_c = 2$ m/s [42]. Thus, only a small fraction of atoms can be trapped. Two approaches can be utilized to improve the loading rate and steady state atom number: first, the light from the triplet cooling laser is spectrally broadened using an AOM [42]. By passing the light twice via an AOM, the laser frequency may be spectrally broadened. The AOM is quickly modulated with alternating frequencies. As a result, the laser is modulated with extra frequency components, thus boosting the capture velocity. Second, a two-color MOT can be employed [40]. The fundamental concept is to generate a shell beam of the singlet transition, that is, a beam with zero intensity in the center. This beam overlaps with the triplet transition core beam. Due to the shell singlet transition, it is possible to address and cool high velocity classes. Following that,

20

the atoms reach the triplet transition core volume, where they are cooled to very low temperatures. Consequently, this approach makes use of both cooling transitions: the singlet transition significantly increases the capture velocity and thus the amount of trapped atoms, while the core triplet transition results in extremely low temperatures.

The atoms are then put into a far red-detuned, crossed optical dipole trap, followed by further cooling approaches such as evaporative cooling [43]. When the atoms have reached the final temperature, the Rydberg EIT experiments are performed. A single photon probe beam at a wavelength of 399 nm and a strong counterpropagating control beam at a wavelength of 395 nm are combined to couple the Yb atoms into the Rydberg state. Subsequently, the single photons of the probe beam are detected with single photon counter modules. Furthermore, the electric field control is used to ionize the Rydberg atoms. Then, the ions can be detected on a microchannel plate.

Laser Stabilization

An ideal laser generates an electromagnetic wave with a single well-defined frequency. However, quantum fluctuations in the active laser medium and technical noise result in a finite linewidth of the output spectrum. The Rydberg states' lifetime of ytterbium is above 10 μs [44], which corresponds to the linewidth around kHz. Thus, in order to investigate Rydberg systems with such narrow atomic transitions, lasers need to be frequency stabilized. The output frequency of the laser is neither monochromatic nor steady over time but fluctuates around a mean value owing to noise. Additionally, the mean value may walk randomly. Moreover, the output power also fluctuates due to several noise sources. Noise is mostly induced by variations in the ambient temperature, pressure, vibrations, or fluctuations in the laser's active medium. It is classified into two types: white noise, or frequency-independent noise created by quantum fluctuations, and $1/f$ noise, caused by technical noise sources. The task of laser stabilization is to reduce the technical noise. In our experiment, the Toptica External-cavity diode lasers, which is the laser head of Toptica DLpro-TA-SHG laser, are utilized for laser stabilization. These lasers are composed of a semiconductor laser diode that is temperature stabilized by a thermoelectric-element and an external grating that acts as a refractive element, coupling one frequency component of the output light back into the laser diode to magnify it. The frequency of the laser can be tuned by changing the temperature of the thermoelectric-element, the current of the laser diode, and the angle of the grating. To stabilize the output frequency of a laser to a narrow linewidth, a stable frequency reference is needed to generate an error signal, which is proportional to the deviation of the laser frequency from the reference. This error signal can be fed back to the laser and, therefore the output frequency can be stabilized. The current diode laser compensates for fast frequency drifts, whereas the piezo element of the grating compensates for gradual frequency drifts.

We use two different locking techniques for the different lasers: The Master laser, Green MOT laser and, Rydberg laser are locked to an ultrastable reference cavity using the Pound-Drever-Hall technique (PDH). Blue MOT lasers and DL pro 1/2 lasers are locked via phase-locked with variable frequency offsets to the Master laser. The overall laser lock schemes are summarized in Table. 3.1.

laser	Transition	wavelength (nm)	locking
Master laser	$^1S_0 \rightarrow {}^1P_1$	399 nm	seed laser (798 nm) locked to cavity
Green MOT laser	$^1S_0 \rightarrow {}^3P_1$	556 nm	seed laser (1112nm) locked to cavity
Rydberg laser	$^1P_1 \rightarrow Rydberg$	394 . . . 401 nm	seed laser (788...802nm) locked to cavity
Blue MOT laser	$^1S_0 \rightarrow {}^1P_1$	399 nm	seed laser (798nm) offset locked to Master laser
DL Pro 1 & 2	$^1S_0 \rightarrow {}^1P_1$	399 nm	offset locks to Master laser

Table 3.1: Laser locking schemes.

3.1 Theoretical Background of Pound-Drever-Hall (PDH) Laser Stabilization

This section will discuss the theoretical knowledge required to configure a PDH laser locking. To begin with, essential equations for the description of optical resonators are derived. Following that, the PDH error signal is deduced. Finally, the theory of higher order mode separation in the resonator is explained.

3.1.1 Optical Resonators

Optical resonator traps and stores light at specific resonant frequencies. It can be thought of as a feedback optical transmission system; light circulates or is repeatedly reflected within the system, without escaping. The simplest resonator consists of two parallel planar mirrors through which light is reflected repeatedly with minimal loss. Due to an optical resonator's frequency selectivity, it can be used as an optical filter or spectrum analyzer. Its primary application, however, is as a "container" for laser light generation. The resonator controls the frequency and spatial distribution. Because resonators have the capability of storing energy, they can also be used to generate pulses of laser energy.

A monochromatic wave of frequency ω has a wavefunction

$$E(r,t) = \text{Re}\left[E_0(r)e^{i\omega t}\right], \tag{3.1}$$

with the complex amplitude $E_0(r)$ satisfying the Helmholtz equation

$$\nabla^2 E_0(r) + k E_0(r) = 0 \tag{3.2}$$

and $k = \omega/c$, note that $c = c_o/n$ is the speed of light in the medium. The modes of a resonator are the basic solutions of the Helmholtz equation under the appropriate boundary conditions. For the planar-mirror resonator, the transverse components of the electric field vanish at the surfaces of the mirrors, so that $E(\mathbf{r}) = 0$ at the planes $z = 0$ and $z = L$ where L is the length of the cavity. The solution to this differential equation is a standing wave $E_0(r) = E\sin(kz)$. Applying the boundary conditions, the values of k are limited to a discrete set

$$k_q = \frac{\pi q}{L}, \quad q \in \mathbb{N}, \tag{3.3}$$

This leads to an infinite set of solutions. The value $q = 0$ is associated with a mode that carries no

energy since $k_0 = 0$ and $\sin k_0 z = 0$. The modes of the resonator are therefore the standing waves $E_q \sin k_q z$, where the positive integer $q = 1, 2, \ldots$ is called the mode number. An arbitrary wave inside the resonator can be written as a superposition of the resonator modes, $E(\mathbf{r}) = \sum_q E_q \sin k_q z$. The frequencies are constrained to discrete values. The free spectral range of such a resonator is defined as the distance in frequency space of the adjacent resonances

$$\Delta \nu_{\text{FSR}} = \frac{c}{2L} \tag{3.4}$$

this is only determined by the length L of the cavity. The λ_q represents wavelengths in the medium.

In the presence of loss, however, the waves are not of equal magnitude. For simplicity, we assume that the cavity is symmetrical and that each mirror has a reflectivity of R. The intensity attenuation factor is therefore R^2. Thus $E_1 = hE_0$, where $h = Re^{-I\varphi}$ where $\varphi = 2kL$. The E_2 is related to E_1 by this same complex factor h, as are all consecutive waves. The net result is the superposition of an infinite number of waves, separated by equal phase shifts but with amplitudes that are reduced. It is readily seen that $E = E_0 + E_1 + E_2 + \cdots = E_0 + hE_0 + h^2 E_0 + \cdots = E_0(1 + h + h^2 + \cdots) = E_0/(1-h)$. The intensity in the resonator

$$I = |E|^2 = |E_0|^2 / \left|1 - Re^{-i\varphi}\right|^2 = I_0 / \left[(1 - R\cos\varphi)^2 + (R\sin\varphi)^2\right]$$
$$= I_0 / \left(1 + R^2 - 2R\cos\varphi\right) = I_0 / \left[(1-R)^2 + 4R\sin^2(\varphi/2)\right] \tag{3.5}$$

is found to be

$$I = \frac{I_{\text{max}}}{1 + (2\sigma/\pi)^2 \sin^2(\varphi/2)}, \quad I_{\text{max}} = \frac{I_0}{(1-R)^2}$$

Here $I_0 = |E_0|^2$ is the intensity of the initial wave, and

$$\mathcal{F} = \frac{\Delta \nu_{\text{FSR}}}{\delta \nu} = \frac{\pi \sqrt{R}}{1 - R}. \tag{3.6}$$

is a parameter known as the finesse of the resonator. The finesse of the resonator can be seen as the number of round-trips a single photon takes between the two mirrors. It is defined as the ratio of the free spectral range $\Delta \nu_{\text{FSR}}$ and the full-width-half-maximum (FWHM) of the resonances $\delta \nu$. This is very important. It means that if you want to lock the laser frequency with an extremely narrow linewidth, a resonator with a large finesse is necessary. Due to the imperfection of the mirror, there is a probability that part of the waves leak out each time it is reflected by a mirror. This leads to an exponential decay of intensity given by the characteristic time of τ

$$I(t) = I_0 \exp\left(-\frac{t}{\tau}\right) \tag{3.7}$$

This is related to the finesse as

$$\mathcal{F} = \tau \frac{\pi c}{L} \tag{3.8}$$

Thus, the finesse of a resonator mode can be estimated by observing its decay time. To gain a quantitative understanding, consider an incoming monochromatic electric field $E_{\text{in}} = E_0 \exp(i\omega t)$ with a frequency ω. The reflected electric field from the resonator is $E_{\text{ref}} = E_1 \exp(i\omega t)$ with the

(a) Intensity of the resonator reflection signal.

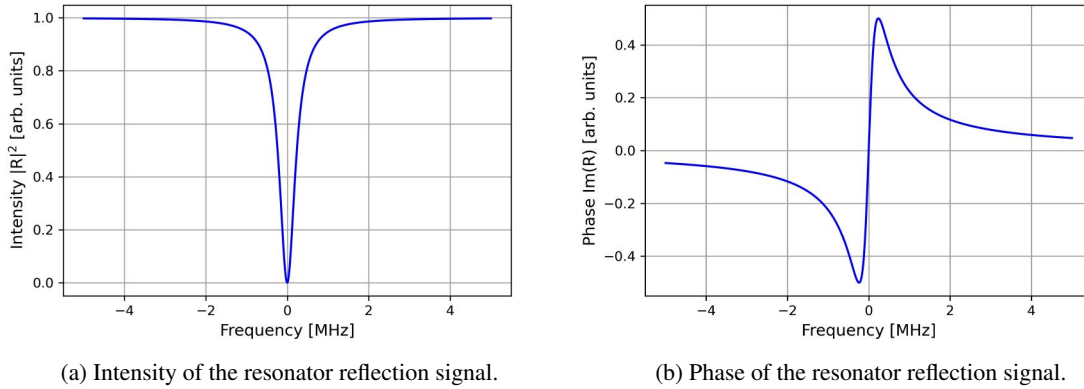(b) Phase of the resonator reflection signal.

Figure 3.1: (a) represents the reflection signal intensity with a dip near resonance caused by destructive interference and (b) is the phase change of the reflected signal when it crosses resonance.

complex amplitude E_0 and E_1. For a symmetric resonator with no losses, the reflection coefficient is

$$\mathcal{R}(\omega) = \frac{E_{\text{ref}}}{E_{\text{in}}} = \frac{\sqrt{R}\left(e^{i\omega/\Delta\nu_{\text{FSR}}} - 1\right)}{1 - Re^{i\omega/\Delta\nu_{\text{FSR}}}} \tag{3.9}$$

with the free spectral range $\Delta\nu_{\text{FSR}}$ and the reflectivity R of each mirror. The intensity of the reflected beam is

$$\begin{aligned} I_{\text{ref}} &= \left|\mathcal{R}E_{\text{in}}\right|^2 \\ &= I_0 \frac{\sin^2\left(\frac{\omega}{2\Delta\nu_{\text{FSR}}}\right)}{(\pi/2\mathcal{F})^2 + \sin^2\left(\frac{\omega}{2\Delta\nu_{\text{FSR}}}\right)} \end{aligned} \tag{3.10}$$

The reflected beam is the coherent sum of two beams, namely the instantly reflected beam at the incoupling mirror and the leakage beam transmitted into the resonator. Notably, the leakage beam splits inside the resonator into a sum of beams that are reflected at different times on the resonator mirrors' interior side. Both beams have the same intensity and frequency in an ideal, lossless, symmetric resonator, but their phase is different. Due to the reflection at the surface of the incoupling mirror, the instantly reflected beam undergoes a phase shift of 180 degrees in relation to the leaking beam in the case of perfect resonator coupling. As a result, the sum of the beams cancels out. The reflection signal is plotted in Fig. 3.1. The transmitted intensity through the resonator can be derived similarly to the reflected beam.

$$I_{\text{trans}} = I_0 \frac{1}{1 + (2\mathcal{F}/\pi)^2 \sin^2\left(\frac{\omega}{2\Delta\nu_{\text{FSR}}}\right)}. \tag{3.11}$$

3.1.2 Modes of Optical Resonator

An optical resonator defines not only the frequency distribution of light, but also its spatial distribution. Prior to determining the coupling optics for mode matching each wavelength to the transfer resonator,

we will briefly discuss the Gaussian-type modes of an optical resonator. The modes of a resonator are the solutions to the paraxial Helmholtz equation under the boundary conditions imposed by the resonator mirrors. The wavefront of the resonator mode at both mirrors has to match the mirror curvatures. The simplest solution of a Gaussian beam at a radial distance ρ from the center axis and axial distance z from the beam focus is given by

$$E(\rho, z) = A_0 \frac{w_0}{w(z)} e^{-\frac{\rho^2}{w^2(z)}} e^{-ikz - \frac{ik\rho^2}{2r_c(z)} + i\zeta(z)} \tag{3.12}$$

with the beam waist w_0, the radius of the beam $w(z)$, the radius of curvature of the wavefront $R(z)$ and the Gouy phase $\zeta(z)$. The intensity of the Gaussian beam, which is proportional to the absolute square of the electric field reads

$$I(r, z) = I_0 \left(\frac{w_0}{w(z)} \right)^2 e^{-\frac{2r^2}{w(z)^2}} \tag{3.13}$$

The beam radius, which is defined as the radius where the radial intensity drops to $1/e^2$, is given by

$$w(z) = w_0 \sqrt{1 + \left(\frac{z}{z_0} \right)^2} \tag{3.14}$$

where w_0 is the beam waist, the smallest beam radius at the focus, and

$$z_0 = \frac{\pi w_0^2}{\lambda} \tag{3.15}$$

is the Rayleigh range, which describes the distance from the focus where the beam radius has increased by a factor of $\sqrt{2}$. The Gouy phase

$$\zeta(z) = \arctan \left(\frac{z}{z_0} \right) \tag{3.16}$$

It is a term that refers to the phase retardation that a Gaussian beam develops when compared to a plane wave of the same frequency. The Gaussian beam is not the only solution to the paraxial Helmholtz equation, which can exist in a resonator. Higher-order modes are described by Hermite-Gaussian beams, which have more complicated radial intensity distributions. Considering the transverse mode indices m and n, the resonance frequencies for the fundamental Gaussian mode, where $m, n = 0$, and higher order Hermite-Gaussian modes, where $m + n > 0$, are given by

$$v_{q,1,m} = q\Delta v_{\text{FSR}} + (n + m + 1)\frac{\Delta\zeta}{\pi}\Delta v_{\text{FSR}} \tag{3.17}$$

Modes which have different longitudinal mode indices q but the same transverse mode indices display the same intensity distribution. Therefore, the longitudinal mode index q is often omitted as it is not important and the possible modes of a resonator are described as TEM_{mn}, where TEM stands for transverse electromagnetic. It is worth noting that the difference of the Gouy phase $\Delta\zeta$ can be determined by means of the boundary conditions. By assuming that mirror curvatures $|R_1| \gg |R_2|$ the expression for $\Delta\zeta$ can be written as

$$\Delta\zeta = \arctan\sqrt{\left|\frac{L}{R_2 - L}\right|} - \arctan\sqrt{\left|\frac{L}{R_1}\frac{R_2 - L}{R_1 + L}\right|} \tag{3.18}$$

For certain values of the Gouy phase shift, e.g. $\pi, \pi/2, \pi/4$, mode frequency degeneracy can occur. To be more specific, as it is shown in Fig 3.2, a $\pi/2$ Gouy phase shift will lead to a $\Delta\nu_{\text{FSR}}/2$ mode spacing and the second mode in the first q family will overlap with the (0,0) mode of the $q + 1$ family, which will lead to degeneracy. In a laser, this can lead to a strong deterioration of beam quality by resonant coupling of the axial modes to higher-order modes. This is also undesired for laser locking as the resonator is used as a reference frequency. However, with proper resonator design, it is possible to avoid at least the particularly sensitive frequency degeneracy. In our design, we use a resonator with a resonator length $L = 100.1$ mm, the mirror curvature $R_2 = 500$ mm and $R_1 \to \infty$. This leads to a frequency spacing of higher transverse modes of 221 MHz. Therefore, the frequency degeneracy can be significantly eliminated, which is shown in Fig. 3.3 and the single fundamental Gaussian mode can serve as a reference frequency for laser locking.
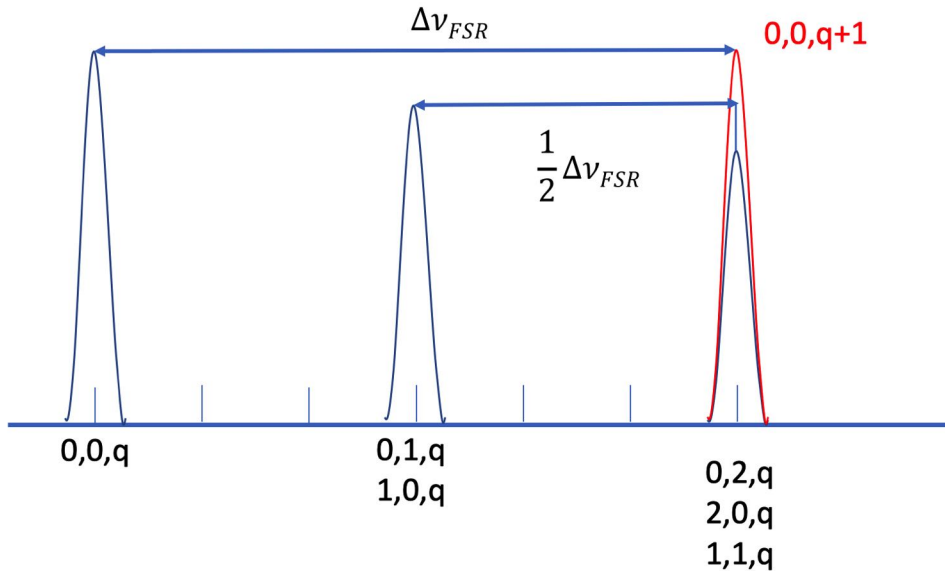

Figure 3.2: Frequency degeneracy in an optical resonator with $\pi/2$ Gouy phase shift.

3.1.3 Pound-Drever-Hall (PDH) Locking Technique

The laser can be locked to the resonance frequency of a cavity. One straightforward method is to lock to the side of a cavity transmission fringe with the highest intensity gradient. However, the transmission light actually goes out after several rounds in the cavity. There is a significant time delay between the transmission light and incident light (on the order of the cavity lifetime, converted to a frequency of tens of kHz). This renders any noise above this frequency incapable of being efficiently removed, thus reducing the effectiveness of this laser-locking method. On top of that, because a change
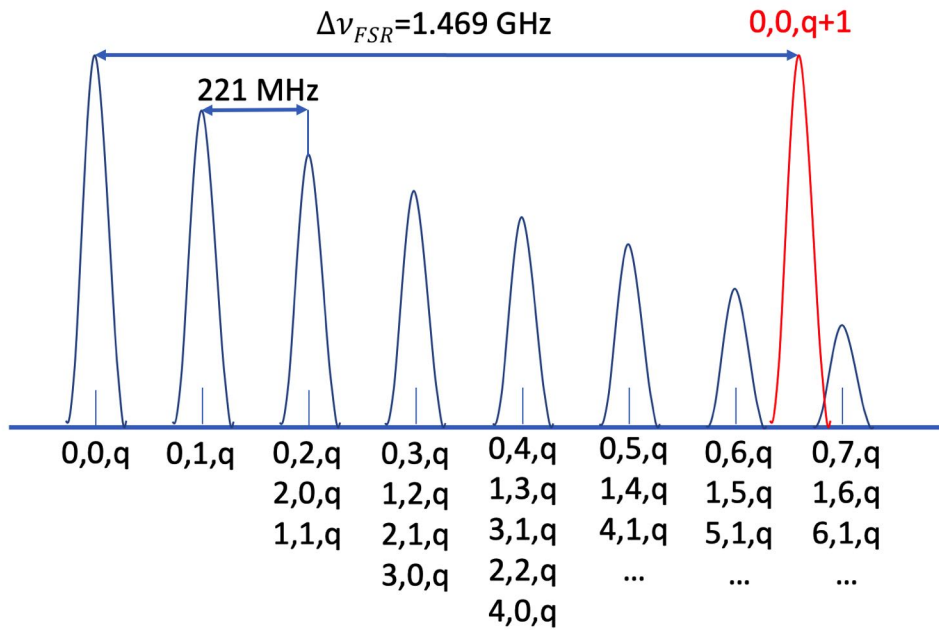
Figure 3.3: Frequency modes in our optical resonator with resonator length $L = 100.1$ mm, the mirror curvature $R_2 = 500$ mm and $R_1 \rightarrow \infty$.

in laser frequency yields a proportional error signal with this approach, it is impossible to distinguish between intensity fluctuations and frequency fluctuations. Instead, one can lock to the center of the cavity reflection signal, which is ideally zero in the absence of losses, enabling the decoupling of laser intensity fluctuations from frequency fluctuations. However, to be able to determine in which direction the laser frequency has to be corrected, an antisymmetric error signal with respect to the cavity resonance is required. The Pound-Drever-Hall (PDH) laser locking scheme, which is one of the most widely-used techniques to frequency-stabilize a laser, provides a solution to overcome these problems. The electronic setup of PDH locking is shown in Fig 3.4. The carrier frequency is modulated with sidebands. The sidebands can be generated via phase modulation of the laser light, e.g. with an electro-optic modulator (EOM). An EOM is similar to a variable waveplate in that it is a crystal that changes its index of refraction rapidly in response to electrical stimuli. This results in a little phase shift in the light traveling through it. The modulation frequency should be considerably greater than the cavity linewidth so that the sidebands are totally reflected when the carrier is close to resonance with the cavity mode. Subsequently, the reflected signal of the cavity mirrors is processed on a photodiode and further modified with a phase-shifter, mixer, and low-pass filter. The error signal is fed back to the laser by a PID controller[1] to lock the frequency of the laser onto a resonance of the cavity.

Now we will introduce the phase modulation into the laser beam mathematically. An EOM modulates the phase of an in coming electric field with an amplitude β and a frequency Ω yields the
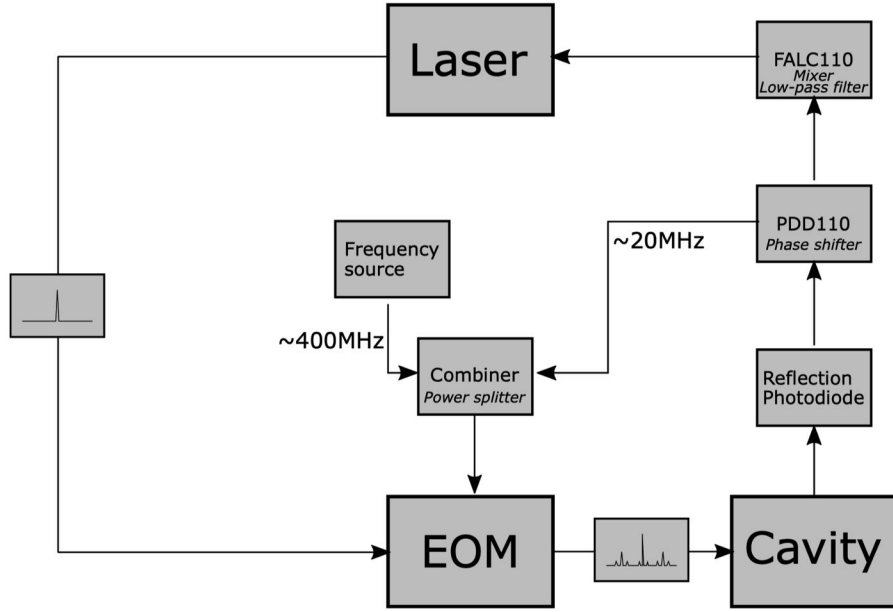
---

[1] FALC 110

Figure 3.4: Electronic setup of PDH locking. The carrier frequency is modulated with sidebands, subsequently the reflected signal of the cavity mirrors is processed on a photodiode and further modified with a phase-shifter, mixer and low-pass filter. The error signal is then fed back to the laser.

expression

$$
\begin{aligned}
E_{\text{in}} &= E_0 e^{i(\omega t + \beta \sin \Omega t)} \\
&= E_0 e^{i\omega t} \sum_{-\infty}^{\infty} J_n(\beta) e^{in\Omega t} \\
&\approx E_0 \left[J_0(\beta) e^{i\omega t} + J_1(\beta) e^{i(\omega+\Omega)t} - J_1(\beta) e^{i(\omega-\Omega)t} \right]
\end{aligned}
\tag{3.19}
$$

Here, the Bessel functions $J_i, i \in \{0, 1\}$ are used and $\beta \ll 1$ is assumed. Therefore, the incoming beam consists of a carrier with frequency ω and two sidebands with frequencies $\omega \pm \Omega$. The reflected beam can be derived as:

$$
\begin{aligned}
E_{\text{ref}} = E_0 \Big[&\mathcal{R}(\omega) J_0(\beta) e^{i\omega t} \\
&+ \mathcal{R}(\omega + \Omega) J_1(\beta) e^{i(\omega+\Omega)t} - \mathcal{R}(\omega - \Omega) J_1(\beta) e^{i(\omega-\Omega)t} \Big]
\end{aligned}
\tag{3.20}
$$

If $P_0 \equiv |E_0|^2$ is the total power in the incident beam, then the power in the carrier is

$$
P_c = J_0^2(\beta) P_0,
$$

and the power in each first-order sideband is

$$
P_s = J_1^2(\beta) P_0.
$$

Then the intensity of the reflected electric field E_{ref} is measured by a photodiode. It yields the power of the reflected beam with mirror reflectivities $\mathcal{R}(\omega)$:

$$
\begin{aligned}
P_{\text{ref}} =& P_c |\mathcal{R}(\omega)|^2 + P_s \left\{ |\mathcal{R}(\omega + \Omega)|^2 + |\mathcal{R}(\omega - \Omega)|^2 \right\} \\
&+ 2\sqrt{P_c P_s} \left\{ \text{Re} \left[\mathcal{R}(\omega)\mathcal{R}^*(\omega + \Omega) \right. \right. \\
&\left. -\mathcal{R}^*(\omega)\mathcal{R}(\omega - \Omega) \right] \cos \Omega t + \text{Im} \left[\mathcal{R}(\omega)\mathcal{R}^*(\omega + \Omega) \right. \\
&\left. \left. -\mathcal{R}^*(\omega)\mathcal{R}(\omega - \Omega) \right] \sin \Omega t \right\} + (2\Omega \text{ terms })
\end{aligned}
\tag{3.21}
$$

The constant terms are caused by interference between the single frequency components. The terms oscillating with the modulation frequency Ω are caused by interference between the carrier and the sidebands, and the terms oscillating with 2Ω are caused by sideband interference. The term oscillating with Ω is particularly intriguing since the sign of the prefactors is sensitive to the detuning of the laser frequency ω to the cavity resonance frequency. This is basically what is required as a feedback signal for laser frequency stabilization. In the case of fast modulation, where the modulation frequency Ω should be greater than the cavity linewidth $\delta \nu$, the reflection coefficients of the sidebands can be approximated by -1, as the sidebands are completely reflected when the carrier is on or close to cavity resonance. The term $\mathcal{R}(\omega)\mathcal{R}^*(\omega + \Omega) - \mathcal{R}^*(\omega)\mathcal{R}(\omega - \Omega)$ is then purely imaginary and the cosine term in eq. 3.21 drops out. The prefactor must be segregated from the oscillation. This is accomplished by multiplying the photodiode and oscillator signals in a mixer. A mixer is an electronic device that essentially multiplies two signals together, multiplying $P_{\text{ref}} \propto \sin \Omega t$ from the photodetector with $\sin \Omega t$ from the oscillator will result in a DC component and a $\cos 2\Omega t$ term. A phase shifter is also needed to compensate for phase shifts due to a delay between the signals. Then, with a low-pass electronic filter, the DC component DC component can be isolated, and this results in the Pound-Drever-Hall error signal:

$$
\epsilon = -2\sqrt{P_c P_s} \, \text{Im} \left\{ \mathcal{R}(\omega)\mathcal{R}^*(\omega + \Omega) - \mathcal{R}^*(\omega)\mathcal{R}(\omega - \Omega) \right\}
\tag{3.22}
$$

In Fig 3.5, the Pound-Drever-Hall error signal consists of a steep slope around zero is given. Due to the extremely steep structure of the error signal, only a small frequency deviation can achieve a significant change in the error signal. Near cavity resonance, the signal can be approximated by a linear function with slope. one can also write the error signal in terms of the regular frequency $f = \omega/2\pi$, which is the deviation of the laser frequency from resonance [45].

$$
\epsilon = D\delta f,
\tag{3.23}
$$

where the proportionality constant D is given by,

$$
D \equiv -\frac{8\sqrt{P_c P_s}}{\delta \nu}
\tag{3.24}
$$

For a fixed incident light, the steepest slope can be achieved by setting the ratio of the sideband power and the carrier power to

$$
\frac{P_s}{P_c} = 0.42
$$

which corresponds to a modulation depth of $\beta = 1.08$. In terms of order of magnitude, excellent cavity

linewidth<100kHz, the corresponding PDH technology can reach 0.01% of linewidth, which is 10 Hz. If there are better electronics (lower electronic noise), it can further reach the level of sub Hz [46].
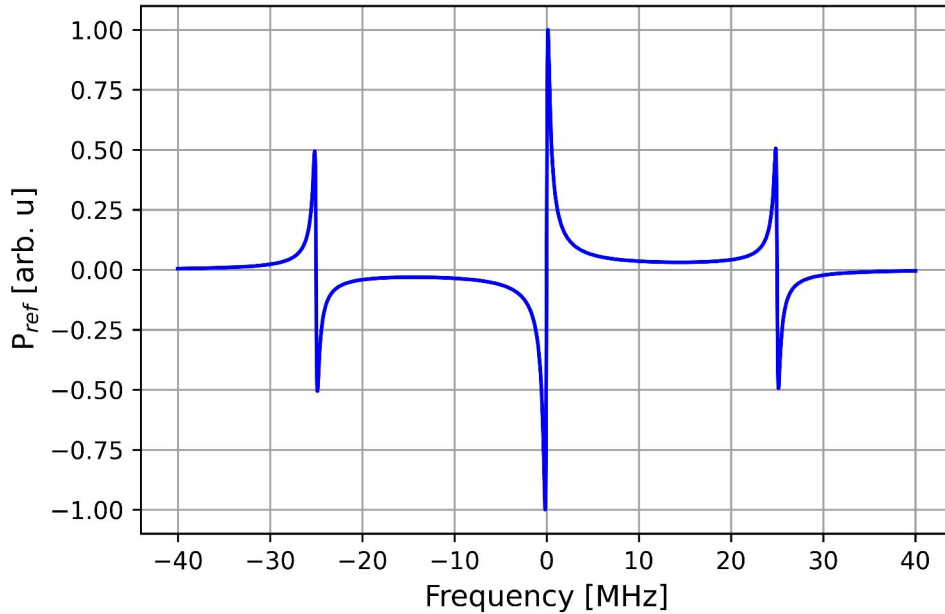

Figure 3.5: Pound-Drever-Hall error signal for a cavity with finesse $\mathcal{F}$ = 39268, a free spectral range $\Delta\nu_{\text{FSR}}$ = 1.5GHz and sidebands at ±20MHz.

Residual Amplitude Modulation

PDH locking stability is often degraded by residual amplitude modulation (RAM), which occurs when modulation sidebands are not perfectly opposite in magnitude or phase, or both. Fluctuation of RAM is an unwanted noise around the modulation frequency, which imposes a limitation on the fidelity of the error signal. RAM is often generated by a mismatch between the polarization of light and one of the major axes of the birefringent crystal within the EOM. The main consequence is that the position of resonance shifts. After the mixer, a DC offset of the error signal is obtained and transmitted back to the laser frequency via the lock. Because the birefringence in the crystal is temperature dependent, temperature changes in the lab can cause changes in RAM and hence in the DC offset of the PDH error signal. As a result, the laser locking point shifts with temperature. There are several methods for reducing RAM as a result of the phase modulation process, such as temperature-stabilizing EOMs used in locking configurations. It is also advantageous to employ an EOM with two crystals in a compensation configuration. The two crystals are rotated 90 degrees in relation to one another, so that temperature dependent birefringence changes in the first crystal are compensated for by anti-correlated birefringence changes in the second crystal.
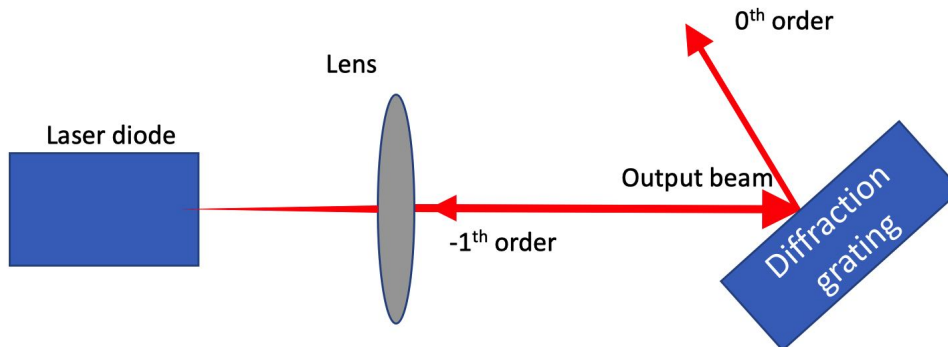
Figure 3.6: ECDL in Littrow configuration: The light diffracted (1st order) at the grating is sent back into the laser.The 0th diffraction order is used as the new output beam to be sent to the experiment.

3.1.4 Feedback Elements of Lasers

Stabilization of diode lasers can be accomplished by feeding back signal to a diffraction grating and the injection current of diode. As illustrated in Fig.3.6, a diffraction grating is positioned outside the laser cavity in an extended-cavity diode laser (ECDL) configuration. This type of grating enables frequency-selective feedback to the laser cavity, forcing the diode into single mode operation and allowing for wavelength tuning via grating angle control. The equation can be used to describe the diffraction at the grating.

$$n\lambda = d\left(\sin(\theta) + \sin\left(\theta'\right)\right) \tag{3.25}$$

where n is the order of diffraction, d is the grating constant, and $\theta\left(\theta'\right)$ is the angle of incidence (diffraction) of the beam with respect to the normal of the grating. The grating is positioned in such a way that the first order of the diffracted light of a certain wavelength is fed back into the laser cavity. As a consequence, the emission of more photons at the desired wavelength is stimulated, which also allows for the lasing of modes that are not in the center of gain profile. Typically, the diffraction grating is positioned atop a piezo to allow for precise frequency control. Frequency control is facilitated via the injection current feedback to diode. The mechanism is as follows: a change in current density in a diode leads to a change in temperature and refractive index, which alters the frequency of emitted light.

3.1.5 Feed Back Loop of Laser Stabilisation

Ideally, one would prefer to reduce the frequency noise of the laser across the whole spectrum; practically, this is plainly unachievable due to the limiting bandwidth of the feedback loop. However, the frequency noise in different parts of the spectrum adds to the linewidth of a laser in very different ways [47]. In this paper, the high modulation index area is defined as $S(f) > 8\ln(2)f/\pi^2$, where $S(f)$ is frequency noise spectral density and f is frequency. Noise in this regime contributes to the laser linewidth, resulting in a Gaussian line shape. In the low modulation index area, where

$S(f) < 8\ln(2)f/\pi^2$ the noise contributes only to the wings of the line shape, but not the linewidth [47]. This has the significant implication that, in order to reduce the laser linewidth, it is necessary to suppress the laser frequency noise up to a frequency on the order of the initial linewidth of the laser.

As already described earlier, the error signal obtained by the Pound-Drever-Hall technique is fed back to the laser by a controlling device. The feedback loop is implemented using a commercial PID controller from Toptica, the FALC 110. The principle of operation of this high-bandwidth device is depicted in Fig. 3.7. After adding the error signal to the controller, two trim-pots can be used to modify both the amplitude and the offset using a gain factor of between 1 and 10. Following this stage, the signal is divided into two different amplifier branches with varying bandwidths. The overall transfer function of the fast circuit branch is set by configuring three different lag-lead filter stages (called Limited Integrators: Extra Slow, Slow and Fast) and a lead-lag filter (called Fast Limited Differentiator) in a row. The term "limited gain" refers to the fact that the gain of these elements is limited to a specific value and does not reach zero or infinity. The gain slopes of the individual filter stages are shifted along the frequency axis by setting the PID switches. For lower frequencies, this architecture enables the progressive gain increase of the controller via the three integrators. Due to the limitations of integrators, one may verify that the gain is not excessively high for high frequencies and is increased solely for low frequencies. On the other hand, the limited differentiator enables the control circuit's phase shifts at high frequencies to be reduced. The second Unlimited Integrator Branch is made up of a single unlimited integrator. Additionally, there are multiple dip switches that can be used to set the slew rate of the integrator to a certain value. This branch is critical for low frequencies of laser, as its gain reaches extremely high values at these frequencies. The advantage of this PID-controller design is that the two branches can be used as feedback for the piezo and the laser diode. It is self-evident that the fast branch should be used as feedback for the laser diode and the unlimited branch for the piezo element. This technique ensures that the piezo element compensates for slow laser frequency drifts, while fast variations are compensated by altering the laser diode current.
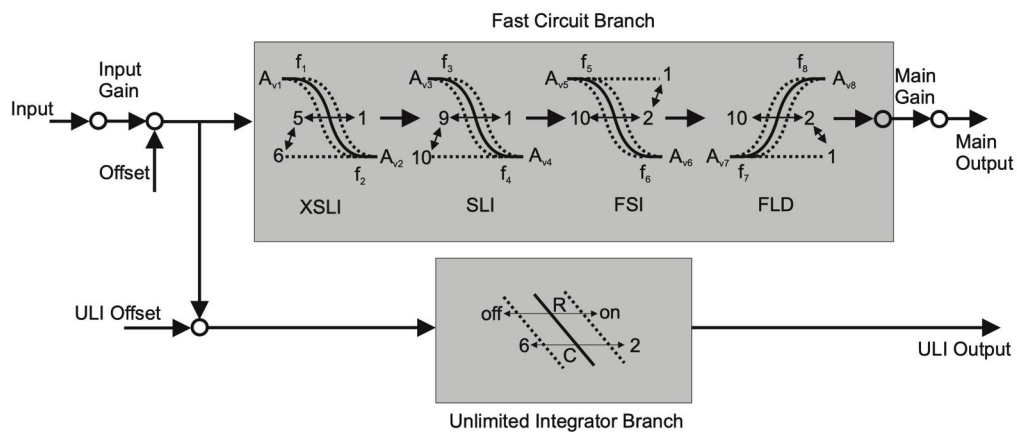

Figure 3.7: Diagram of the electronic setup of the FALC 110[from the manual]. This feedback loop is split into a fast and a slow branch. These horizontal arrows denote corner frequencies.

3.2 Locking Laser to an External Cavity

3.2.1 Mode Matching

To couple to the fundamental mode of the cavity, the incoming beams from the outside have to be mode-matched to the cavity modes at the respective wavelengths. The light from the EOM fibers must be aligned with the calculated spot sizes on the flat mirror for each laser. A fiber collimation lens for each fiber and a single common coupling lens in front of the cavity is the most basic configuration. The beams from the fibers are not collimated to reach the correct spot size for each wavelength; instead, the fiber-outcoupling lenses are slightly misaligned to get the correct beam size on the cavity coupling lens for each wavelength. It is also necessary to incorporate the curved first mirror, which serves as a plano-concave lens for the incoming beam. The required focal lengths for the fiber coupling lenses and the lens positions can be calculated with the program "Gaussian Beam Calculator". An example for 800 nm is shown in Fig. 3.8. Actual lenses and positions used in the setup are shown in Table 3.2.
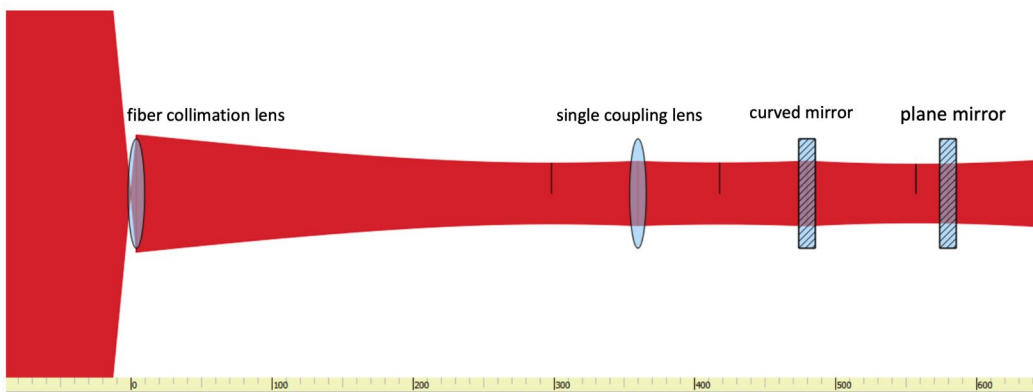
Figure 3.8: Mode matching design for the 800 nm laser. The outcoupling lens is followed by the mode matching lens focusing on the plane mirror after passing through the curved mirror.

3.2.2 Optical Setup of Cavity Lock System

A plano-concave cavity from the company Stable Laser Systems[2] with a plane $R_1 = \infty$ and a concave mirror $R_2 = 500$ mm is employed in this experiment to stabilize the frequency of the Master, Rydberg, and 3D MOT lasers. The finesse of this cavity is 40000, and it has been carefully characterized in Philipp-Lunt's thesis [48]. The optical configuration is depicted in Fig. 3.9. The mirrors are spaced 100 mm apart using an ultra-low-expansion (ULE) glass spacer. Because the thermal expansion coefficient of ULE glass has a zero crossing point at $T_C = 30.7°$C, the cavity is constantly heated using Peltier elements to that temperature to ensure that the mirrors' distance discrepancies are as small as possible. Anti-reflection coatings are used on the mirrors at 798 nm, 790 nm, and 1112 nm. For temperature and vibration isolation, the optical resonator is mounted on a block of Zerodur. This assembly is housed in an aluminum enclosure and pumped to a pressure of 10^{-8} mbar. To minimize thermal expansion caused by incoupled light heating, each laser beam has a power of $P_{\text{Master}} = 40 \, \mu$W, $P_{\text{Rydberg}} = 43 \, \mu$W and $P_{\text{3DMOT}} = 100 \, \mu$W.

---

[2] VH-6010-4 from Stable Laser Systems

Majestix-798nm (Idefix is the same)		
Component	Focal length	Position [mm]
Fiber	waist w = 2.5μm	x = 0
Fiber coupling lens - C160TME-B	f = 4.0 mm	x = 4.04 mm − 4.05 mm
coupling lens - AC254-300-B-ML achromatic doublet	f = 300 mm	x = 383 mm
Mirror 1[R = 500 mm]		x = 540 mm
Mirror 2		x = 640 mm
Asterix-1112nm		
Component	Focal length	Position [mm]
Fiber	waist w = 3.3μm	$x = 0$
Fiber coupling lens - C340TMD-B	$f = 4.03$ mm	$x = 4.07$ mm − 4.08 mm
coupling lens - AC254-300-B-ML achromatic doublet	$f = 300$ mm	$x = 335$ mm
Mirror 1[$R = 500$ mm]		$x = 116.5$ mm
Mirror 2		$x = 551.5$

Table 3.2: Lenses and positions used for mode matching.

To couple all three lasers into the cavity, the laser beams are overlapped. A PBS[3] is used for the Rydberg and Master laser and a dichroic mirror[4] for the 3D MOT laser. To avoid crosstalk between the reflected beam of the Master and the Rydberg laser, an additional PBS cube is positioned perpendicularly. As a result, this cube functions as a filter for horizontally polarized components. A lens with a focal length of f = 300 mm is positioned in front of the cavity such that the radius of curvature of the wavefronts of the in-coupling laser beams matches the curvature of the plano-convex mirror, and the waist matches the planar mirror. The photodiode behind the cavity detects the transmission signal through the cavity, which is used to optimize cavity coupling and monitor the laser locks. Three different photodiodes detect the reflected signals of each laser and subsequently process it to generate the PDH error signal for the Master, Rydberg, and 3D MOT lasers, respectively.

Since the cavity is ultrastable, it provides fixed locking points in frequency space separated by the free spectral range of the resonator. The PDH sidebands are modulated at the carrier frequency of the cavity-locked lasers using the EOM from EO SPACE[5]. The core part of this EOM is a lithium niobate crystal. The refractive index of a crystal depends on the local electric field. As a result, the phase of the outcoupled light is altered as it passes through the crystal. The frequency of the laser light is regulated by modulating a sinusoidally fluctuating electric field on the EOM. For the applied PDH frequency, the outcoupled laser has symmetrical sidebands. In our case, these are 15 MHz, 20 MHz, and 25 MHz of the Rydberg, 3D MOT, and master laser.

3.2.3 Cavity Signal

As described in Subsection 3.1.2, the basic Gaussian mode of the reference cavity is used for laser locking. The goal of achieving optimal coupling into the cavity is to align so that only the fundamental TEM_{00} Gaussian mode survives. It is a challenging work to find the initial signal through the cavity.

---

[3] Thorlabs B-coated PBS cube

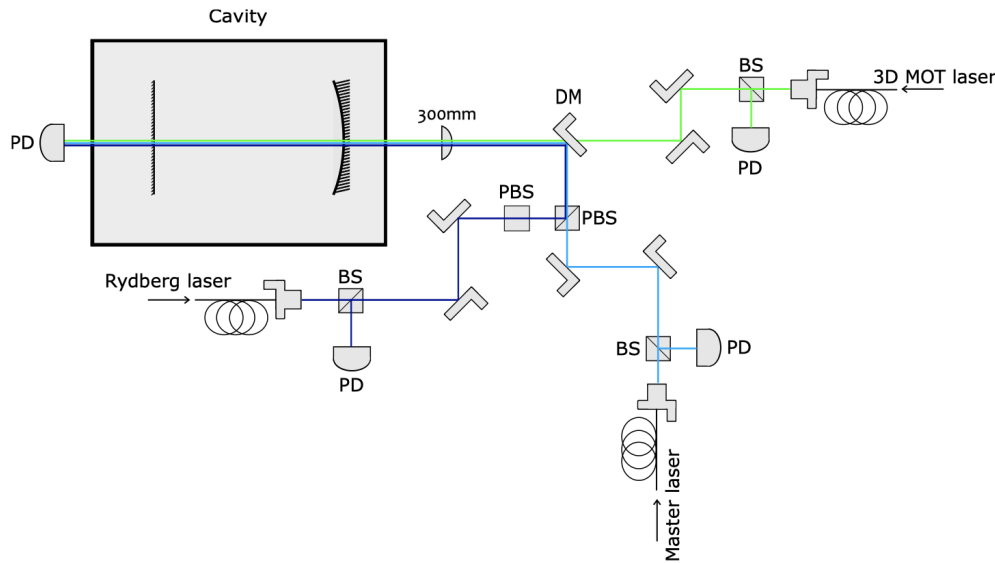[4] Thorlabs DMLP900

[5] Ser.No. 439613

Figure 3.9: Optical setup of the PDH locking system. All three laser beams are overlapped with a polarizing beam splitter (PBS) and a dichroic mirror (DM). The transmission signal is detected on a photoiode (PD). The reflected signal is detected by three different PD separately.

To obtain this, a camera and a photodiode which connected to an oscilloscope, are needed. A 50:50 beamsplitter behind the cavity is placed to have a signal on the photodiode and camera simultaneously. First, the laser is scanned over a free-spectral range, i.e. 1.5 GHz, to make sure there is a cavity resonance somewhere throughout the scan. When aligning on the camera a scan rate of a handful of Hz is used. The camera is utilized to detect the transmitted light. Usually, the first signal is a higher order mode. With the help of the two in-coupling mirrors, each laser beam can be coupled into the ultra stable cavity such that the fundamental mode (TEM_{00} Gaussian mode) of the cavity is excited. The transmitted beam of the cavity is directed onto a camera[6] to visualize the excited cavity modes. Once the fundamental mode of the cavity is excited, a bright round shape can be observed in the camera as shown in Fig. 3.10.

Note that it is not possible to align only on the camera since the fundamental mode will saturate the camera, and a signal from a few higher order modes may stay undetected. A photodiode coupled to an oscilloscope is used. If the fundamental mode is visible on the camera, it should be the highest peak on the oscilloscope. The transmission signal is shown in Fig. 3.11. In order to have better locking performance, cavity coupling is optimized such that all the higher order modes in the cavity are minimized up to the order of the noise level.

3.2.4 Characterization of the RF Sources of PDH Locking

Since the cavity is passive (and ultrastable), it provides fixed locking points in frequency space separated by the free spectral range of the resonator (1.497 GHz). To lock the lasers (almost) anywhere,

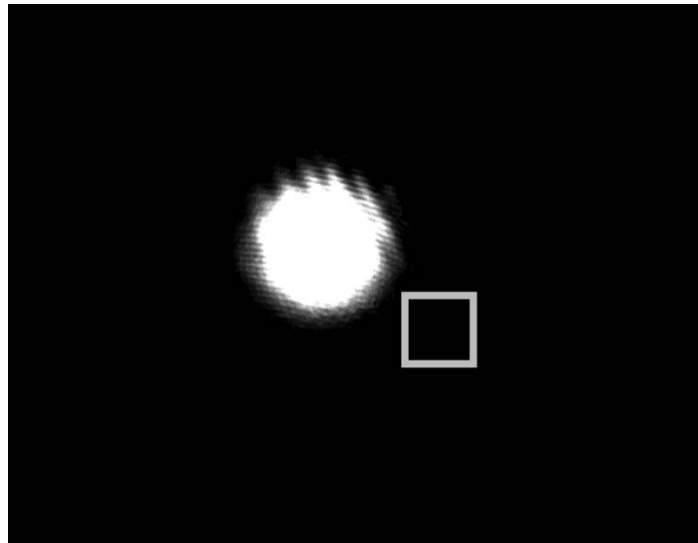---

[6] Unibrain Fire-i 530b
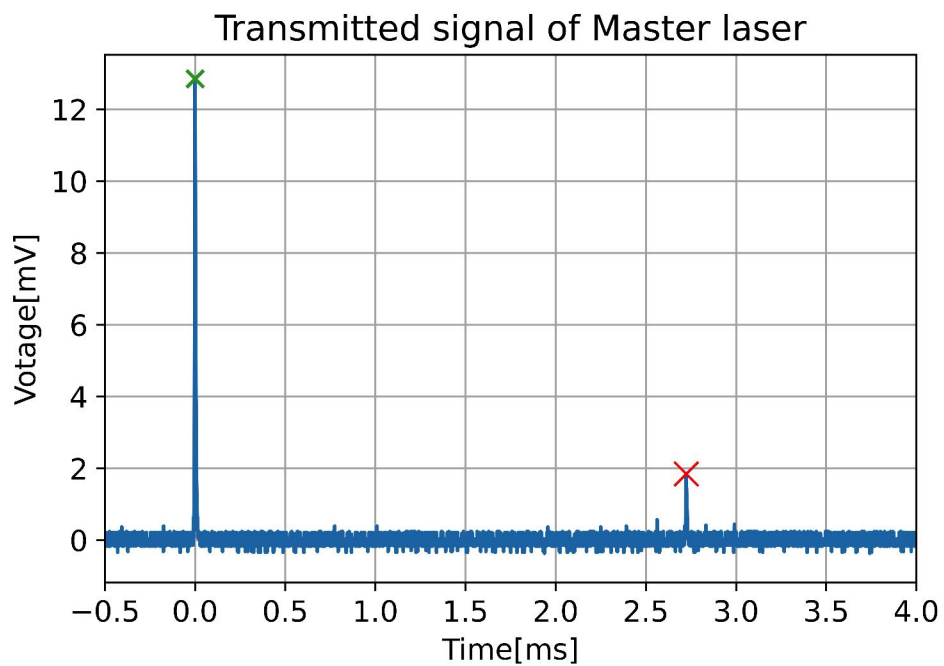
Figure 3.10: Fundamental Gaussian mode on Camera.

Figure 3.11: The transmission signal of the cavity. The carrier frequency is marked with a green cross, and the higher mode is marked with an red cross. After the optimization of cavity coupling, all the higher order modes should be on the order of the noise level. The x-axis is scan of the laser and hence time corresponds to the frequency of the laser.
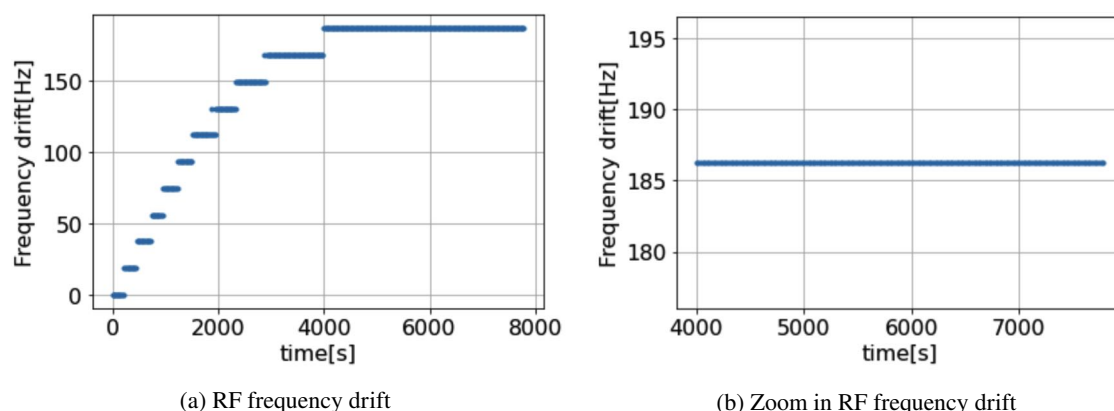
(a) RF frequency drift

(b) Zoom in RF frequency drift

Figure 3.12: (a) shows the frequency drift of RF source, and (b) shows a zoom in frequency drift of RF source.

we use broadband fiber EOMs from EO SPACE[7]. The laser frequency is modified by an extra sideband provided by an rf-source. The frequency distance of the rf-sideband can be set in the range of 50 to 750 MHz. The laser is locked to one of the rf-sidebands with a frequency offset from the carrier frequency. If this frequency of the sideband is changed while the laser is locked, the laser can only compensate by altering its actual frequency, which means that the laser's output frequency can be scanned by altering this modulation frequency. For frequency source, we use broadband rf-generators SynthUSBII (34.4MHz - 4.4GHz) from Windfreak. First, the rf-source at room temperature was switched on, and we measured the frequency drift of rf-source for a long time. In Fig. 3.12, it shows that before 4000 seconds, the frequency of rf-source gradually improved with time, and after 4000 seconds, the frequency reached a stable plateau. This is because of the temperature dependent accuracy of the crystal oscillator inside the RF source Windfreak SynthUSB. Only after 4000 seconds of working time will the crystal reach a stable working temperature so that the crystal has good accuracy of frequency. This is important because every time one turns on the rf-source, one needs to wait for it to reach the proper working temperature.

3.3 Measurement of the Laser Linewidth

In the previous sections, the PDH method for locking the laser was presented. There are several methods to characterize/measure the linewidth of a laser, but with the help of in-house equipment, we did chose to employ the optical heterodyne detection scheme with two lasers. A short introduction to heterodyne detection and the limitations of the resolution with a Fast Fourier transform (FFT) oscilloscope will also be given.

Optical Heterodyne Detection

Optical heterodyne detection is a technique for determining laser linewidth. The basic principle behind this is that two laser beams from near identical frequency lasers are overlapped. This results in an oscillation at the difference and sum of the two frequencies if the spatial distributions overlap

---

[7] Ser.No. 439613

and the polarization is not orthogonal. The sum frequency of the lasers is optical in nature and thus inaccessible to electronics. The beat frequency, on the other hand, can be in the MHz-GHz range and is thus resolvable using an FFT oscilloscope. The setup for the heterodyne linewidth measurement is quite simple and illustrated in Fig. 3.13. First, the frequency of the Rydberg laser was shifted from 790 nm to 798 nm. The branch of the 798 nm Rydberg laser is overlapped with the Master laser running at nearly the same frequency. The beat note signal of the two overlapped laser beams is detected with an AC coupled fast photodiode[8] from Hamamatsu, and the fast photodiode signal is connected to a high bandwidth oscilloscope[9] with FFT features.
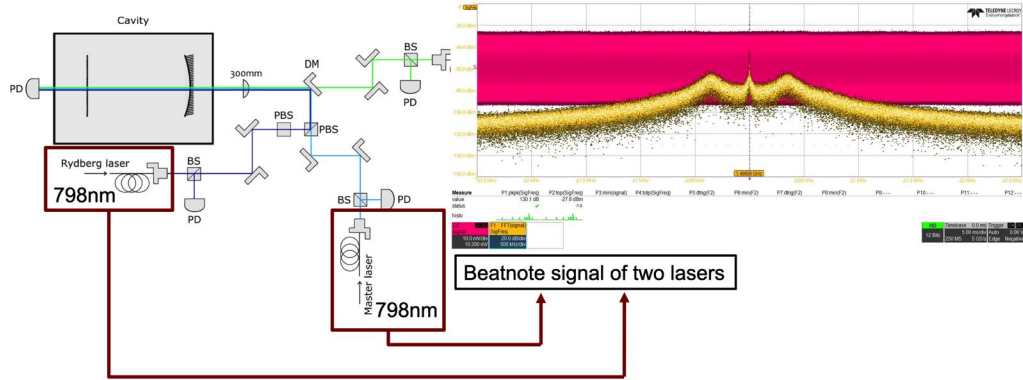
Figure 3.13: The setup for the heterodyne linewidth measurement. A branch of Rydberg laser is overlapped with the Master laser. With a fast AC-coupled photodiode the signal of the overlapped beams is detected and visualized on an FFT oscilloscope. The yellow curve is the beatnote signal at 1.4966 GHz.

The electric field of the two lasers beams can be denoted by,

$$E_{1/2} = \text{Re} \left[E_{0,1/2} e^{i\left(\omega_{1/2} t + \varphi_{1/2} \right)} \right] \tag{3.26}$$

then the intensity of the two overlapped beams measured by the AC coupled fast photodiode is given by:

$$I(t) = \left(E_1(t) + E_2(t) \right)^2 = E_1^2(t) + E_2^2(t) + 2E_1(t)E_2(t). \tag{3.27}$$

The first two terms represent the constant intensity, whereas the last term is a result of the interference of the two electric fields. The constant terms are filtered out by the AC photodiode. The power spectral density, which is detected with an FFT oscilloscope can be calculated with the help of the Wiener-Kintchin theorem. It claims that the power spectral density S is equal to the Fourier transform F of the autocorrelation G [49], which is given below:

$$S_I(\omega) = \mathcal{F} \underbrace{\left\langle I_x(t) I_x(t+\tau) \right\rangle}_{G_I(\tau)}. \tag{3.28}$$

This equation can be stated in such a way the power spectral density S of the beat note can be expressed

---

[8] Hamamatsu G4176-03
[9] Lecroy WavePro DSO

in terms of the power spectral density of the two laser fields.

$$S(\omega) = \left(S_{E_1} \otimes S_{E_2}\right)(\omega). \tag{3.29}$$

The beat note signal provides immediate access to the laser linewidth measurement. The finite linewidth is caused by white noise generated by quantum fluctuations and 1/f-noise generated by technical noise. White noise produces a Lorentzian shaped laser spectrum, whereas 1/f-noise produces gaussian broadening. Both sources of noise contribute to the finite laser linewidth, resulting in a Voigt profile. The normalized Voigt function can be written as:

$$S_\mathrm{V} = \left(S_\mathrm{G} \otimes S_\mathrm{L}\right)(\omega) \tag{3.30}$$

This is a convolution of a Gaussian and Lorentzian curve. The linewidth of the of the Voigt profile reads [50],

$$\Delta\omega_\mathrm{V} = 0.5346\Delta\omega_L + \sqrt{0.2165975\Delta\omega_L^2 + \Delta\omega_G^2} \tag{3.31}$$

where $\Delta\omega_\mathrm{G}$ is the Gaussian linewidth and $\Delta\omega_\mathrm{L}$ the Lorentz linewidth.

$$\Delta\omega_\mathrm{G} = 2\sigma\sqrt{2\ln 2}$$

$$\Delta\omega_\mathrm{L} = 2\Gamma$$

Resolution of FFT Oscilloscope

Similar to the display of a spectrum analyzer, the FFT oscilloscope can be used to convert the time domain to the frequency domain. In contrast to the spectrum analyzer, where the resolution bandwidth (RBW) and video bandwidth (VBW) can be adjusted, the FFT span is defined by the sampling rate. Three critical factors define the FFT spectrum on an oscilloscope: the Nyquist frequency f_Ny, which defines the frequency span, the frequency resolution Δf, and the capture time of oscilloscope t_cap, which defines the time period over which the waveform is captured. The frequency range of FFT oscilloscopes begins at 0 Hz and increases to the span frequency. As a result, f_Ny represents the highest frequency represented in the frequency domain. The number of sample points N and the sampling period in the time domain ΔT can be chosen as beginning values. These parameters are related in the following way [51]:

$$
\begin{aligned}
f_\mathrm{Ny} &= \frac{1}{2\Delta T} \\
t_\mathrm{cap} &= N\Delta T \\
\Delta f &= \frac{1}{t_\mathrm{cap}} = \frac{1}{N\Delta T}
\end{aligned}
\tag{3.32}
$$

As a result, the frequency resolution can be improved by increasing the number of sample points N or by increasing the sampling duration ΔT. Choosing a longer sample period, on the other hand, counters the Nyquist frequency, resulting in a narrower frequency span. Thus, given a default memory length of N, a sample period, a tradeoff must be made in order to achieve a high Nyquist frequency

with decent resolution.

Beat Note Signal

In Fig. 3.14 the beat note signal of the master and Rydberg laser is shown for the case where the two lasers are locked to adjacent cavity modes. The beat frequency is f_{beat} = 1.4966 GHz, which is in very good agreement with the theoretical value of FSR of cavity$\Delta \nu_{\text{FSR,theo}}$ = 1.497 GHz. One may find there are two lower peaks in Fig. 3.14; these are servo bumps. The servo bumps originate from the finite bandwidth of the feedback loop. It specifies the time scale on which the lock is capable of reacting to distortions, and it can be modified by changing the parameters of the PID controller.
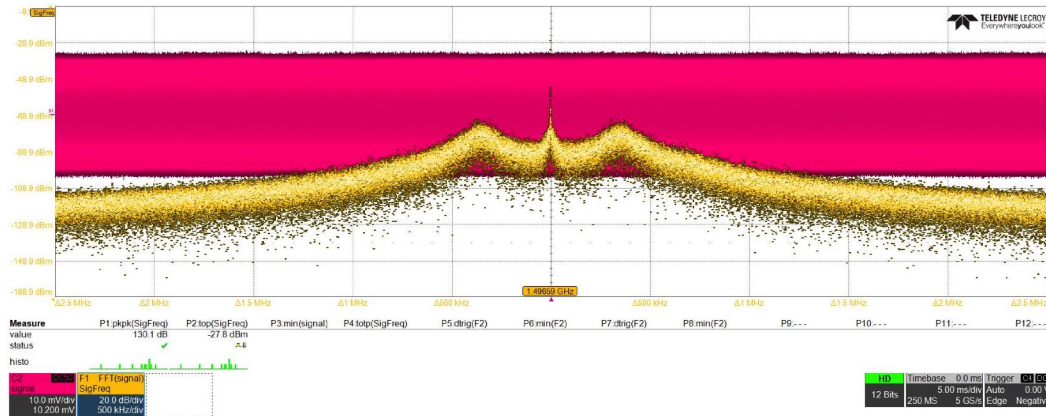
Figure 3.14: The beatnote signal on FFT oscilloscope at 1.4966 GHz. X-axis is frequency and Y-axis is amplitude [dBm].

In order to increase the frequency resolution of the FFT oscilloscope. For this device, the capture time t_{cap} = 500 ms. This yields a frequency resolution Δf = 2 Hz. The Nyquist frequency is f_{Ny} = 50 MHz. Hence, a higher frequency resolution can be achieved but with a maximum beat frequency of 50 MHz. The beat frequency can be decreased by exploiting the sidebands generated from the rf-source. Both lasers are locked on the rf-sidebands. Hence, the beat note frequency of Rydberg and master laser is determined by the frequency difference of the rf-frequency. In particular, the beat note frequency is reduced to 35 MHz which is shown in Fig. 3.15. Additionally, the beat note signal in the linear scale is composed of several data points. The linewidth of the beat note can be derived from this data set using the Voigtian and Lorentzian fit functions. By applying the eq. 3.31, the linewidth reads

$$\Delta \nu_{\text{Voigt}} = 1 \, ^{+2}_{-0} \text{ Hz}$$

The uncertainty of beat note linewidth obtained from the fit parameters is only 0.5 Hz. However, A relatively large asymmetric error [+2,-0] Hz is given here since the resolution limit of the FFT oscilloscope 2 Hz is reached, and the reason for using asymmetric error here is the linewidth will always be greater than 0. This result indicates a high reduction of technical noise due to the PDH locking performance. Particularly, a sub 10 Hz linewidth of laser has been achieved, which is 0.01% of the original linewidth. Please note only the relative stability of the laser frequency is given here, and the absolute stability of the frequency will be given by the trapped atoms in 2D-MOT and science chambers which will be discussed in the last chapter.
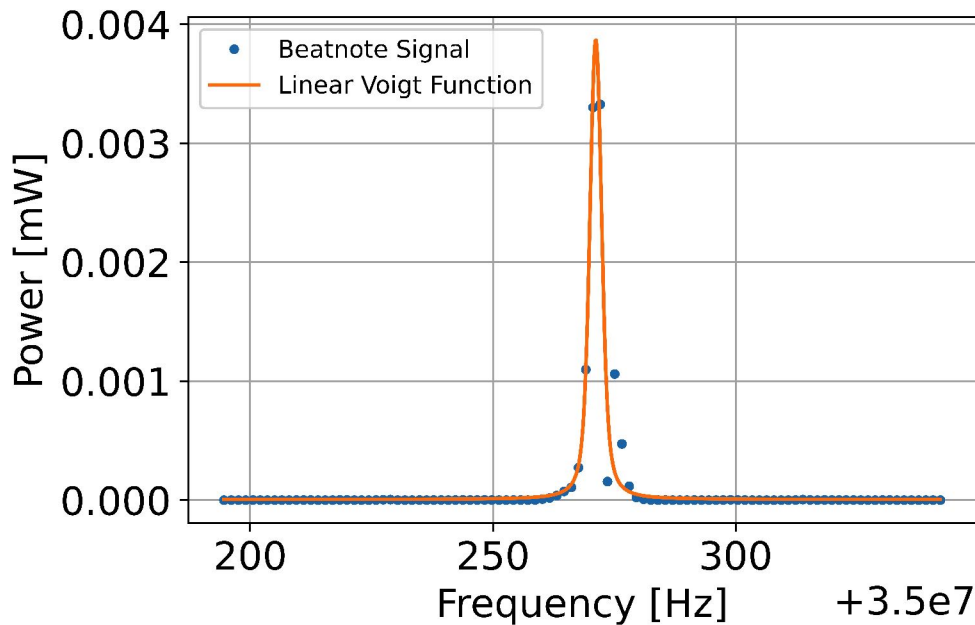
Figure 3.15: The beat note signal of PDH lock in linear scale with a Voigtian function is plotted.

Measurement of the Long-time Stability

In order to quantify the longterm stability of the cavity lock, the beat note signal is measured over a time scale of 3500 seconds. The frequency and amplitude drifts are shown in Fig. 3.16. The first beat note frequency and amplitude are used as a reference point, and so the frequency and amplitude deviations are zero at time t = 0 s. The frequency drift is within 15 Hz, and the amplitude fluctuates around 5 dBm. These drifts are mainly caused by residual amplitude modulation (RAM), which has been introduced in section 3.1.3. In conclusion, the stability of laser PDH locking fulfills our frequency stability requirements for further work.

3.4 Digital Offset Phase Lock

The digital phase lock is a technique for comparing the beat frequency of a frequency offset lock to the beat frequency of a steady radio frequency oscillator. With the digital offset phase lock, we do not need a reference cavity for each single laser, as we can lock the slave lasers up to several GHz away from the Master laser.

3.4.1 Setup of the Digital Phase Lock

As shown in Fig. 3.17, the light from Blue MOT laser and DL pro 1/2 lasers were overlapped on three different fast AC coupled photodiodes[10]. On each photodiode, the light from two lasers is

---

[10] Hamamatsu Photonics G4176-03

(a) Long term frequency drift

(b) Long term Amplitude drift
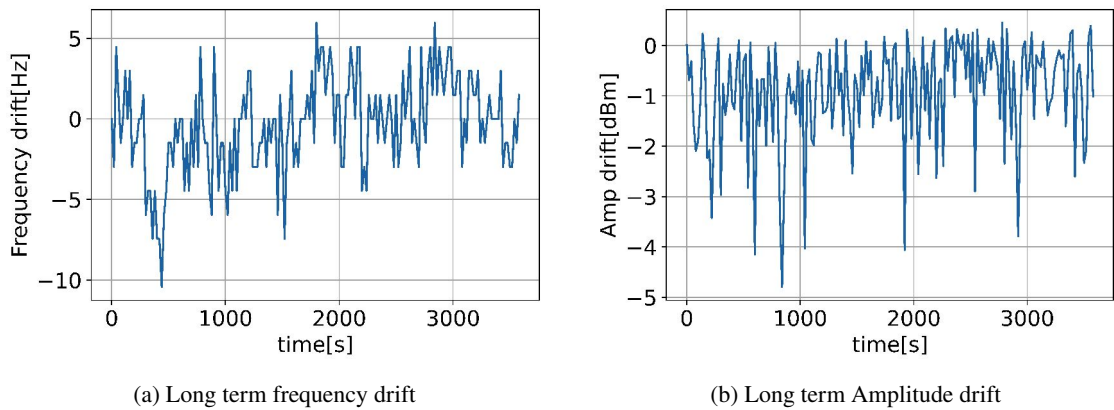
Figure 3.16: Longterm behavior of the beat note signal. (a) An oscillatory drift of the beat frequency is observable. (b) The ampitude drift is observed.

superimposed, so the beat note signal can be measured. Usually, we use a beat-frequency in the range of 1 to 2 GHz. The self-built fast AC coupled photodiodes can measure frequencies up to 6 GHz. Following that, the beat frequency is compared to a reference frequency from a steady RF-oscillator. We employ a direct-digital-synthesizer board (DDS-board) with a frequency tuning range of 20 MHz to 240 MHz as the RF oscillator[11]. One signal from the beatnote photodiode and one from the DDS-board are sent to a digital phase lock board. This board compares the two frequencies and generates an error signal as a result.

3.4.2 Principle of the Digital Phase Lock

To implement digital phase lock, a digital phase lock board is needed, which is also shown in Fig. 3.17. The critical component of the digital phase lock board is the Analog Devices AD4007 chip, which implements a digital phase-locked loop (PLL). The most common application for this board is to phase lock a microwave source to a radio frequency reference. In our scenario, we substitute a beatnote signal between two lasers operating in the 1 GHz region for the microwave source.

The counters transform the input signals from analog sine waves into digital pulse trains first. By default, the frequency of the reference signal is split by 2, whereas the frequency of the beatnote is divided by N (=8,16,32,or 64). The phase/frequency detector receives these digital pulse sequences. This is a completely digital circuit composed of several flip-flop gates that are opened and closed by the digital pulse sequence edges. These flip-flops regulate the state of the charge-pump. This component is comprised of two MOSFETs configured in a "push/pull" configuration. This implies that when one of the MOSFETS is open, it "pushes" charges out of the PIN 20 of chip, and the other "pulls" charges in from the outside. To measure this charge pumping, we connect the resistor and capacitor to PIN 20 and ground as shwon in Fig. 3.19. The voltage across these two components varies according to the amount of charge pushed/pulled per time unit. This is the error signal. One critical characteristic is that charge is pumped/pulled even when two signals are exactly the same frequency but out of phase. The two signals' digital edges are slightly out of phase, resulting in a difference in the amount of charge pushed and pulled. This increases the phase sensitivity of the
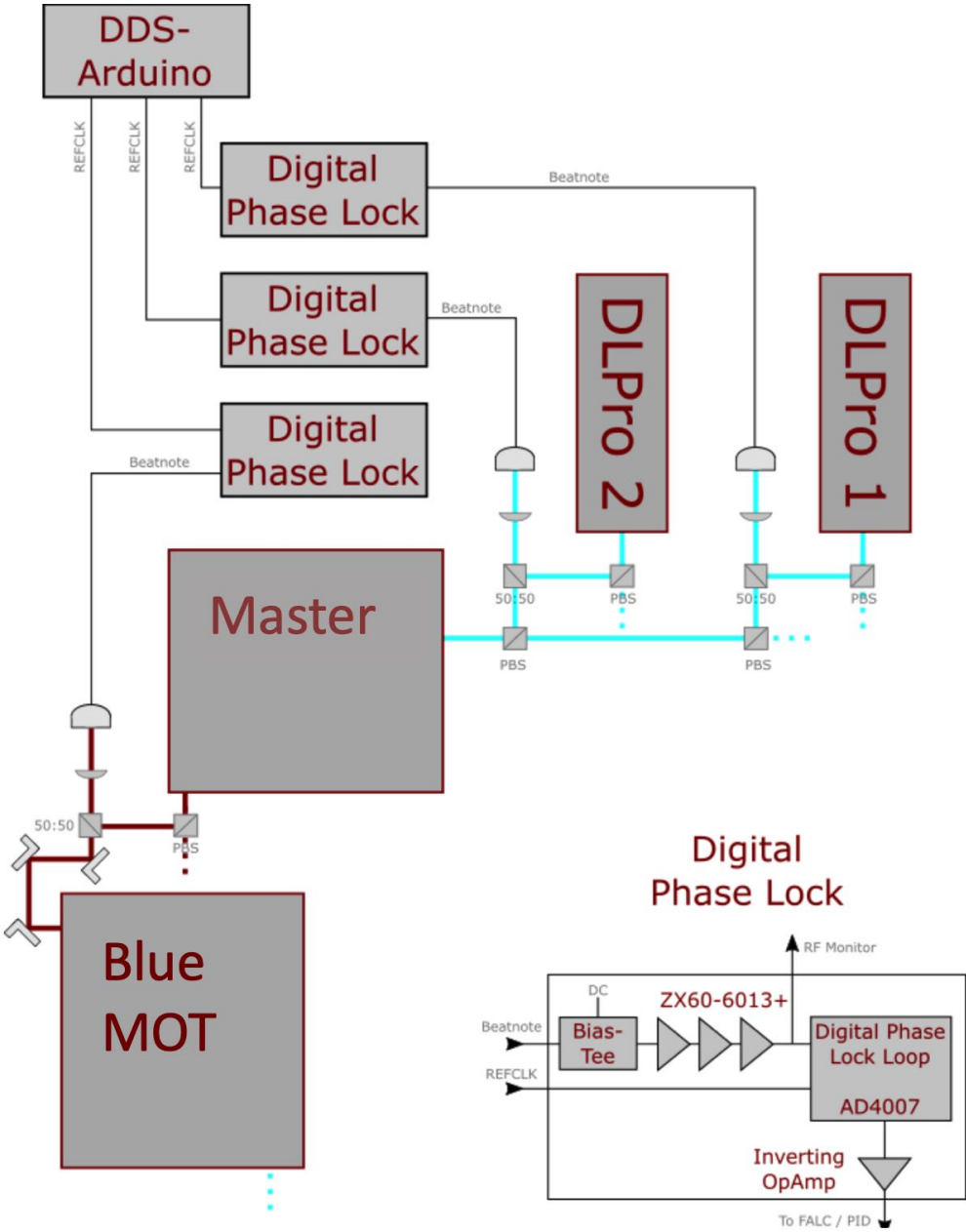
---

[11] DDS-ardunio

Figure 3.17: Setup of the digital phase lock. The light from the three lasers were overlapped on three different fast AC coupled photodiodes. Following that, the beat frequency is compared to a reference frequency from direct-digital-synthesizer board (DDS-board) in the digital phase lock board. Then, a error signal will be given by this board.

detector. The second critical point is that the error has already been integrated owing to the capacitor in the output. The charge pump increases (or reduces) the charge on the capacitor per time unit for a set phase/frequency difference. This implies that even with the smallest error, the error signal will always reach the maximum/minimum voltage, which is the typical behavior of an integrator in an open loop. This modifies the circuit's closed-loop function. This is now a double integrator when combined with the integrator in the PID-controller. Actually, we use FALC 110 as a PID-controller. Since the FALC actually already has multiple integrators, things become even more complicated. The critical point is that none of this matters for our purposes. The (dual, triple,...) integrator has an effect on the low frequency region of the lock, which we are already working with a very high gain. The high frequency part narrows the linewidth while the integrator is not used and the feedback is regulated by the proportional and differential parts. Another way to look at this is that the closed loop corrects any errors far in advance of the railing. Alternatively, over timeframes far shorter than the capacitor's time constant, the error signal is simply proportional to the instantaneous error.
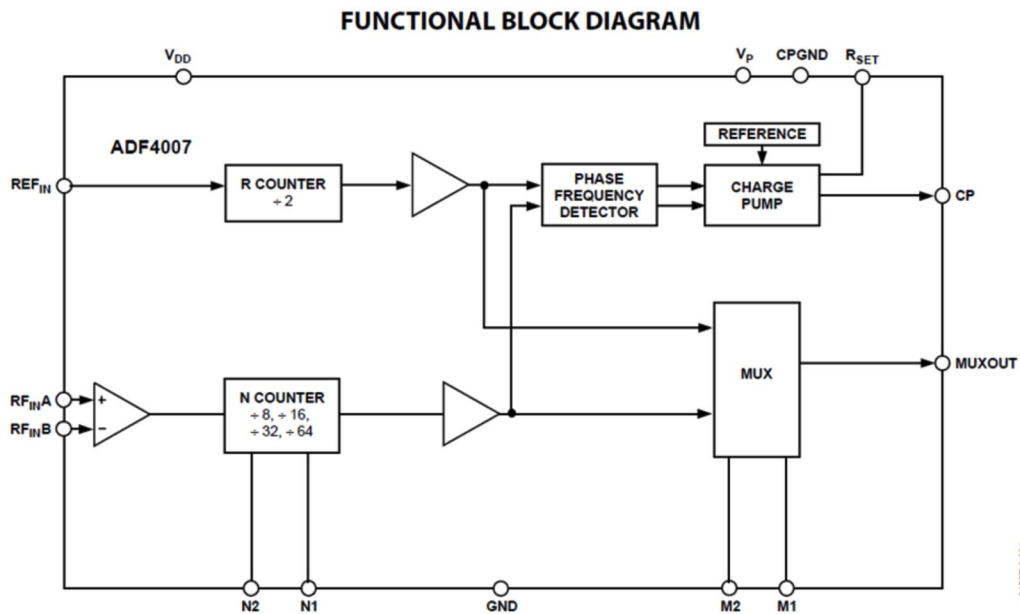
Figure 3.18: AD4007 chip from Analog Devices.[from ANALOG DEVICES] The AD4007 are 18-bit successive approximation register (SAR) analog-to-digital converters (ADCs) that operate from a single power supply, VDD. The reference voltage, VREF, is applied externally and can be set independent of the supply voltage.

3.4.3 Characterization of the digital phase lock

The beat frequency of the DLpro 1 and the Master laser was measured in Fig. 3.20. The beat frequency is at 1.6 GHz. In order to measure this beat note on FFT oscilloscope, one should apply a capture time t_{cap} = 50 ms. This yields a frequency resolution Δf = 20 Hz. The linewidth reads

$$\Delta v_{Voigt} = 24 \, ^{+20}_{-0} \text{ Hz}$$

The uncertainty of the beat note linewidth obtained from the fit parameters is 5 Hz. A larger
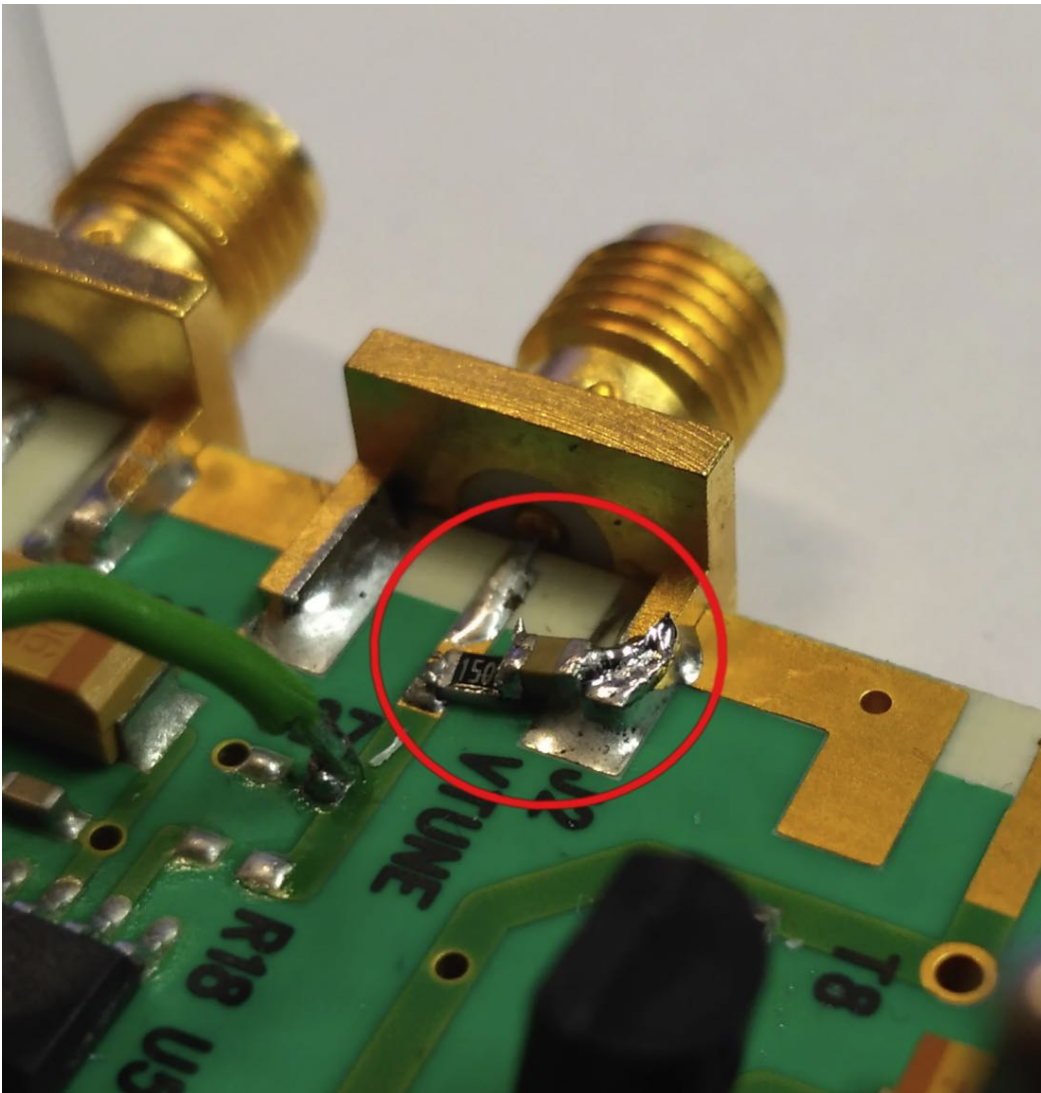
Figure 3.19: The capacitor between PIN 20 and ground.

asymmetric error [+20,-0] Hz is estimated because the resolution limit of the FFT oscilloscope is 20 Hz in this case. One may argue that compared with the beat note linewidth of the PDH lock we get in section 3.3, the linewidth of the digital phase lock is relatively larger. This is due to the fact that the locking electronics system is not perfect, and it has a certain response time. In particular, the response time is mainly determined by the parameters of the PID-controller and the charging time of the capacitors in our phase lock box. However, it is worth noting that such digital phase lock performance fulfills the next step of our experiment.
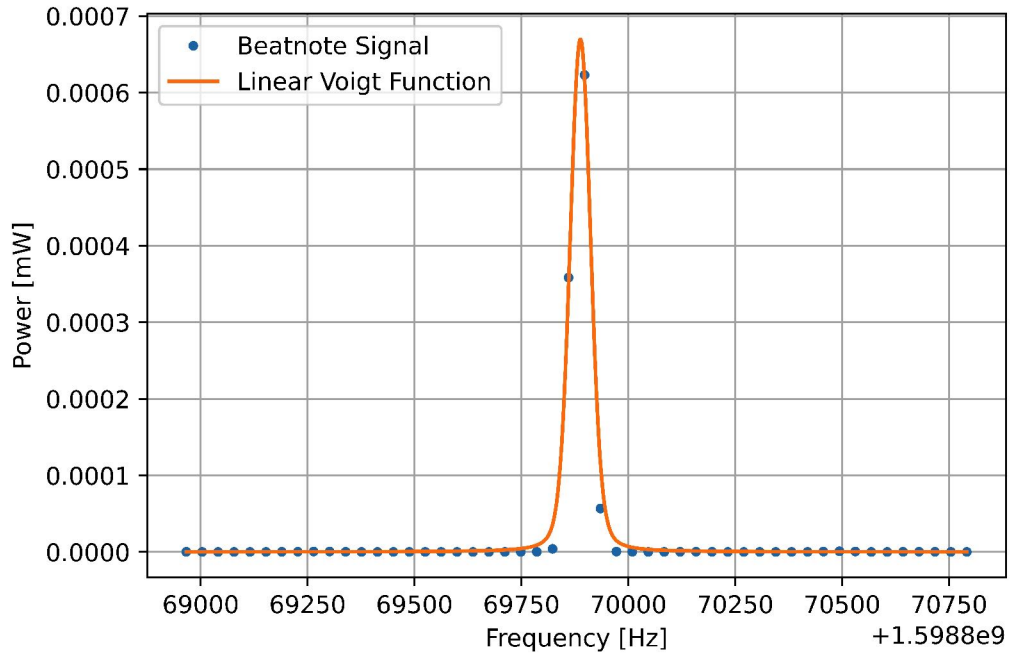
Figure 3.20: The beat note signal of digital phase lock in linear scale with a Voigtian function is plotted.

Probe/Control Pulse Shaping

To implement Rydberg EIT, a frequency stabilized weak probe beam at the wavelength 399 nm, and a strong, counter-propagating frequency stabilized control beam at the wavelength 395 nm are needed. Besides this, we also need to control the shape of the probe and control pulses.

Shaped probe/control pulses are commonly used for Rydberg EIT [52–54]. The use of shaped pulses can improve the fidelity of a Rydberg-blockade two-qubit entangling gate by several orders of magnitude compared to square pulses [55]. The frequency domain profile of a probe/control pulse is the Fourier transform of the time dependent pulse shape and determines the width, uniformity, and phase of the frequency spectrum. Due to the reciprocal relationship between time and frequency, short probe pulses have a very broad frequency distribution while long probe pulses have a very narrow frequency distribution. In addition to the duration of the pulse, the shape of the pulse also has an important effect on the frequency spectrum. For a given pulse duration, a Gaussian pulse has a narrower frequency domain linewidth than a boxcar pulse as presented in Fig. 4.1 and 4.2. As we already discussed in the previous chapter, Rydberg states typically have relatively narrow linewidths of the order of sub kHz level. If one considers using pulses with boxcar shape for Rydberg EIT, one needs to increase the pulse duration to achieve a narrower linewidth. However, a limiting factor for the pulse duration is the time the atoms stay in the center of the science chamber after switching off the MOT and the optical dipole trap. A more feasible and efficient approach is to use an optimal pulse shape with the shortest possible duration in the time domain and the narrowest possible linewidth in the frequency domain. Here, a Gaussian pulse shape is well suited for the probe pulse. Moreover, with probe/control pulse shaping techniques, one can also dynamically change the optical response of the EIT medium, for example, to implement photon storage.

4.1 Setup for Implementing Pulse Shaping

The setup for implementing pulse shaping is shown in Fig. 4.3. On the YQO Control computer, a specific function of a pulse can be predefined from the main experiment GUI in the variable window. Following that, these predefined values are sent into the database on the YQO Vault computer. Next, the fungen_server.py is launched on the YQO Device computer to set a network communication thread. It keeps on listening for the the YQO control pings and reads parameters from the database of the YQO Vault computer, and then it loads parameters to Arbitrary Function Generator (AWG).
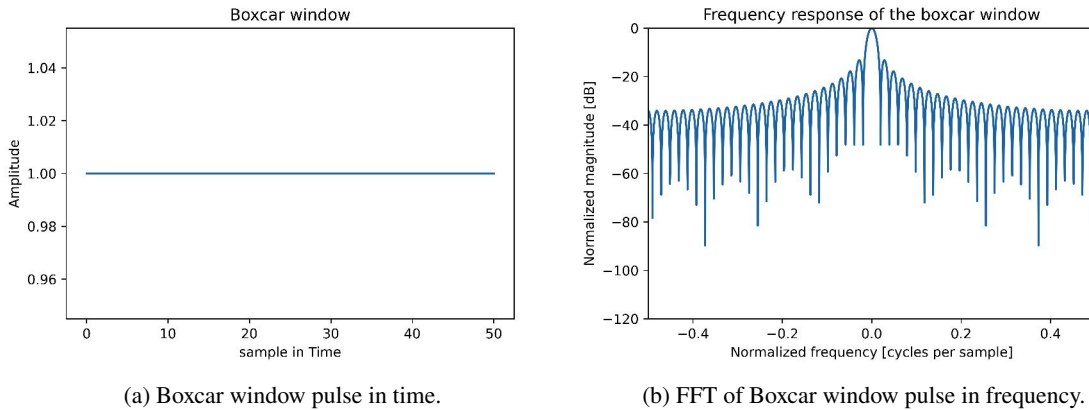
(a) Boxcar window pulse in time.

(b) FFT of Boxcar window pulse in frequency.

Figure 4.1: (a) shows a Boxcar pulse in time domain. (b) shows Fourier transform of the Boxcar pulse.

(a) Gaussian window pulse in time.
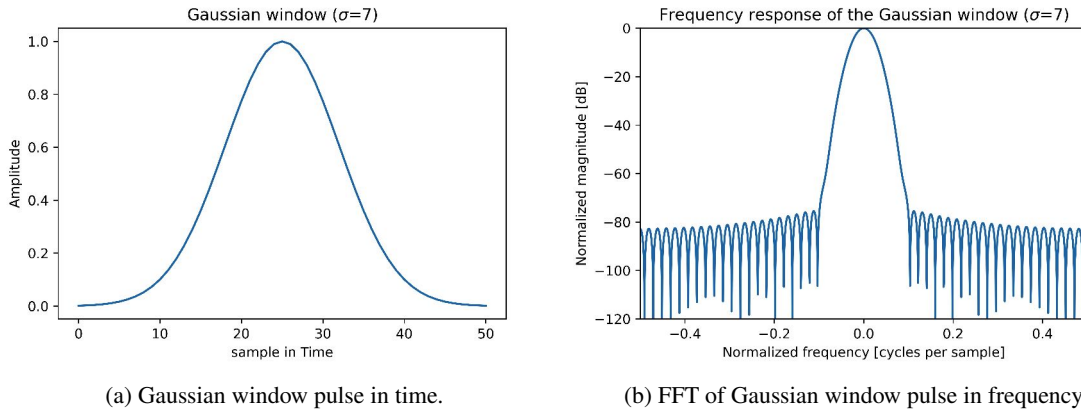
(b) FFT of Gaussian window pulse in frequency.

Figure 4.2: (a) shows a Gaussian pulse in time domain. (b) shows Fourier transform of the Gaussian pulse.

The AWG[1] is implemented for the generation of specially shaped pulse profiles in order to shape the control and probe beam, and the functions for specific pulse shape are stored in pulse_shapes.py file. These functions are called in the fungen.py script. Upon detection of an external trigger, the AWG output the pulses. The output signal from the AWG is fed into the analog input of the AOM driver box. The AOM driver box modulates the output of AWG using a mixer inside. Then, the output of AOM driver Box is fed into the Acousto-Optic Modulator (AOM[2]). The output pulse from the AOM is measured by a fast photodiode[3] and the signal is recorded by an oscilloscope. AOM nonlinearity is also dealt with by adding a calibration model in the auto_calibriation.py. This can be obtained by measuring the output optical power vs. control voltage.

---

[1] Agilent AWG 33522B

[2] Gooch and Housego 3200-129

[3] Hamamatsu Photonics G4176-03
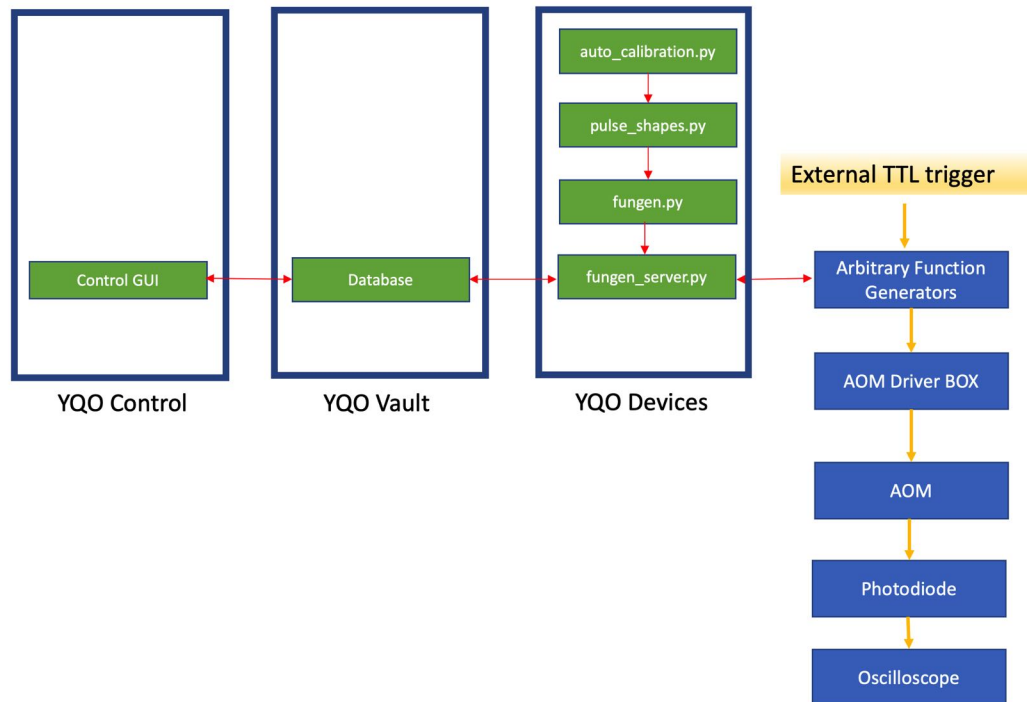
Figure 4.3: The setup for pulse shaping. YQO Control computer transmits predefined values for a specific function of pulse to the database on the YQO Vault computer. The fungen_server.py is used to load parameters from the database to Arbitrary Function Generator (AWG). Upon detection of an external trigger, the calibrated pulse of AWG is fed the analog input of the AOM driver box. The AOM driver box modulates the output of AWG using a mixer inside. Then, the output of the AOM driver Box is fed into the Acousto-Optic Modulator (AOM). The output pulse from the AOM is measured by a fast photodiode and, the signal is recorded by an oscilloscope. In addition, the functions for specific pulse shape are stored in pulse_shapes.py file. These functions are called in the fungen.py script.

4.2 Characterization of Acousto-Optic Modulator

An AOM, also called a Bragg cell, uses the acousto-optic effect to diffract and shift the frequency of light using sound waves. The working principle of AOM is illustrated in Fig. 4.4. A piezoelectric transducer is attached to a medium. A vibrating transducer is driven by an oscillating electric signal, which generates sound waves in the material. These can be regarded as a shift in periodic expansion and compression planes that change the index of refraction. An optical beam can be diffracted, typically into several orders and, the diffraction angle depends on the periodicity of the sound wave, e.g., it depends on the frequency of your RF signal. For the AOM driver, we use a DDS to generate these frequencies. That is to say, shaping the RF signal leads to shaping the optical pulse. Also, modulation can be carried out quite rapidly, so AOM is well suited for shaping the intensity profile of a laser beam.
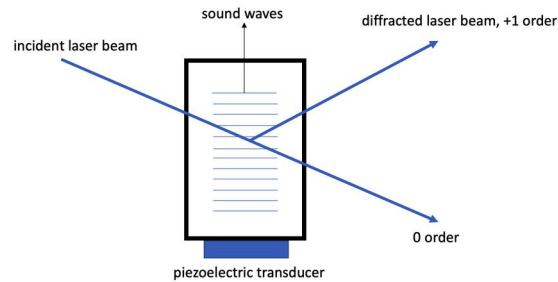
Figure 4.4: An acousto-optic modulator consists of a piezoelectric transducer which creates sound waves in a material. A light beam is diffracted into several orders. By modulating the material with a pure sinusoid and tilting the AOM, so the light is reflected from the flat sound waves into the first diffraction order.

4.2.1 Rise/Fall-Time

The rise/fall-time is critical for our application, since we need fast switching. It describes the switching time for the AOM transmission from 10% maximum intensity in the first order to the 90% maximum intensity, and vice versa. This will put a limit on how narrow we can make the pulse shape of our probe/control beam. Rise/Fall-time is limited by the finite velocity of sound in the acousto-optic medium. This can be explained by using Fig. 4.5, the acoustic wave will take some time to go through the beam diameter at the focal point. This implies that the response of an AOM with a large incoming beam diameter is necessarily slow. While such a modulator can be operated with a focused laser beam of smaller diameter, the diffraction efficiency may suffer as a result of the increased beam divergence. In addition, it is necessary to keep the AOM at the geometric center of the two focal lenses because this will make the transmitted light with different orders collimated.

The setup for measuring the characteristic curve of AOM[4] is shown in Fig. 4.6. First, the AOM Drive Box fast switches on and off the AOM with an external TTL trigger. Then, the light from the AOM is coupled into a single mode fiber of probe laser. A APC/PC single mode fiber is used to couple the light into the single photon counter. Here, the APC is connected with single mode fiber of probe laser with Mating Sleeves and, the PC is connected to the single photon counter (SPC)[5]. The typical time resolution of SPC is 1000 ps. Following that, the output signal from the single photon counter is transmitted to the Time tagger[6]. Time tagger is an 8-channel digital counting device used to register photon counter clicks (e.g., single photon count events from SPC) with a time resolution of 60 ps, and it is also need to have an external TTL trigger. The data acquisition is done on the Time tagger software of the computer. The measured characteristic curve of DLpro 1/2 AOMs are shown in Fig. 4.7. The rise time of DLpro 1 laser AOM is 7 ± 1 ns, and for DLpro 2 laser AOM it is 8 ± 1 ns, which means these AOMs are definitely good for implementing pulse shaping at the scale of microseconds.

---

[4] Gooch and Housego 3200-129

[5] COUNT-100B-FC from LASER COMPONENTS
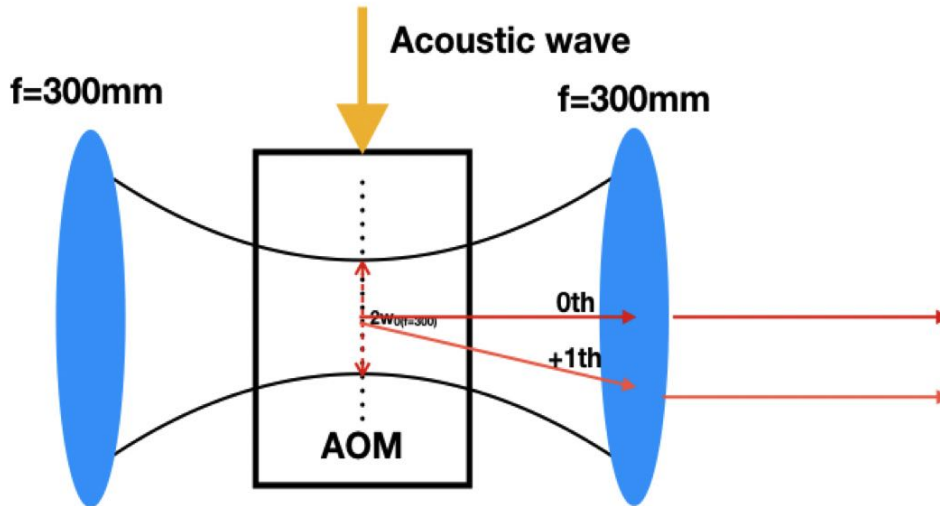
[6] Swabian Instruments Time-tagger 20

Figure 4.5: Diagram of light and acoustic wave interaction in AOM. An acoustic wave will take some time to go through the beam diameter at the focal point, and the rise/Fall-time is limited by the finite velocity of sound in the acousto-optic medium.
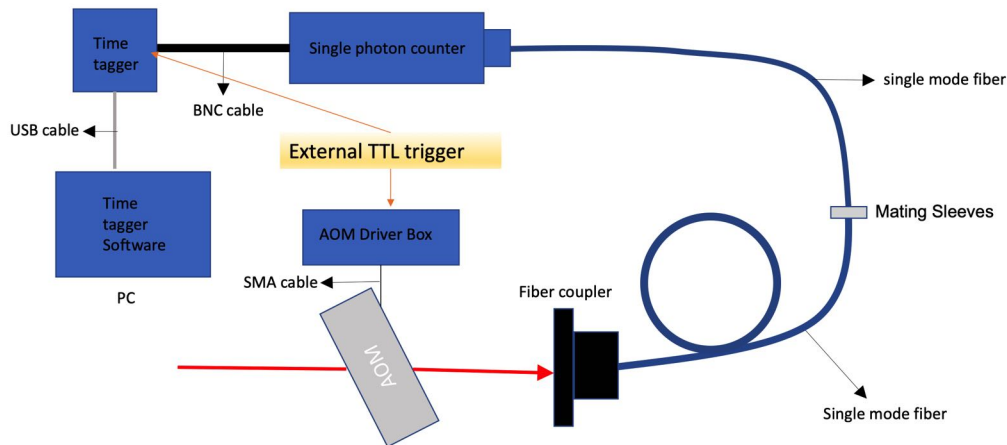

Figure 4.6: The setup for measuring the characteristic curve of AOM. The AOM is drived by the AOM Drive Box with an external TTL trigger. Then, the light from the AOM is coupled into a single mode fiber of probe laser. A APC/PC single mode fiber is used to couple the light into the single photon counter. After that, the output signal from the single photon counter is transmitted to the Time tagger. The Time tagger also have an external TTL trigger. Finally, the data acquisition is done on the Time tagger software of the computer.
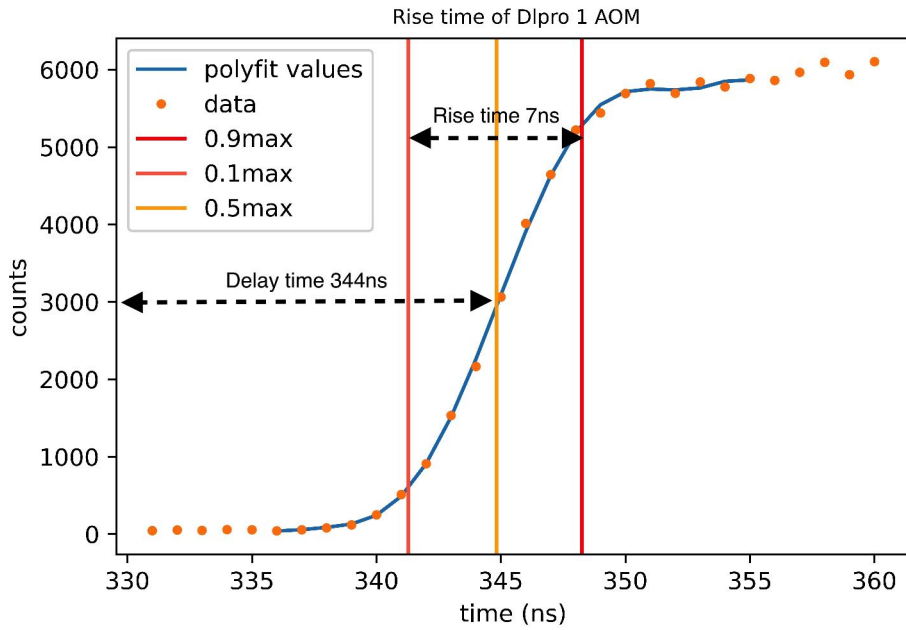
(a) Characteristic curve of DLpro 1 laser AOM. The rise time is 7 ± 1 ns.
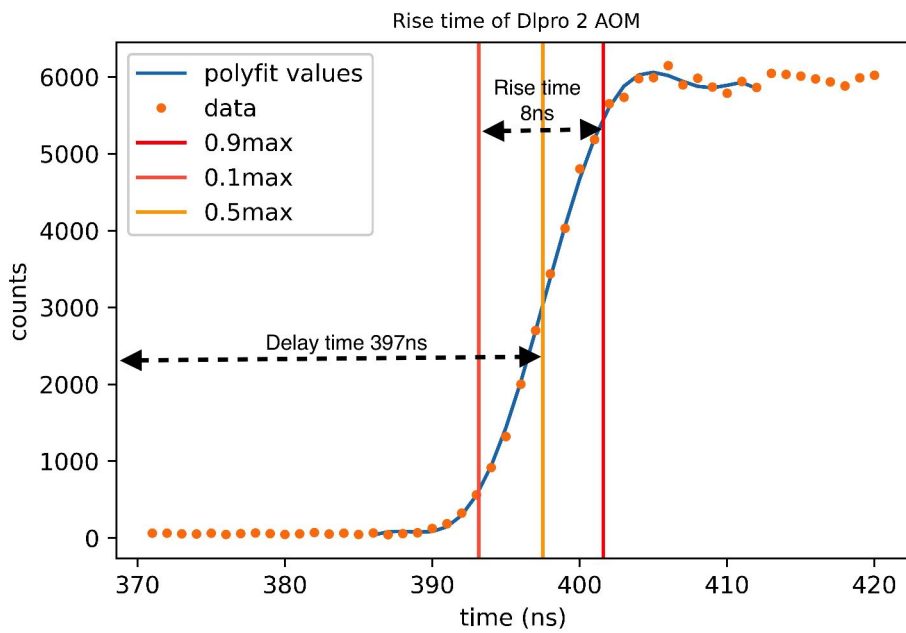
(b) Characteristic curve of DLpro 2 laser AOM. The rise time is 8 ± 1 ns.

Figure 4.7: (a) shows characteristic curve of Dlpro 1 laser AOM, (b) shows characteristic curve of Dlpro 2 laser AOM. The rise time is given in these figures.

4.3 AOM Calibration

The nonlinearity of an AOM can be observed on an oscilloscope in Fig. 4.8. A voltage ramp of 0-10V (blue trace) is applied to the analog input of the AOM driver box, the pulse shape of the output signal (green trace) is not the same as the input. Since the Rydberg EIT is highly sensitive to probe/control pulse shape, it is necessary to calibrate the AOM.
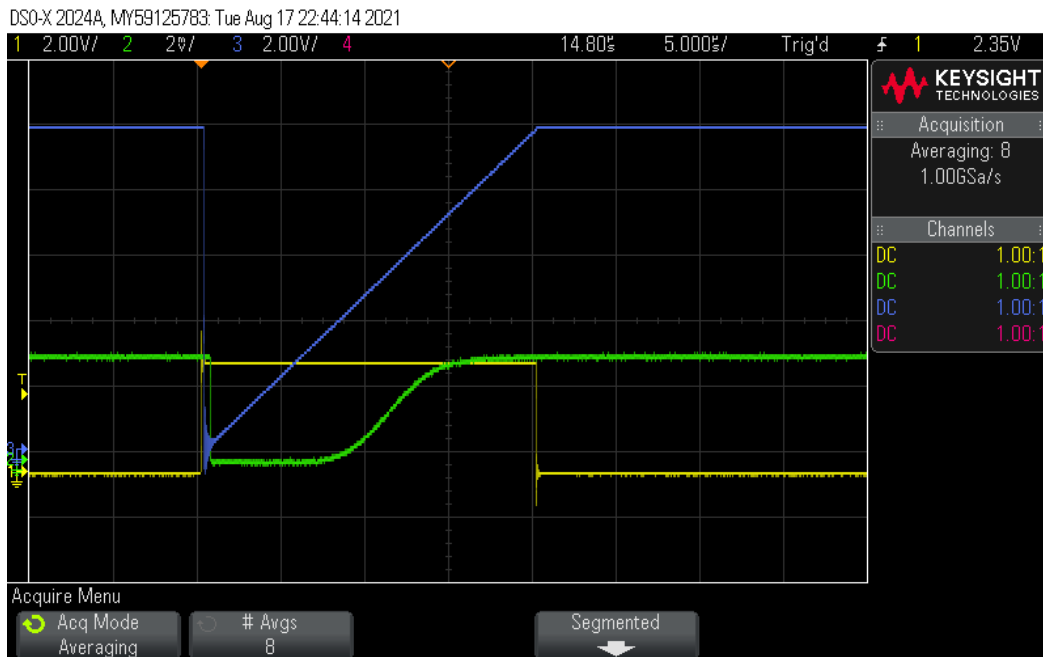
Figure 4.8: The input and output signal of AOM. The blue curve is the voltage from the Function Generator, and the yellow trace is the external TTL trigger (to the Arbitrary Function Generators), the green trace is the power of the light measured on a photodiode. X-axis is time, and Y-axis is voltage.

The calibration of the output laser power is done by recording a trace for a range of voltage applied to the AOM amplitude input. The trace is chopped for a suitable range, and a polynomial model is fitted as shown in Fig. 4.9 to generate calibration parameters. The calibrated fitting parameters need to be stored in the fungen.py script for the poly1d models. To make the process more convenient and efficient, I created a script. Every time one needs the Arbitrary Function Generator to drive different AOMs, this calibration process can be automatically done by running the auto_calibration.py script.

4.4 High Fidelity Gaussian Pulse Output

An idea Gaussian pulse is defined from the main experiment GUI in the variable window on the YQO Control computer. Without any calibration, the idea Gaussian pulse was sent to the AOM Driver Box. Then, the output pulse from the AOM was measured. As shown in Fig. 4.10, with an idea Gaussian pulse into the AOM Drive Box, the output pulse from the AOM is definitely not a Gaussian pulse. Also, very large distortion can be observed.

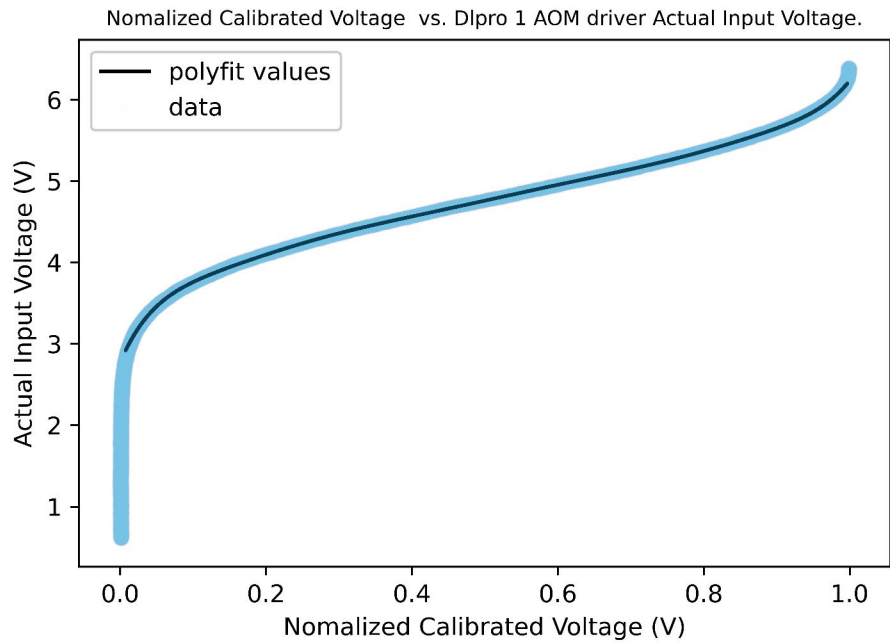To avoid the large distortion of the output pulse of AOM, the calibration process needs to be applied.

Figure 4.9: The calibration curve of DLpro 1 laser AOM. The black curve gives a Polynomial fitting function to calibrate the AOM.
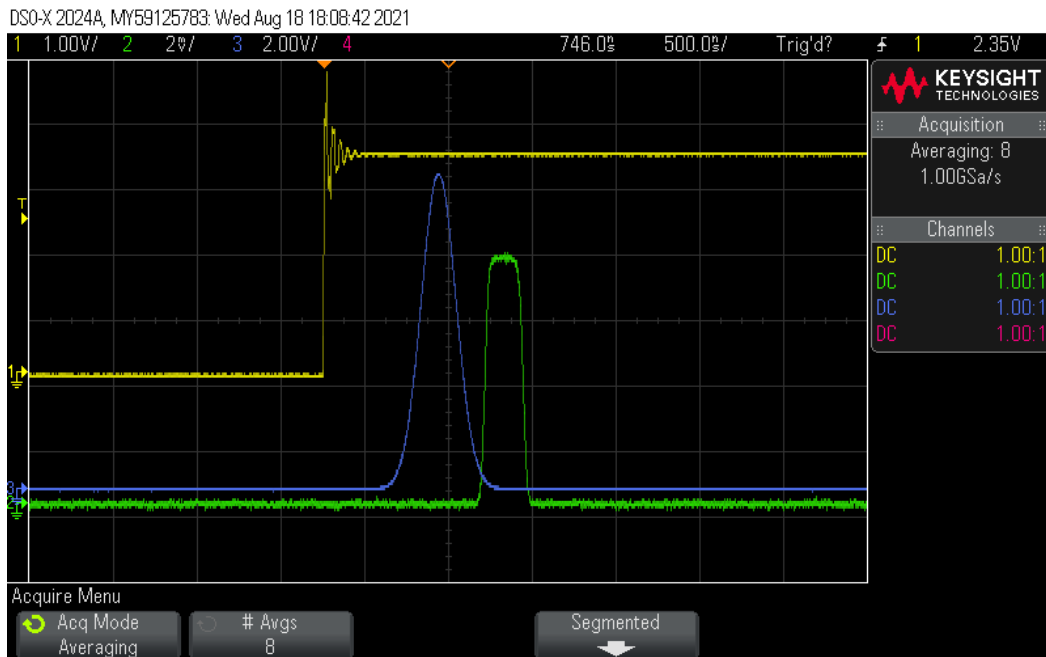

Figure 4.10: The input and output signal of AOM. The blue curve is the idea Gaussian pulse from the Function Generator, and the yellow trace is the external TTL trigger (to the Arbitrary Function Generators), the green trace is the output pulse of AOM measured on a photodiode. X-axis is time, and Y-axis is voltage.

We need to quantitatively study the fidelity of our pulse shaping with the calibration, so an idea Gaussian pulse is defined on experiment GUI. After the calibration, the modified pulse was sent to the AOM Driver Box. Then, the output pulse from the AOM was measured. In Fig. 4.11, the fitting parameter sigma of normalized applied input pulse (green curve) is $1.0265 \cdot 10^{-7}$ and $1.02155 \cdot 10^{-7}$ of fitted normalized output pulse (orange curve) from the AOM. It is clear to verify that less than 1% distortion can be observed between the applied signal and the output signal from AOM. Also, the calibrated signal is very fast on the order of microseconds.
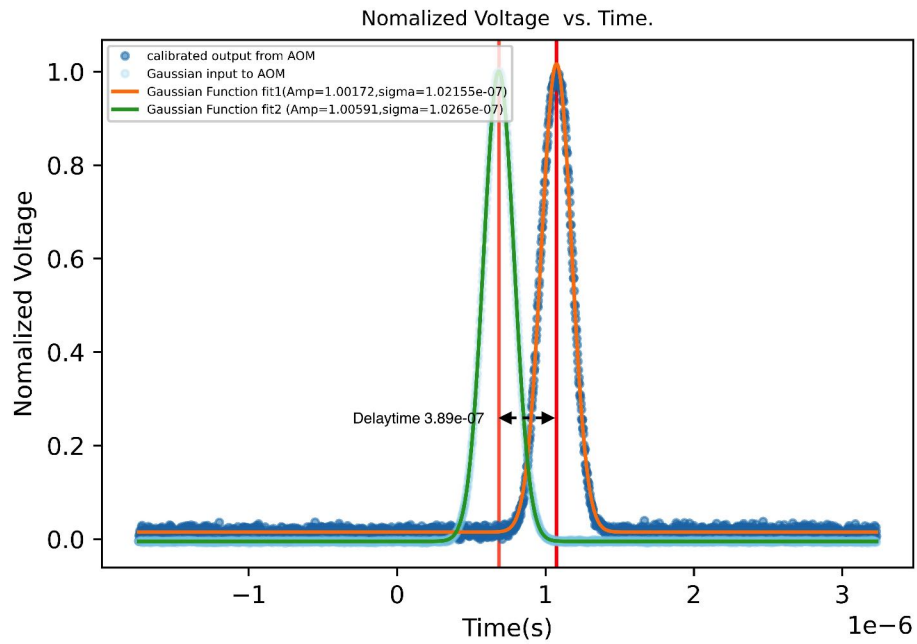
Figure 4.11: The calibration of Gaussian pulse. The green curve is a fit of applied signal into Arbitrary Function Generators, the orange curve is a fit to the output signal measured on oscilloscope. Both the applied signal and output signal of AOM are normalised. By comparing the fitting parameters shown in this figure, less than 1% distortion of the output signal has been achieved.

The New Homemade Titanium Ultra-High Vacuum (UHV) Chamber

As we already discussed in chapter 2, ytterbium is pre-cooled in the 2D-MOT chamber. Initially, we used a glass cell from the company JapanCell to implement the 2D-MOT. But the glass cell has the problem that it is very fragile and easy to break when one aligns the 2D-MOT chamber to the science chamber on the experiment table. To fundamentally solve this problem, a better solution was proposed by one of our senior scientists Rafael Rothganger de Paiva. He designed a new titanium UHV chamber which is shown in Fig. 5.1. The basic idea is to find a metal frame which is glued by four viewports. To ensure UHV compatibility, the thermal expansion of the metal frame and the viewports should be matched. After careful serach, we found the titanium frame and the BK7 viewports fulfill the requirement. This new titanium UHV chamber is very robust and reliable. I assisted with assembling this new titanium UHV chamber, and the steps will be discussed in this chapter.
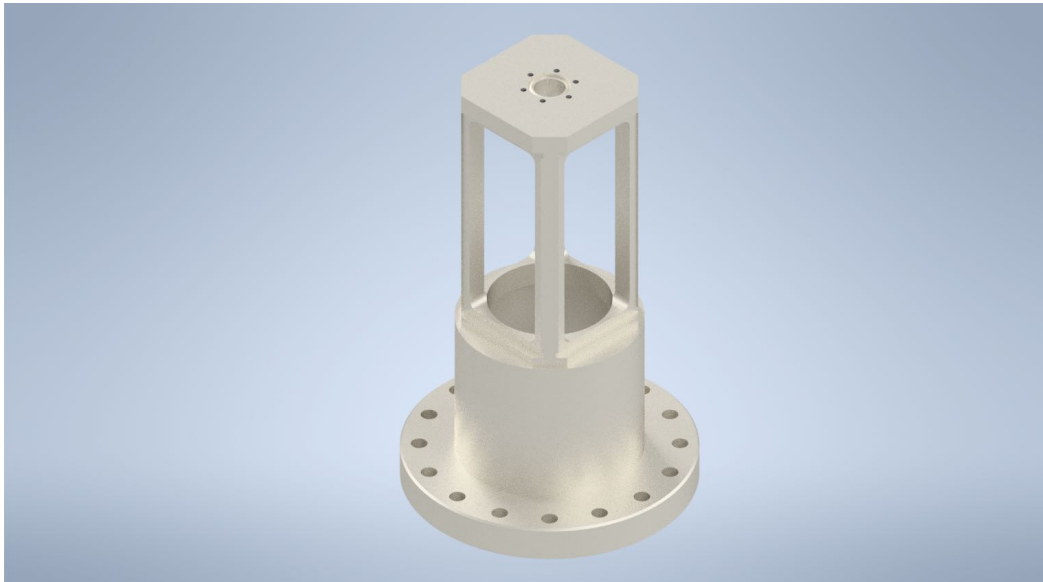

Figure 5.1: The 3D drawing for Titanium UHV chamber.

5.1 UHV cleaning for Titanium Frame

Cleaning the titanium frame for UHV operation is important, because even small patches of dirt can contaminate the chamber and one needs to evaporate it for a long time in the baking phase to reach the desired pressure. The fundamental goal of the cleaning process is to eliminate all organic matter, particularly any remnants of oil and grease. The cleaning procedure begins with a rough cleaning with a clean cloth and goes through solvents in an ultrasonic bath of several steps. Note that the cleaning should be done under a fume hood for safety purposes as well as to keep it clean.

1. **Soap Degreasing:** This step is to remove any grease and oil from the surface of the titanium frame. The titanium frame is immersed in an ultrasonic bath with Sonoswiss T1 in distilled water at 70°C for 1 hour. The Sonoswiss T1 is diluted 5% by volume.

2. **Soap Rinsing:** After cleaning the parts with soap, the following step is to remove any soap residue. This is accomplished by first rinsing the titanium frame in the distilled water then sonicating it in distilled water for 10 minutes.

3. **Solvent Cleaning in acetone:** The titanium frame was then immersed in an ultrasonic bath containing acetone with 99.8% purity for 1 hour. While acetone is effective in dissolving a wide variety of pollutants, this may leave a residue. It should be noted that if the same ultrasonic bath is used for both soap cleaning and solvents, it must be fully cooled in between processes, as acetone has a boiling point of 56 $^\circ$C.

4. **Solvent Cleaning in Isopropanol:** The titanium frame needs to be rinsed with Isopropyl Alcohol (IPA) with 99.8% purity immediately after leaving the acetone bath while still wet from the acetone. The reason for this is that if the acetone evaporates first, there is a risk that the dissolved contaminants will stick back to the surface. When the acetone has been rinsed of with IPA, the titanium frame is immersed in an ultrasonic bath with IPA for 30 minutes.

5. **Dry:** When the IPA bath has been done, the titanium frame should be clean but need to dry. It should be dried with pressurized nitrogen air flow under a fume hood. Then it is wrapped with vacuum grade aluminium foil.

Once the cleaning process is done following the steps above, the BK7 viewports are glued to the frame. The gluing process needs to be done in a clean space (ideally in a clean room). In the next section, the gluing process will be discussed in detail.

5.2 Gluing Viewports to Titanium Frame

The choice of glue is very important and should be fulfilled the following requirements: First of all, it should have small enough particles so that it doesn't contain air bubbles trapped inside. Secondly, it should be possible to cure at a temperature which will not destroy the coating on the viewports (the maximum tolerance temperature of viewports coating is 200 $^\circ$C). Also, it should have a proper cure condition. Here, we chose to use the Epotek H77S glue[1], since the particle of it is only 20 microns

---

[1] H77S glue from EPOXY TECHNONOGY

Color (before cure)	Part A: Grey; Part B: Amber
Consistency	Smooth pourable liquid
Glass Transition Temp	$\geq 80 \quad °C$
Coefficient of Thermal Expansion	Below Tg: 39×10^{-6}in/in°C; Above Tg: 98×10^{-6}in/in°C
Particle Size	≤ 20 microns

Table 5.1: Physical properties of Epotek H77S glue.

and the cure condition of it is 150 °C for 1 hour. The physical properties of the Epotek H77S glue are shown in Table. 5.1.

Once the glue is chosen, the gluing process should be carried out ideally in a cleanroom. Actually, we did glue in a fume-hood in a newly built lab.

1. The glass viewports must be cleaned with ethanol (99.8%) and optical cleaning tissues.

2. Prepare the Epotek H77S glue, using 100:35 weight ration of Part A and Part B (see Table. 5.1) in a 100 ml beaker.

3. Socinate the beaker to remove the air bubbles in the glue for 10 mins at 40 °C.

4. Insert the glue into a syringe with 21 gauge needle. Make sure that the needle is always dipped inside the solution so that no air bubbles can leak into the syringe.

5. Place the titanium frame horizontally and apply the glue along the grew of the titanium frame with the syringe. Care must be taken to apply uniform pressure on the piston of the syringe. Spread the glue uniformly across the contact surface with the needle such that no bubbles or empty spaces are left.

6. Place the viewports carefully such that no air bubbles are trapped in between the contact surfaces as shown in Fig. 5.2. If any bubbles are trapped, one could take the viewport away and restart the process from step 3.

7. Place the titanium Frame in the oven, and bake the chamber at 150 °C for 1h. To reach 150 °C, a ramp of 1 °C/min must be used in order to avoid any cracks in the BK7 viewports.

8. Ramp the oven down to room temperature.

9. Repeating the process starting from step 1, all the viewports are glued into the titanium frame. The complete titanium chamber is shown in Fig. 5.3.

10. Place the fully assembled chamber one more time in the oven for 24 hours at 180 °C.

5.3 Leak Proof of the Newly Built Titanium Ultra-High Vacuum (UHV) Chamber

Before connecting the titanium 2D-MOT chamber together with the science chamber, it is necessary to check if it is leak proof. The process we utilized for pumping down the titanium chamber is as follows.
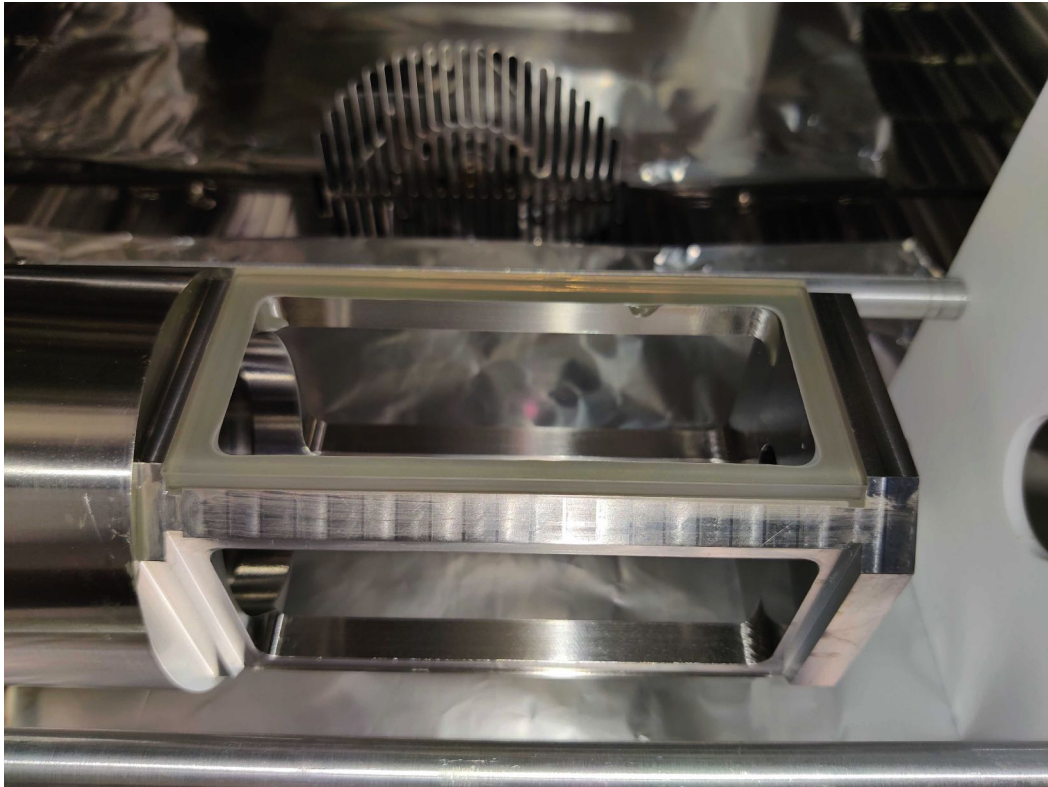
Figure 5.2: Glue the glass plate to the titanium Frame.

1. The titanium chamber was mounted on a stainless steel spherical octagon[2], and the nuts were tightened following a star pattern in order to make the connection leak proof. Also, the titanium 2D-MOT chamber was closed with a CF 16 blanking flange in order to test the titanium chamber independently. The assembled titanium chamber is shown in Fig. 5.4.

2. The vacuum process can be implemented. The turbo pump from Pfiefer vacuum was connected to the titanium chamber via the Gate valve[3]. Then a roughing pump was connected to the exhaust of the turbo pump. The basic idea is to utilize the roughing pump to lower the pressure enough for the turbo to turn on and then use the turbo as the main pump until the pressure is low enough for the getters to work.

3. Once everything was made sure to be tight and no leaks, started pumping with the roughing pump up until 10^{-3} mbar and then started the turbo pump.

4. After pumping for 4 hours, the pressure of the titanium 2D-MOT chamber reached 10^{-8} mbar.

5. Then, as it seems the 2D side was leak proof, we did activated the NGEs[4] and Ion pumps for further removing dust.

---

[2] Kimball Physics 6" spherical octagon
[3] All-metal angle valve, DN40, VAT
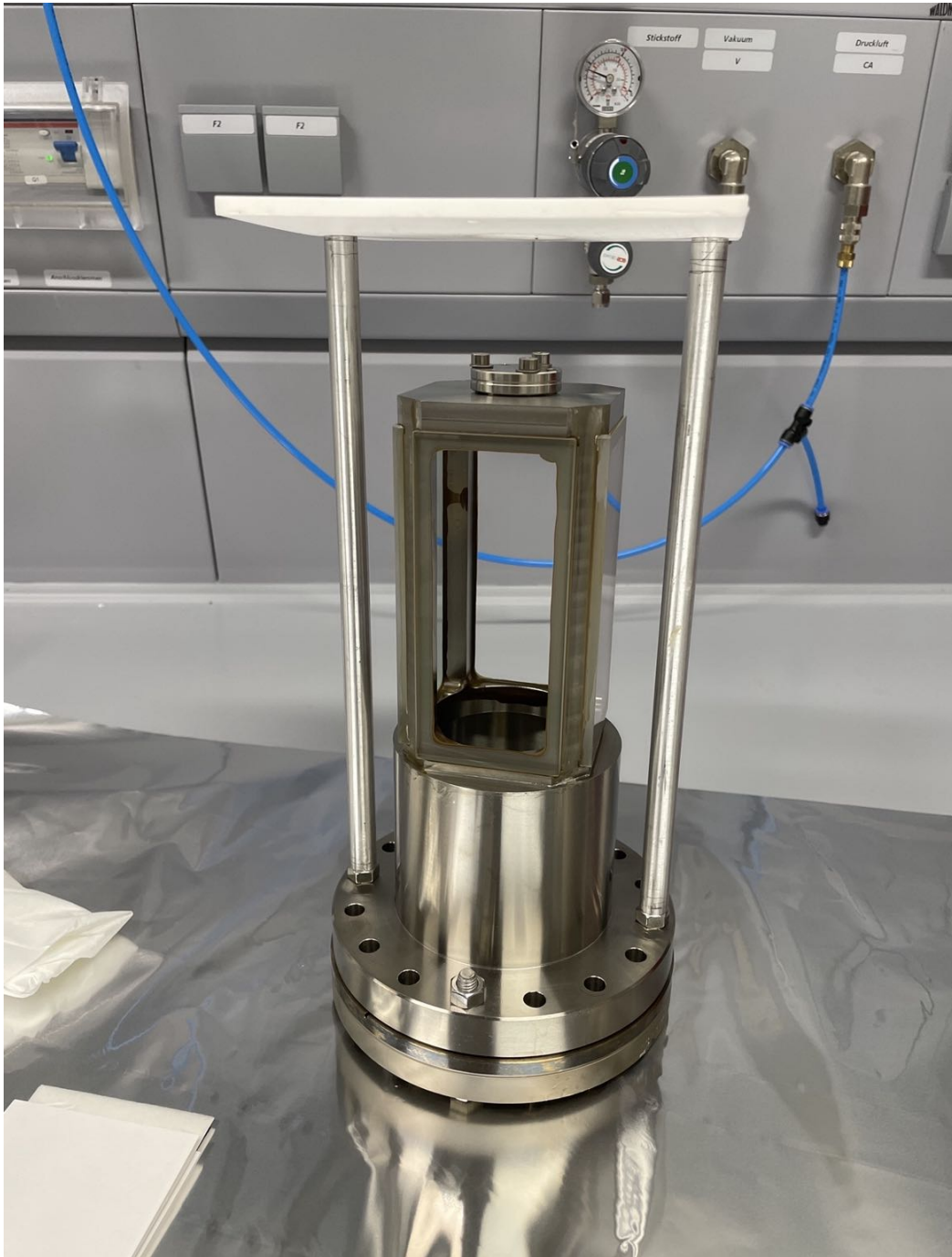[4] Saes group NEXTorr Z200

Figure 5.3: Titanium chamber with all glass plates glued.

Figure 5.4: Titanium 2D chamber mounted on a stainless steel spherical octagon.

6. By pumping down it for a weekend, the pressure of the titanium 2D-MOT chamber reached 10^{-10} mbar.

It was conclusive enough that the titanium chamber was leak proof and sufficient enough to connect to the science chamber. After connecting the titanium 2D-MOT chamber and the science chamber, the overall system also needs to be baked. The baking procedure is carefully discussed in Mogens Henrik From's thesis [56]. Since the baking process is not the focus of this chapter, only the final pressure after the baking is shown here: 2D-MOT chamber: $8.7 \cdot 10^{-11}$ mbar, science chamber: $8.9 \cdot 10^{-11}$ mbar. The high level of vacuum confirms that our homemade titanium chamber has a performance as good as the commercial company's product.

Experiment results of 2D/3D Magneto-optical trap (MOT)

With the realization of a stabilized laser system(see chapter 3) and a high-vacuum experimental chamber system (see chapter 5), we are in the position to implement a 2D and 3D-MOT.

The schematic optic setup of 2D/3D-MOT is shown in Fig. 6.1. Our design of a dispenser-loaded 2D-MOT follows the design of the Hamburg (Becker/Sengstock) Yb setup [14], one of the 1st-generation Yb experiments, and mixes in ideas from a by now very popular design for an alkali 2D-MOT originally from Amsterdam (Walraven) [57]. The experiment begins by loading ytterbium atoms from the dispensers. These atoms is pre-cooled into the 2D-MOT using the wide $\Gamma/2\pi = 29.1$ MHz singlet transition $^1S_0 \rightarrow {}^1P_1$. Not like the conventional 2D-MOT system, which costs lots of space and large optics for making a single elliptical cooling beam in a 2D-MOT chamber, we use 5 separate 2D MOTs. Five circular, consecutive cooling regions are chosen in the 2D-MOT chamber. Besides, we use dispensers which makes our setup less noisy compared to a thermal source like an oven with a Zeeman slower. The 2D-MOT serves as the source of cold atoms for subsequently loading into a 3D-MOT. Then, the 2D-MOT is transferred to the science chamber through a transfer stage with push beams. Finally, in the science chamber, a green MOT ($^1S_0 \rightarrow {}^3P_1$) traps and cools atoms in a central region while a blue "shell" MOT ($^1S_0 \rightarrow {}^1P_1$) provides an initial slowing of atoms coming from the 2D-MOT. It combines the low temperature of the triplet MOT with the high capture velocity of the singlet MOT. The last step is the optical trap (not implemented yet).

In this chapter, first of all, the 2D-MOTs of different isotopes of ytterbium will be discussed. Then, the picture of the first Blue MOT in the science chamber will be shown.

6.1 2D-MOT

In this section, the fluorescence of 2D-MOT and the measurements of ytterbium isotopes are briefly shown.

We locked the Master laser at 375.7622 THz, then manually scanned the 2D -MOT laser and measured the beatnote frequency with the spectrum analyzer. Since the dispenser is not a pure Yb 174 source, several MOTs of the different isotopes can be seen in the 2D-MOT chamber.

The 2D-MOT was observed by a camera, a typical fluorescence of MOT is shown in Fig 6.2. We can observe MOTs with beat frequency at −366 MHz (from Master laser lock, faint fluorescence), 0 MHz
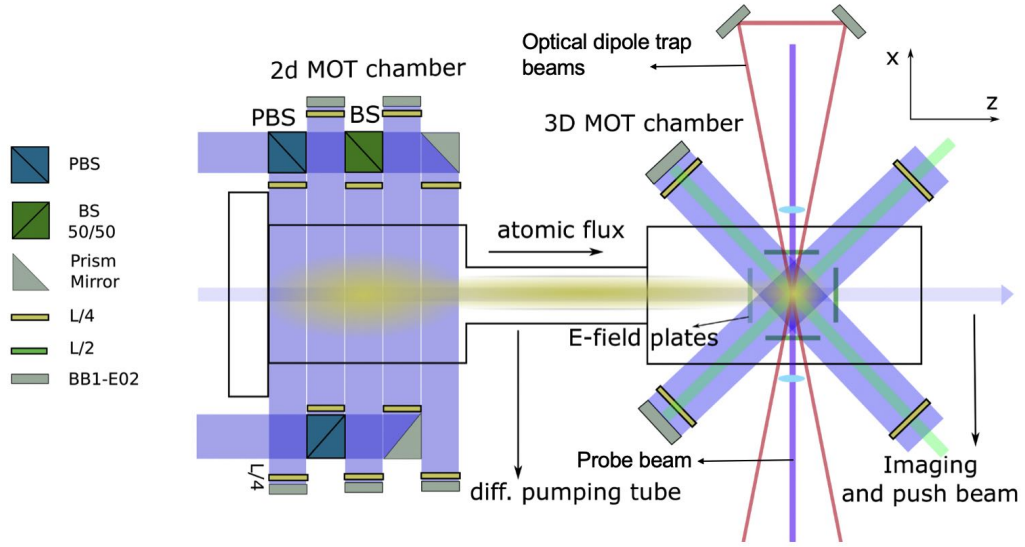
Figure 6.1: Schematic setup of the 2D and 3D-MOT optics. The experiment begins by loading ytterbium atoms from the dispensers. These atoms is pre-cooled into the 2D-MOT using the wide $\Gamma/2\pi = 29.1$ MHz singlet transition $^1S_0 \rightarrow {}^1P_1$. Five circular, consecutive cooling regions are chosen in the 2D-MOT chamber. Then, the 2D-MOT is transferred to the science chamber through a transfer stage with push beams. Finally, in the science chamber, a green MOT ($^1S_0 \rightarrow {}^3P_1$) traps and cools atoms in a central region while a blue "shell" MOT ($^1S_0 \rightarrow {}^1P_1$) provides an initial slowing of atoms coming from the 2D-MOT. The atoms are then put into a far red-detuned, crossed optical dipole trap, followed by further cooling approaches such as evaporative cooling. When the atoms have reached the final temperature, the Rydberg EIT experiments are performed. A single photon probe beam at a wavelength of 399 nm and a strong counterpropagating control beam at a wavelength of 395 nm are combined to couple the Yb atoms into the Rydberg state. Subsequently, the electric field control is used to ionize the Rydberg atoms. Then, the ions can be detected on a microchannel plate.

MOT	Measured MHz	Shift from the strongest MOT (4) MHz	value from ref[58] MHz.	Isotope
1	366	1202	1190.36	171 F = 1/2
2	0	836	835.19	171(F = 3/2)
3	-308	528	531.11	172
4	-836	0	0	174
5	-1332	−496	−508.89	176

Table 6.1: Isotope measurement of ytterbium.

(Both, 2D-MOT laser and Master laser the same frequency, and faint fluorescence), at −308 MHz (2nd strongest fluorescence), −836 MHz (the strongest fluorescence signal) and −1332 MHz (faint signal). Comparing our results with Absolute frequency measurements of the $^1S_0 \rightarrow {}^1P_1$ transition in ytterbium [58], it is safe to draw a conclusion that we have observed different isotopes of ytterbium. See the Table. 6.1 for an overview.
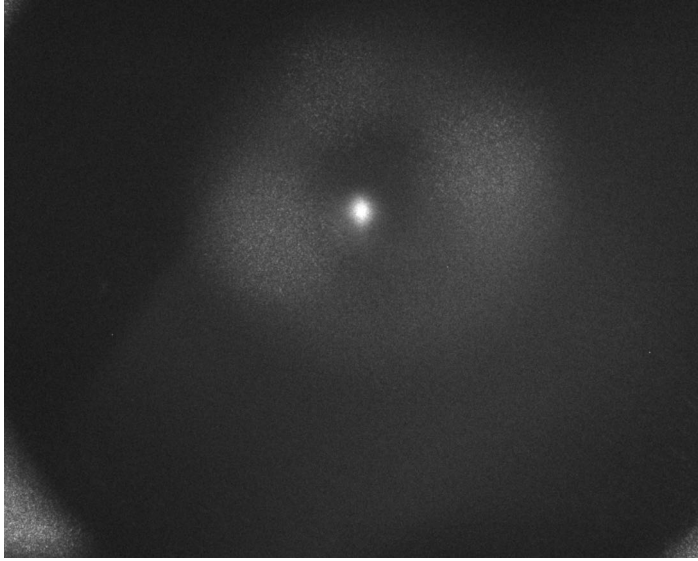
Figure 6.2: Fluorescence of 2D-MOT recorded by a camera. The camera is focused on to the MOT. The shadow of the ring is the facet of the differential pumping section, and one can see that it is in the center.

Parameter	Value
Dispenser current	4.2 A
2D-MOT cooling power (right after the fiber output - 1cm beam)	62 mW
3D-MOT cooling power (right after the fiber output - 1cm beam)	130 mW
Master laser	lock at 375.7622 THz
Blue MOT laser	lock at 375.7627 THZ.
Push beam red detuning	270 MHz($-$1st order AOM
Push beam power	0.318 mW($\sim$ 1 cm beam diameter)
Compensation coil current	1.46 A(optimum)
MOT Coil current	40 A
2D-MOT chamber pressure	$1.5 \cdot 10^{-9}$ mbar
Science chamber pressure	$9.2 \cdot 10^{-11}$ mbar

Table 6.2: MOT parameters

6.2 Blue (399 nm) 3D-MOT in the Science Chamber

After confirming that we observed MOTs for ytterbium isotopes, the blue (399 nm) 3D-MOT in the science chamber can be implemented. For this purpose, we need to optimize the position of the 2D-MOT and align the atomic beam to the differential pumping tube first. Then we need to apply a push beam for 3D MOT since adding additional pushing beams can significantly improve the efficiency of transfer from 2D to 3D-MOT camber. The additional radiation pressure of a pushing beam is used to match the velocity distribution emerging from the 2D-MOT to the capture range of the 3D-MOT and to enhance the transfer of axially slow atoms [14]. With the MOT parameters shown in Table 6.2, a fluorescence image of the 3D-MOT can be seen in the Fig. 6.3. It also can be visible by the naked eyes as shown in Fig. 6.4.

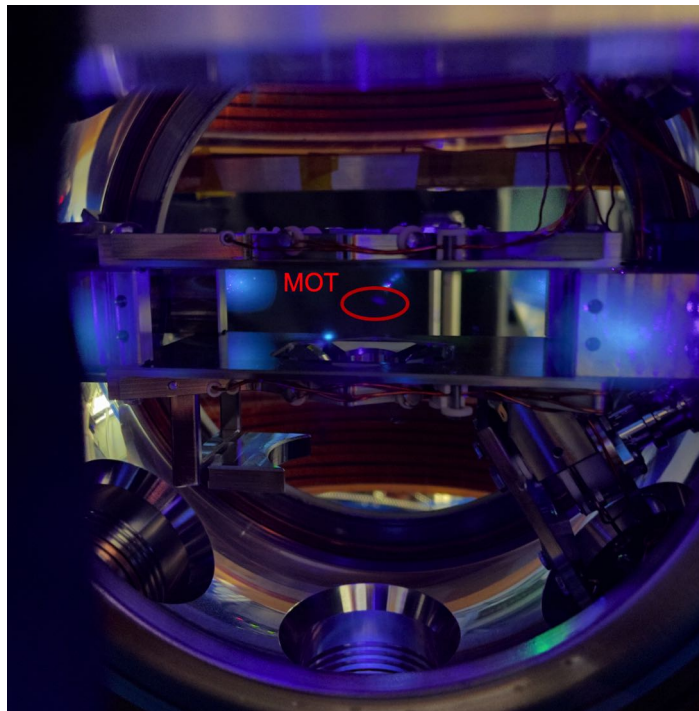Figure 6.3: Fluorescence image of 3D MOT recorded by a camera behind the science chamber.

Figure 6.4: Fluorescence image of 3D MOT taken by phone camera.

Summary and Outlook

In the scope of this thesis, a new ultra-cold ytterbium experiment for nonlinear quantum optics based on Rydberg atoms was constructed. The main focus was setting up the laser system with high frequency stability and probe/control pulse shaping for precise excitation of Rydberg atoms via a two-photon transition. Furthermore, a new UHV compatible 2D chamber made of titanium and BK7 glass was designed and constructed in-house. After combining the new 2D titanium chamber and the science chamber, consecutively the 2D-MOT, and then the blue 3D-MOT have been achieved. At the current status, the realization of the green (556 nm) 3D-MOT, optimization of the MOTs(both 2D and 3D side), and absorption imaging of the atomic cloud are under progress.

For the laser stabilization, we use two different locking techniques for the different lasers: The Master laser, Rydberg laser, and Green MOT laser were locked to an ultra-stable high finesse $\mathcal{F} \sim 40000$ cavity using the Pound-Drever-Hall locking technique. The performance of laser lock was characterized by optical heterodyne detection. In the end, a sub 10 Hz linewidth of stabilized laser with a longterm drift of 15 Hz has been achieved. The two probe lasers and one blue MOT laser producing light at 399 nm have been locked via offset-phase-lock technique to the Master laser. A beat linewidth lower than 100 Hz was obtained.

To implement Rydberg EIT, a weak probe beam and a strong, counter-propagating control beam are needed. Since Rydberg EIT can be highly sensitive to probe/control pulse shape, a high fidelity (less than 1% distortion) Gaussian pulse was established by utilizing the arbitrary function generator (AWG) and acousto-optic modulator (AOM). The rise time of DLpro 1/2 laser AOM were measured by a single photon counter with Time tagger. In addition, An automatic method for calibrating AOM has also been developed.

A new titanium UHV Chamber for 2D-MOT was constructed. Compared to the previous glass cell from Japancell, the titanium chamber is far more resistant to stress and reliable. It's hardly broken when aligning the chamber. The titanium frame was cleaned before being glued on four pieces of glass plates. Once the cleaning process was done, the BK7 viewports were glued to the frame. The leak proof was also checked. After assembling it into the experiment system, and baking of the vacuum system started. Fially, $8.7 \cdot 10^{-11}$ mbar in the 2D chamber, $8.9 \cdot 10^{-11}$ mBar in the 3D chamber were achieved.

Since that, we have had a complete vacuum experiment system and stabilized laser system. The starting point of the experiment, magneto-optical trap, was realized. We observed MOTs of different ytterbium isotopes in the 2D chamber and blue (399 nm) 3D-MOT in the science chamber.

The next stage of this experiment is realizing the Green (556 nm) MOT in the science chamber and optimizing the setup to have high atom number in the MOT region. After that, the sawtooth wave adiabatic passage (SWAP) cooling scheme [59] and movable arrays of dipole traps can be implemented. A preliminary SWAP cooling measurement in a 3D-MOT demonstrates the concept and confirms that the cooling method and design offer significant promise for further experiments [59]. SWAP cooling with a green 3D-MOT, in particular, should be thoroughly investigated to see how free parameters affect cooling efficiency and ultimately optimize the trap as desired.

Bibliography

[1] H. E. White et al., *Introduction to atomic spectra*, (1934) (cit. on p. 1).

[2] C. Tresp, *A setup for highly precise excitation and detection of Rydberg atoms*,
     Masterarbeit. Universität Stuttgart (2012) (cit. on p. 1).

[3] E. Urban et al., *Observation of Rydberg blockade between two atoms*,
     Nature Physics **5** (2009) 110 (cit. on p. 1).

[4] S. Gleyzes et al., *Quantum jumps of light recording the birth and death of a photon in a cavity*,
     Nature **446** (2007) 297 (cit. on p. 1).

[5] J.-M. Raimond, M. Brune and S. Haroche,
     Manipulating quantum entanglement with atoms and photons in a cavity,
     Reviews of Modern Physics **73** (2001) 565 (cit. on p. 1).

[6] Y. Dudin and A. Kuzmich, *Strongly interacting Rydberg excitations of a cold atomic gas*,
     Science **336** (2012) 887 (cit. on p. 1).

[7] B. Zhao, M. Müller, K. Hammerer and P. Zoller,
     Efficient quantum repeater based on deterministic Rydberg gates,
     Physical Review A **81** (2010) 052329 (cit. on p. 1).

[8] C. Tresp,
     Rydberg polaritons and Rydberg superatoms-novel tools for quantum nonlinear optics, (2017)
     (cit. on p. 1).

[9] C. Liu, Z. Dutton, C. H. Behroozi and L. V. Hau, *Observation of coherent optical information
     storage in an atomic medium using halted light pulses*, Nature **409** (2001) 490 (cit. on p. 1).

[10] T. Peyronel et al.,
     Quantum nonlinear optics with single photons enabled by strongly interacting atoms,
     Nature **488** (2012) 57 (cit. on p. 1).

[11] O. Firstenberg et al., *Attractive photons in a quantum nonlinear medium*, Nature **502** (2013) 71
     (cit. on p. 1).

[12] N. Stiesdal et al.,
     Observation of three-body correlations for photons coupled to a Rydberg superatom,
     Physical review letters **121** (2018) 103601 (cit. on p. 1).

[13] S. N. Pisharody, *Electron dynamics in double Rydberg wavepackets*,
     University of Virginia, 2003 (cit. on p. 2).

[14] S. Dörscher et al., *Creation of quantum-degenerate gases of ytterbium in a compact
     2D-/3D-magneto-optical trap setup*, Review of Scientific Instruments **84** (2013) 043109
     (cit. on pp. 2, 14, 67, 69).

Bibliography

[15]   M. Takamoto, F.-L. Hong, R. Higashi and H. Katori, *An optical lattice clock*,
       Nature **435** (2005) 321 (cit. on p. 3).

[16]   B. Bloom et al., *An optical lattice clock with accuracy and stability at the 10- 18 level*,
       Nature **506** (2014) 71 (cit. on pp. 3, 4).

[17]   Y. Takasu et al., *Spin-singlet Bose-Einstein condensation of two-electron atoms*,
       Physical Review Letters **91** (2003) 040404 (cit. on p. 3).

[18]   A. J. Daley, M. M. Boyd, J. Ye and P. Zoller,
       Quantum computing with alkaline-earth-metal atoms,
       Physical review letters **101** (2008) 170504 (cit. on p. 3).

[19]   A. V. Gorshkov et al., *Two-orbital SU (N) magnetism with ultracold alkaline-earth atoms*,
       Nature physics **6** (2010) 289 (cit. on p. 3).

[20]   C. Foot, D. Foot and C. Foot, *Atomic Physics*, Oxford Master Series in Physics,
       OUP Oxford, 2005, ISBN: 9780198506966,
       URL: https://books.google.de/books?id=kXYpAQAAMAAJ (cit. on p. 3).

[21]   S. Stellmer, R. Grimm and F. Schreck, *Production of quantum-degenerate strontium gases*,
       Physical Review A **87** (2013) 013611 (cit. on p. 4).

[22]   A. Derevianko and H. Katori, *Colloquium: Physics of optical lattice clocks*,
       Reviews of Modern Physics **83** (2011) 331 (cit. on p. 4).

[23]   S. Kato, S. Sugawa, K. Shibata, R. Yamamoto and Y. Takahashi,
       Control of resonant interaction between electronic ground and excited states,
       Physical review letters **110** (2013) 173201 (cit. on p. 4).

[24]   H. Ott et al., *Radio frequency selective addressing of localized atoms in a periodic potential*,
       Physical review letters **93** (2004) 120407 (cit. on p. 4).

[25]   C. S. Adams, H. J. Lee, N. Davidson, M. Kasevich and S. Chu,
       Evaporative cooling in a crossed dipole trap, Physical review letters **74** (1995) 3577
       (cit. on p. 4).

[26]   F. Scazza,
       Probing SU (N)-symmetric orbital interactions with ytterbium Fermi gases in optical lattices,
       PhD thesis: lmu, 2015 (cit. on p. 4).

[27]   J. E. Sansonetti and W. C. Martin, *Handbook of basic atomic spectroscopic data*,
       Journal of physical and chemical reference data **34** (2005) 1559 (cit. on p. 5).

[28]   Y. Takasu et al., *Photoassociation spectroscopy of laser-cooled ytterbium atoms*,
       Physical review letters **93** (2004) 123202 (cit. on p. 5).

[29]   K. Beloy et al.,
       Determination of the 5 d 6 s 3 D 1 state lifetime and blackbody-radiation clock shift in Yb,
       Physical Review A **86** (2012) 051404 (cit. on p. 5).

[30]   S. G. Porsev and A. Derevianko,
       Hyperfine quenching of the metastable P 0, 2 3 states in divalent atoms,
       Physical Review A **69** (2004) 042506 (cit. on p. 5).

[31] H. J. Metcalf and P. van der Straten, *Laser cooling and trapping of atoms*, JOSA B **20** (2003) 887 (cit. on p. 6).

[32] A. J. Daley, *Quantum computing and quantum simulation with group-II atoms*, Quantum Information Processing **10** (2011) 865 (cit. on p. 6).

[33] J. W. Cho et al., *Optical repumping of triplet-P states enhances magneto-optical trapping of ytterbium atoms*, Physical Review A **85** (2012) 035401 (cit. on p. 6).

[34] S. Porsev, Y. G. Rakhlina and M. Kozlov, *Electric-dipole amplitudes, lifetimes, and polarizabilities of the low-lying levels of atomic ytterbium*, Physical Review A **60** (1999) 2781 (cit. on p. 6).

[35] H. Busche, S. W. Ball and P. Huillery, *A high repetition rate experimental setup for quantum non-linear optics with cold Rydberg atoms*, The European Physical Journal Special Topics **225** (2016) 2839 (cit. on p. 7).

[36] E. Distante et al., *Storing single photons emitted by a quantum memory on a highly excited Rydberg state*, Nature communications **8** (2017) 1 (cit. on p. 7).

[37] M. Chen and K. Cheng, *Hyperfine quenching of the metastable 4s4p 3p0 and 3p2 states of zn-like ions*, Canadian Journal of Physics **89** (2011) 473 (cit. on p. 9).

[38] F. Gounand, *Calculation of radial matrix elements and radiative lifetimes for highly excited states of alkali atoms using the Coulomb approximation*, Journal de Physique **40** (1979) 457 (cit. on p. 9).

[39] I. Beterov, I. Ryabtsev, D. Tretyakov and V. Entin, *Quasiclassical calculations of BBR-induced depopulation rates and effective lifetimes of Rydberg nS, nP and nD alkali-metal atoms with n< 80*, arXiv preprint arXiv:0810.0339 (2008) (cit. on p. 10).

[40] J. Lee, J. H. Lee, J. Noh and J. Mun, *Core-shell magneto-optical trap for alkaline-earth-metal-like atoms*, Physical Review A **91** (2015) 053405 (cit. on pp. 11, 15, 20).

[41] D. J. Hucknall, *Vacuum technology and applications*, Elsevier, 2013 (cit. on p. 18).

[42] S. Uetake, R. Murakami, J. M. Doyle and Y. Takahashi, *Spin-dependent collision of ultracold metastable atoms*, Physical Review A **86** (2012) 032712 (cit. on p. 20).

[43] A. H. Hansen et al., *Quantum degenerate mixture of ytterbium and lithium atoms*, Physical Review A **84** (2011) 011606 (cit. on p. 21).

[44] J. Wilson et al., *Trapped arrays of alkaline earth Rydberg atoms in optical tweezers*, arXiv preprint arXiv:1912.08754 (2019) (cit. on p. 23).

[45] E. D. Black, *An introduction to Pound–Drever–Hall laser frequency stabilization*, American journal of physics **69** (2001) 79 (cit. on p. 31).

[46] D. Matei et al., *1.5 µ m lasers with sub-10 mHz linewidth*,
      Physical review letters **118** (2017) 263202 (cit. on p. 32).

[47] G. Di Domenico, S. Schilt and P. Thomann,
      Simple approach to the relation between laser frequency noise and laser line shape,
      Applied optics **49** (2010) 4801 (cit. on pp. 33, 34).

[48] P. Lunt,
      Design and Construction of a New Ultracold Ytterbium Experiment For Rydberg Physics,
      (1. January 2019.) (cit. on p. 35).

[49] A. Khintchine, *Korrelationstheorie der stationären stochastischen Prozesse*,
      Mathematische Annalen **109** (1934) 604 (cit. on p. 40).

[50] J. J. Olivero and R. Longbothum, *Empirical fits to the Voigt line width: A brief review*,
      Journal of Quantitative Spectroscopy and Radiative Transfer **17** (1977) 233 (cit. on p. 41).

[51] *LeCroy Corporation. WavePro DSO Operators Manual. New York, USA: LeCroy Corporation,
      2002*, () (cit. on p. 41).

[52] I. Novikova, R. L. Walsworth and Y. Xiao,
      Electromagnetically induced transparency-based slow and stored light in warm atoms,
      Laser & Photonics Reviews **6** (2012) 333 (cit. on p. 49).

[53] B. Macke and B. Ségard, *Pulse Normalisation in Slow-Light Media*,
      Physical Review A **73** (2006) 043802 (cit. on p. 49).

[54] J. Cheng, S. Han and Y. Yan, *Nonlinear propagation of ultraslow pulses in media with
      electromagnetically induced transparency*, Optics letters **30** (2005) 2638 (cit. on p. 49).

[55] L. Theis, F. Motzoi, F. Wilhelm and M. Saffman,
      High-fidelity Rydberg-blockade entangling gate using shaped, analytic pulses,
      Physical Review A **94** (2016) 032306 (cit. on p. 49).

[56] M. H. From, *Towards Rydberg quantum optics with ultra-cold Yb atoms*, (June 11, 2021)
      (cit. on p. 65).

[57] K. Dieckmann, R. Spreeuw, M. Weidemüller and J. Walraven,
      Two-dimensional magneto-optical trap as a source of slow atoms,
      Physical Review A **58** (1998) 3891 (cit. on p. 67).

[58] T. Lauprêtre et al.,
      Absolute frequency measurements of the 1 S 0→ 1 P 1 transition in ytterbium,
      OSA Continuum **3** (2020) 50 (cit. on p. 68).

[59] M. Holland and J. Bartolotta, "Sawtooth Wave Adiabatic Passage in a Magneto-Optical Trap",
      APS Division of Atomic, Molecular and Optical Physics Meeting Abstracts, vol. 2020, 2020
      E01 (cit. on p. 72).

List of Figures

List of Tables